1-15-2019

Ignition and Extinction Behavior of Fuels in a Microcombustor

Pawan Sharma

IGNITION AND EXTINCTION BEHAVIOR OF FUELS IN A MICROCOMBUSTOR

A Dissertation

Submitted to the Graduate Faculty of the
Louisiana State University and
Agricultural and Mechanical College
in partial fulfillment of the
requirements for the degree of
Doctor of Philosophy

in

Mechanical Engineering

by
Pawan Sharma
B.Tech., Indian Institute of Technology (BHU), Varanasi, 2013
M.Tech., Indian Institute of Technology (BHU), Varanasi, 2013
May 2019

Acknowledgments

My first acknowledgement goes to my Ph.D. supervisor and mentor, Professor Ingmar Schoegl for his continuous support and guidance during my doctorate degree. He always provided me with a nice environment to do my research. I am happy that I had the opportunity to work under his supervision, where I learnt to keep high standards and work toward them.

I am honored that Dr. Keith Gonthier, Dr. Ram Devireddy, Dr. Ye Xu, and Dr. Shyam Menon accepted to be in my dissertation committee, to whom I am thankful for their thoughtful comments and suggestions to improve my work.

I would like to acknowledge the financial support by the Lawrence Livermore National Laboratory under contract DE-AC52-07NA27344 and the Economic Development Assistantships (EDA) program. I would also like to acknowledge that portions of this research were conducted with high performance computing resources provided by Louisiana State University (http://www.hpc.lsu.edu).

My deepest gratitude goes to my family, especially to my parents. Finally, I would like to thank all of my teachers and colleagues at Louisiana State University, who directly or indirectly helped me accomplish my PhD.

Table of Contents

APPENDIX

List of Tables

List of Figures

Abstract

Conventional fuel testing device-CFR engine requires large quantities of fuels, which makes it unsuitable for research of small samples of fuels. This current study seeks to address this limitation by using an externally heated microcombustor as an alternative fuel testing device. Mainly three combustion behaviors have been observed inside a microcombustor: strong flames at higher flow rates, Flames with Repetitive Extinction and Ignition (FREI) at intermediate flow rates, and weak flames at marginal flow rates. In previous studies, weak combustion behavior has been proven suitable to study fuel properties from small samples of fuels. Microcombustor experiments typically rely on flame images. Imaging of weak flame needs long camera exposures due to reduced CH^* emissions, hence weak flame experiments are not suitable for high throughput testing. FREI and strong flames give stronger CH^* emission signals and can provide high throughput testing ability. The objective of this work is to investigate the potential of FREI and strong flames for fuel research and screening purposes. A major novelty of this work is to evaluate FREI behavior through low-speed imaging and a microphone. FREI ignition and extinction temperatures of methane, ethane, propane, dimethyl ether and ethylene are shown to be fuel specific. The strong flame behavior is used to obtain insights into laminar flame speed of fuels. The respective impacts of microcombustor diameter, external heating, and unburned mixture equivalence ratio have been studied well. The open-source CFD package OpenFOAM with the detailed chemistry solver LaminarSMOKE is used to study FREI behavior of stoichiometric propane-air mixtures at engine relevant pressures. In simulations, critical fuel properties - i.e., FREI ignition and extinction temperatures, quenching diameter, and flame thickness, are found to decrease with increasing pressure similar to conventional IC engine behavior. Overall, fuel specific behavior of microcombustion and elevated pressure simulation results have shown microcombustion potential for fuel characterization for IC engines.

Chapter 1
Motivation and Approach

1.1 Introduction

In this thesis, microcombustion has been proposed as a convenient approach for research and characterization of small samples of fuels. Fuel consumption (1-10 cm/min for gaseous fuels) for externally heated microcombustors scale properly with small samples of fuels. Externally heated microcombustors have potential to provide inexpensive diagnostics and a high-throughput ability for new fuels screening. The primary objective of this thesis is to determine whether combustion behavior inside an externally heated microcombustor can be used for fuel research and characterization. The fuel data acquired from the microcombustor experiments can be used to develop and validate kinetic mechanisms of new fuels.

The specific objectives of the current work are as follows:

- Develop a first working prototype of the small sample fuel-tester.
- Examine different combustion regimes inside the microcombustor.
- Investigate the respective impacts of external heating, microcombustor inner diameter, and fuel-air mixture equivalence ratio on combustion regimes inside the microcombustor.
- Investigate ignition, flame propagation, and extinction behavior of test fuels inside the microcombustor.
- Assess expected combustion phenomena inside the microcombustor for engine relevant pressure.

This chapter discusses the motivation and approach for this work. Section 1.2 describes GHG emission of fossil fuels and the worldwide fuel economy and emission standards. Section 1.3 discusses essential engine parameters and behaviors. Section 1.4 discusses some important combustion fundamentals. Finally, initiatives taken by the United States Department of Energy (DOE) to

accelerate bio-fuels research and shortcomings of Cooperative Fuel Research (CFR) for bio-fuels testing are explained in detail (Section 1.5).

1.2 GHG Emission and Fuel Economy Standards

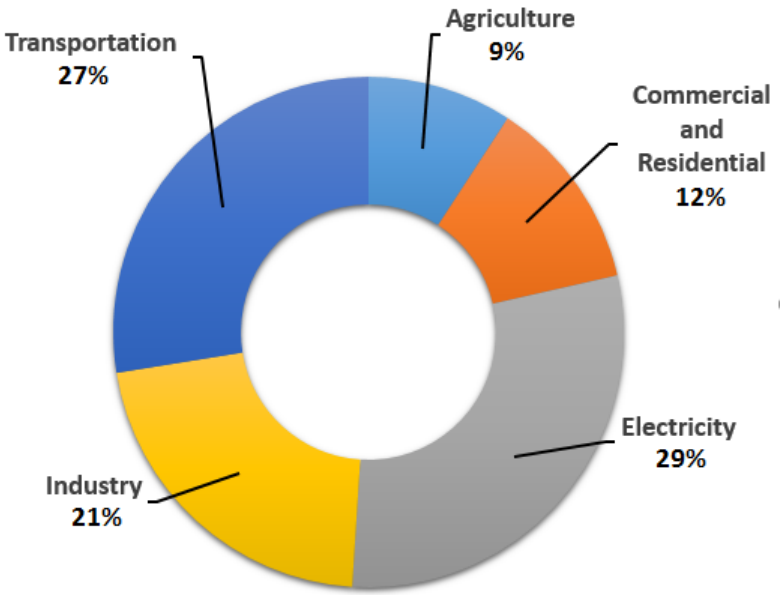

Figure 1.1: Global greenhouse gas emissions by economic sector. [78]

Despite fast growth of the renewable energy sector and electric vehicles, fossil fuels remain the single largest source of the world energy supply [5, 4]. Fossil fuel combustion emits Green House Gases (GHG), such as carbon dioxide (CO_2) and methane (CH_4). GHG keep the earth warm by absorbing solar energy, but excess GHG in the atmosphere warms up the planet and causes global warming [25, 75, 43]. The transportation sector is a significant contributor to GHG emissions. A sharp rise in the atmospheric CO_2 concentration has been observed in recent decades due to GHG emissions where a significant amount stems from petroleum-powered motor vehicles [78, 40, 77]. 3.2 billion barrels of gasoline are burned by automobiles in the USA each year [81]. The transportation sector contributes 70 percent of the total U.S. petroleum consumption and 27 percent of the total USA GHG emissions as shown in Figure 1.1 [78]. Demand for transportation vehicles is expected to increase drastically by 2050 because of increases in the world population and further advancement of developing countries [5, 4], which makes future vehicles fuel economy and emission standards important.

The US government and other nations are setting strict vehicle emission standards to ensure a safe environment for future generations. In the US, the Department of Transportation's National Highway Traffic Safety Administration (NHTSA) and the Environmental Protection Agency (EPA)

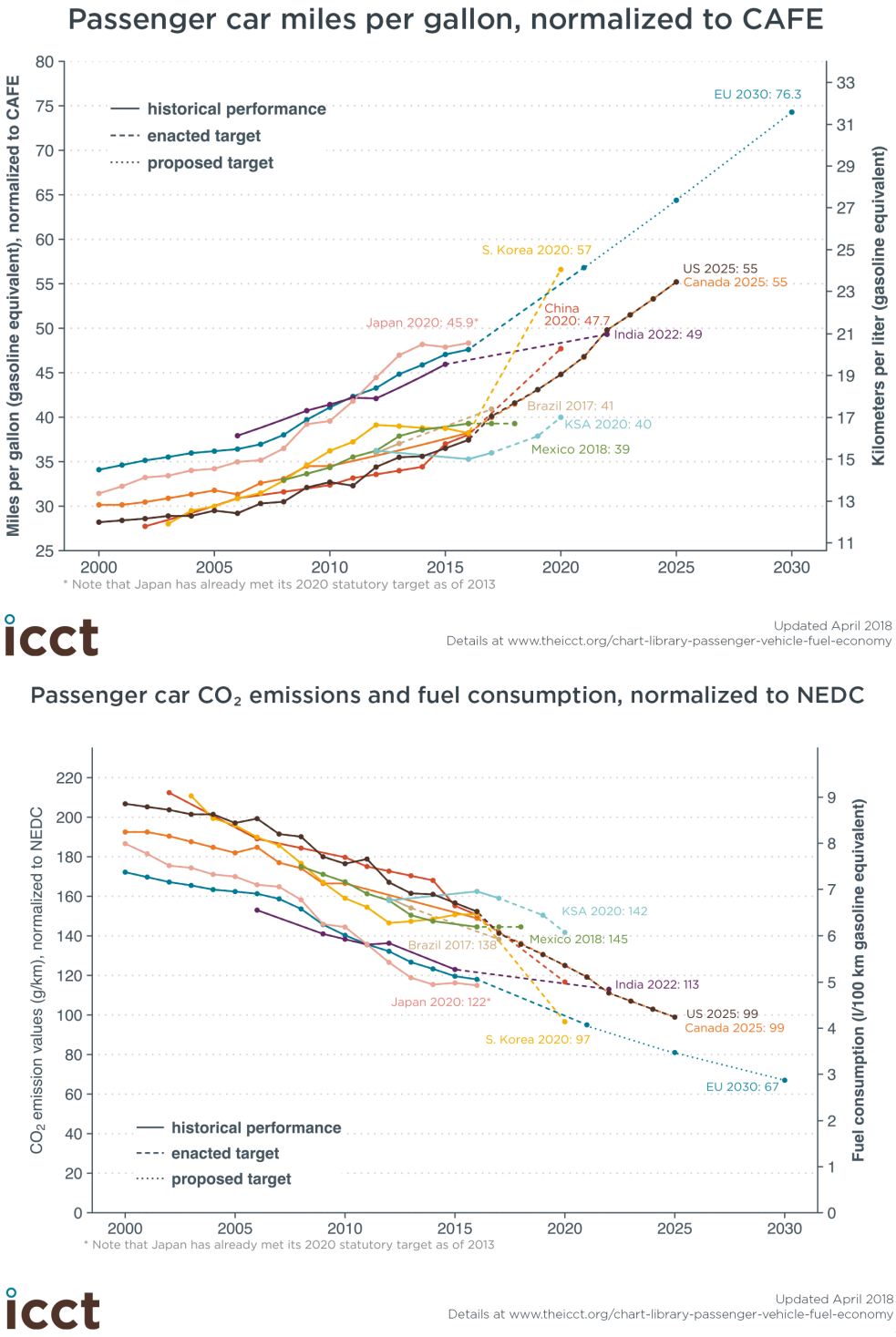

Figure 1.2: Comparison of Global Fuel Economy Standards and CO_2 Emission Standards. [109]

have made new fuel economy regulations to reduce the greenhouse gas emission and improve the fuel economy of light-duty vehicles and medium-duty passenger vehicles of 2017-2026 [93, 3, 82, 76]. These new rules are an amended version of the United States Corporate Average Fuel Economy (CAFE) standards. CAFE standards were first enacted in 1975 by the United States government to improve fuel economy of motor vehicles after the 1973 oil crisis [6]. The first legislative change to CAFE standards was done in 2007 by passing the Energy Independence and Security Act (EISA) [74]. EISA set a target of 35 miles per gallon for future vehicles by 2020 [74]. In 2011, the United States government set new CAFE standards to make fuel economy standards reach 54.5 miles per gallon for light-duty vehicles and medium-duty passenger vehicles for 2017–2025 model years [93, 3, 82], which were further amended in August, 2018 through the Safer Affordable Fuel-Efficient (SAFE) vehicles rule for model years 2021-2026 passenger cars and light trucks [76].

Figure 1.2 compares CO_2 emission/fuel consumption and passenger car miles per gallon, respectively, for eight governments that account for more than 80 percent of global vehicle sales [78, 7, 109]. Fuel consumptions are compared in terms of miles per gallon and normalized to the CAFE value. CO_2 emission values are expressed in gm per kilometer and normalized to the New European Driving Cycle (NEDC) standard. NEDC are emission/fuel economy standards for passenger vehicles. Figure 1.2 shows that the European Union has the most stringent fuel economy and CO_2 emission standards out of all major players. Figure 1.2 further shows that the US and Canada follow almost the same standard, while Saudi Arabia, South Korea, and Mexico are a few years behind the US and Canada. Figure 1.2 illustrates that in comparison of several other countries CAFE standards are still lenient. All motor vehicle manufacturers in the US operate on a global basis, so the United States automobile manufacturers will still have to comply with global standards even if the US government eases CAFE standards, which makes future vehicles fuel economy/emission significant to the United States automakers.

1.3 Important Engine Parameters and Behaviors

Stringent fuel economy and emission standards have forced automotive manufacturers to search for new fuels and engine technologies with high fuel economy and a low carbon content to achieve CAFE standards. This section discusses indicated thermal efficiency, octane numbers, knock, and laminar flame speed in detail, which are important to engine performance and fuel economy.

1.3.1 Indicated Thermal Efficiency

Indicated thermal efficiency is significant with respect to engine fuel economy. Indicated thermal efficiency is defined as a ratio of net work output generated to the fuel heat energy. Indicated thermal efficiency is given by an expression shown in Equation 1.1 for the Otto cycle in SI engines.

$$\eta = 1 - \frac{1}{r^{\gamma-1}} \tag{1.1}$$

where r is the engine compression ratio and γ is the ratio of specific heats $(\frac{C_p}{C_v})$. γ in terms of degrees of freedom is shown in Equation 1.2. As temperature increases, molecules degrees of freedom increases and γ decreases.

$$\gamma = \frac{f+2}{f} \tag{1.2}$$

1.3.2 Engine Knock

Engine knock is an abnormal combustion phenomenon, which occurs in spark ignition (SI) engines [35]. Combustion of the fuel-air mixture inside the engine cylinder which does not result from the flame front initiated by the spark plug is known as knock. Engine knock is harmful to the engine structure and causes a loss in peak power.

The spark plug ignites the unburned compressed fuel-air mixture in an SI engine, and a turbulent flame front develops and travels through the combustion chamber. This turbulent flame front compresses the end gas and raises its pressure and temperature, and this causes a rapid release of the energy by the end gas combustion due to auto-ignition, resulting in engine knock. Knock

creates metal-pinging sounds and vibrations. Metal-pinging sounds from knock are repeatable and recurrent. Higher compression ratios are conducive to knock phenomena because of resultant high pressure and temperature inside the engine cylinder. Engine knock limits the engine thermal efficiency by limiting the engine compression ratio.

Characteristics of knock depend on the pressure and temperature time history of the end gas in an IC engine [35]. Figure 1.3 shows the cylinder pressure history for normal engine cycle, moderate knock, and super knock, respectively [48]. Normal combustion does not show high-frequency pressure fluctuations, while high-frequency pressure fluctuations are larger in magnitude ($\sim$ 140 bar) for the super knock in comparison of the moderate knock ($\sim$ 24 bar). These high-frequency pressure fluctuations dampen out with time. Pressure variations occur late in the combustion process during moderate knock, while pressure changes occur earlier in the combustion process during super knock.

1.3.3 Octane Ratings

The ability of a fuel to resist knock is measured by its octane rating. Here, Research Octane Number (RON) and Motor Octane Number (MON) are two important octane ratings used to quantify ignition properties of fuels and determined by standard test methods prescribed by ASTM D2699 and ASTM D2700, respectively [2, 1]. ASTM D2699 and ASTM D270 are performed in a Cooper-

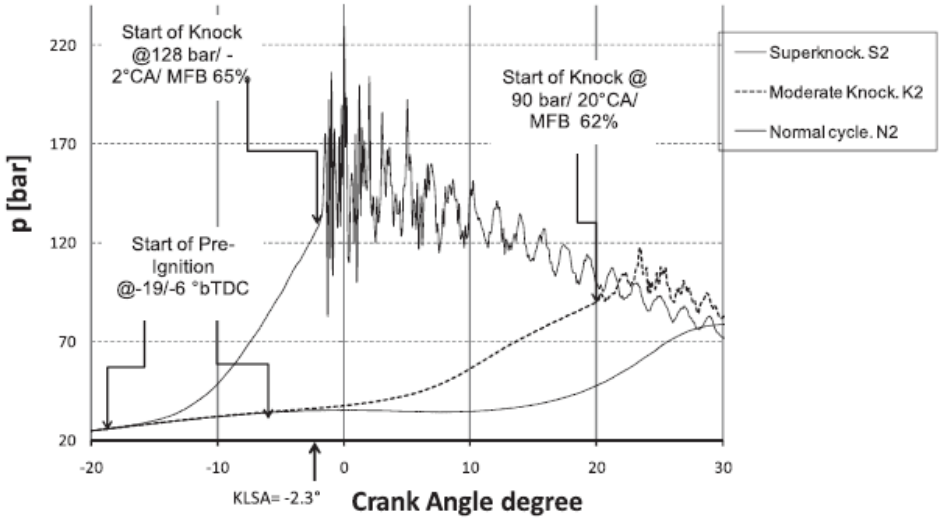

Figure 1.3: Normal cycle, moderate knock, and super knock in a turbocharged engine. In-cylinder pressure traces from experiments. [48]

ative Fuel Research (CFR) engine for knock characterization [2, 1]. The CFR engine (Figure 1.4) is a four-stroke, single cylinder spark-ignition variable compression engine developed by Waukesha Motor Company for testing and performance analysis of fuels [41, 107, 12]. Before the invention of the CFR engine in 1928, the maximum engine compression ratio was used as an engine parameter for knock characterization [87]. The first CFR engine was manufactured and delivered in 1929 [41, 107]. Various engine parameters, e.g., fuel choice, ignition timing, and compression ratio can be controlled in the CFR engine for octane rating measurements.

Octane scales were originally based on primary reference fuel (PRF) blends, which are mixtures of a known volume of n-heptane and iso-octane. RON/MON standards do not explain the auto-ignition characteristics of practical fuels very well with PRFs as reference fuels because practical fuels contain aromatic and olefins components other than paraffins. To better understand the auto-ignition characteristics of practical fuels PRFs were replaced by TSFs. Toluene standard fuels (TSFs) are used as reference fuels for knock characterization in CFR engines. TSF blends are mixtures of a known volume of reference fuel grade n-heptane, iso-octane, and toluene.

RON characterizes the behavior of a fuel at lower speeds and temperatures and an indicative of

Figure 1.4: Waukesha Cooperative Fuel Research (CFR) engine (image source: http://www.waukeshacfr.com).

typical road performance. In the RON test procedure, the CFR engine is operated at a constant speed (600RPM) with an intake mixture temperature of 325K; the compression ratio is increased until the onset of knocking, and finally knock behavior of the test fuel is compared to the knocking behavior of one or more blends of TSF of known octane numbers [2]. MON indicates the behavior of a fuel at higher speeds and temperatures. MON is determined by testing the fuel inside a CFR engine with a preheated fuel-air mixture, variable ignition timing, and higher engine speeds. In the MON test procedure, the CFR engine is operated at a constant speed (900RPM) with an intake mixture temperature 422K. Again, the compression ratio is increased until the onset of knocking [1]. MON is usually 8 to 10 points lower than the RON because preheated fuel-air mixture, variable ignition timing, and higher engine speeds decrease the fuel's knock resistance. Testing parameters for RON and MON are shown in Table 1.1.

Anti-Knock Index (AKI) is defined as average of RON and MON values (Equation 1.3). AKI is the fuel rating stated at US gas stations.

$$AKI = \frac{RON + MON}{2} \tag{1.3}$$

Fuel sensitivity (S) is defined as the difference in RON and MON values, and it is zero by definition for PRFs (Equation 1.4).

$$S = RON - MON \tag{1.4}$$

Table 1.1: ASTM standards for RON and MON [2, 1]

	RON	MON
Engine Speed (rpm)	600 ± 6	900 ± 9
Inlet Temperature (K)	325.15	422.15 ± 1
Inlet Pressure	Atmospheric	Atmospheric
Spark Advance (degree)	13 BTC	19-26 BTC (Varies with compression ratio)
Equivalence Ratio (phi)	Adjusted to achieve maximum knock intensity	Adjusted to achieve maximum knock intensity

In addition to RON, MON, and AKI, the Octane Index (OI) has been often used in the literature to understand knock behavior of practical fuels [47, 48, 46]. OI is defined as:

$$OI = RON - K(RON - MON) \tag{1.5}$$

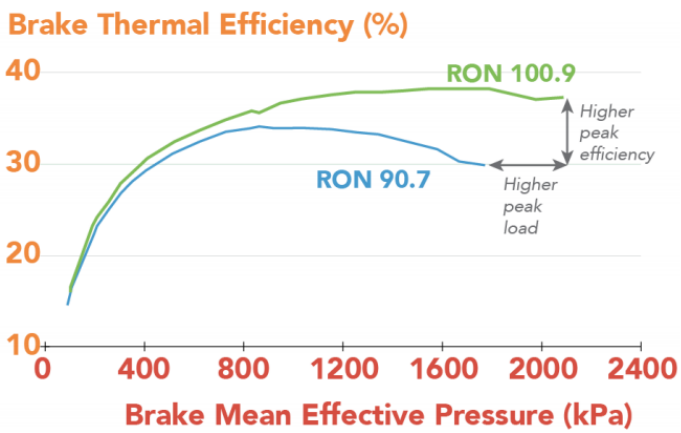

Figure 1.5: Impact of Research Octane Number on Brake Thermal Efficiency. [21]

K is a constant parameter and depends on pressure and temperature histories of the unburned mixture [47, 48, 46]. Pressure and temperature in the end gas are influenced by operating conditions and engine design. The value of K depends on operating conditions and engine design, hence a practical fuel's (S>0) OI will vary with the operating conditions and engine design [47, 48, 46].

Traditional gasoline fuels restrict the ability of car manufacturers to increase engine compression ratio due to moderate octane numbers. Figure 1.5 exhibits how a high research octane number (RON) fuel provides higher peak efficiency at higher brake mean effective pressures in comparison to a low RON fuel, where brake mean effective pressure indicates a theoretical pressure applied on the engine piston uniformly from the top to the bottom to create a measured brake power output in each power stroke [21]. Ethanol is one example of bio-fuel, which is used as an octane booster in traditional gasoline fuel blends [106, 57, 38, 110, 105].

1.3.4 Dilution Tolerance

Exhaust gas recirculation (EGR) is a technique used to reduce NOx emission from SI and CI engines. Figure 1.6 exhibits the EGR process through a schematic diagram. EGR works by mixing

a portion of engine exhaust gas with the engine intake fuel-air mixture. EGR dilutes the incoming mixture into the combustion chamber by providing gases inert to the combustion. These inert gases act as heat absorbents in the combustion chamber and reduce the peak combustion chamber temperature. Reduced combustion chamber temperature is helpful in reducing the formation of NOx because NOx forms in significant amount only at combustion temperature above ∼1800K.

However, excess EGR makes combustion unstable in the engine cylinder. Several studies have reported that fuel with higher laminar flame speed (LFS) provides a higher tolerance for EGR dilution before combustion becomes unstable inside the engine cylinder [23, 14, 100, 53].

1.3.5 Charge Cooling

In a turbocharged engine, the turbocharger compresses the intake air. The compression process increases the intake air temperature. An increase in the intake air temperature causes a decrease in the air density; hence less oxygen is available for combustion, which causes incomplete combustion. Hot intake air also causes knock [35]. Charge cooling decreases the air temperature before it enters into the combustion chamber. Charge cooling is usually achieved by fuel vaporization inside the engine cylinder by blending ethanol (a high latent heat fuel) into the fuel. Several studies have reported the impact of charge cooling on improving engine thermal efficiency by knock mitigation,

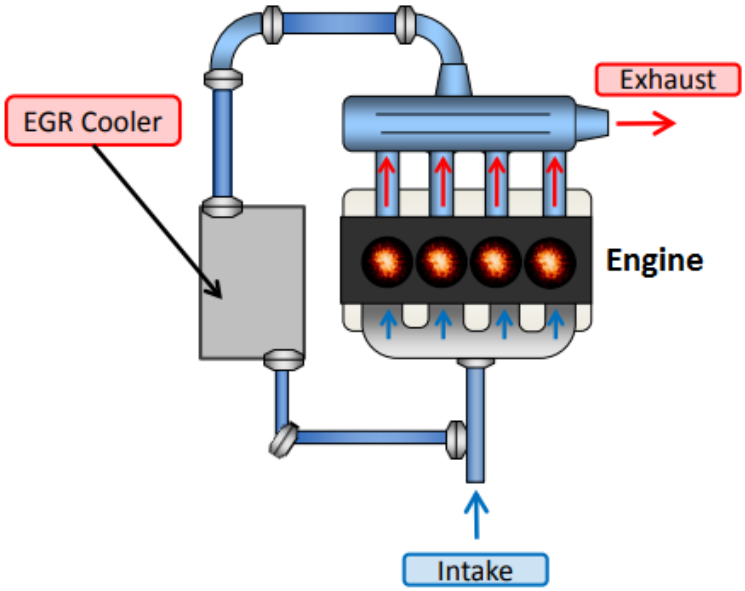

Figure 1.6: Exhaust Gas Recirculation process.

where they have found increase in knock resistance by mixing ethanol into fuel/air mixtures [57].

1.4 Combustion Fundamentals

This section discusses a few important combustion terminologies and types of flames.

1.4.1 Combustion Stoichiometry

Combustion involves exothermic chemical reactions, where fuel and oxidizer react and form oxidized products. The main oxidizer for combustion is either oxygen or atmospheric air. Air contains approximately 78% nitrogen N_2, 21% oxygen O_2, and 1% other gases by volume. For stoichiometric analysis of combustion, air is assumed to be consist 79% N_2 and 21% O_2 by volume. On mole basis, for each mole of O_2, air contains 3.76 moles of N_2. A basic combustion reaction where fuel (hydrocarbon) and oxidizer (air) reacts and forms oxidized products is shown in Equation 1.6. Here a hydrocarbon with the chemical formula C_xH_Y reacts with air and forms CO_2 and H_2O. N_2 does not react and acts as an inert gas. N_2 absorbs the heat generated by the combustion reaction and reduces the flame temperature.

$$C_xH_Y + (X + \frac{Y}{4})(O_2 + 3.76N_2) \rightarrow XCO_2 + \frac{Y}{2}H_2O + (X + \frac{Y}{4})N_2 \tag{1.6}$$

The minimum amount of air to burn all the fuel in the combustion reaction is known as stoichiometric air or theoretical air. The equivalence ratio (ϕ) is used to quantify deviation from stoichiometric mixture. ϕ is defined as the actual fuel-air ratio normalized with the stoichiometric fuel-air ratio (Equation 1.7). ϕ is 1 for a stoichiometric mixture, less than 1 for a fuel-rich mixture, and greater than 1 for a fuel-lean mixture.

$$\phi = \frac{(\text{Fuel}/\text{Air})_{\text{actual}}}{(\text{Fuel}/\text{Air})_{\text{stoic}}} \tag{1.7}$$

The stoichiometric ratio (λ) is also used alternatively to quantify a fuel-air mixture composition (Equation 1.8).

$$\lambda = \frac{1}{\phi} = \frac{(\text{Air/Fuel})_{\text{actual}}}{(\text{Air/Fuel})_{\text{stoic}}} \tag{1.8}$$

1.4.2 Types of Flames

A flame is a self-sustaining localized combustion zone, which propagates at subsonic velocity [55, 28, 102]. Depending on fuel and oxidizer interactions during combustion, flames can be classified in three main categories: premixed flames, non-premixed flames, and partially premixed flames. On the basis of the flow regime, flames can be classified in two categories: laminar flames and turbulent flames. Further laminar premixed flames will only be discussed in the scope of this thesis.

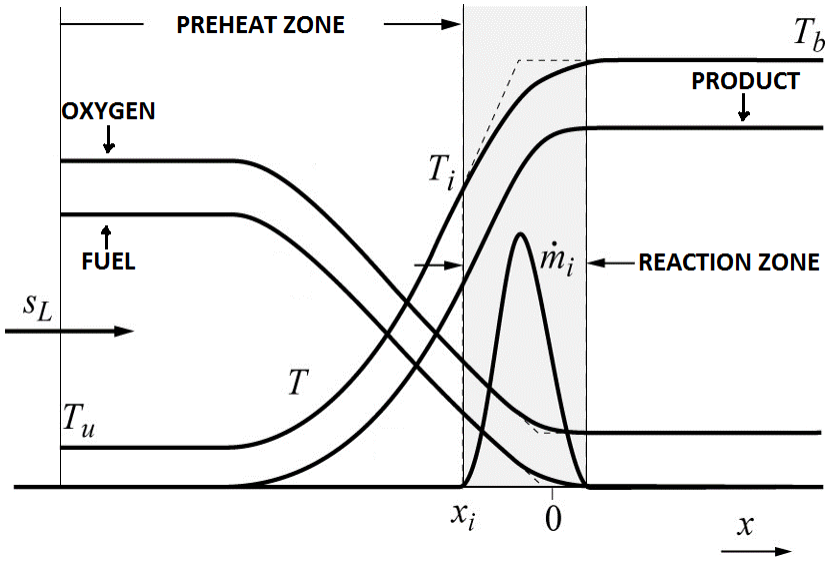

Figure 1.7: Laminar flame structure. [84]

Figure 1.7 illustrates a flame structure of a laminar premixed flame. In a laminar premixed flame, fuel and oxidizer completely mix before reaching the reaction zone. The structure of a laminar premixed flame is divided into two zones: a preheat zone and a reaction zone. As shown in Figure 1.7, fuel and oxidizer enter in the preheat zone from the upstream side with a velocity S_L. The mixture in the preheat zone continuously gets heated by heat from the reaction zone. As the mixture passes through the preheat zone, its temperature increases. When the mixture temperature reaches the inner layer temperature T_i, radical production and oxidation starts. As mixture passes through the reaction zone, the fuel is completely consumed, and combustion reaction products

convected downstream. A little heat is released in the preheat zone, while a large amount of energy released in the reaction zone.

1.4.3 Auto-Ignition Temperature and Auto-Ignition Delay Time

The auto-ignition temperature is defined as the minimum temperature at which a fuel will ignite without external energy source [55]. It is also known as self-ignition temperature or simply ignition temperature. The auto-ignition temperature of a fuel depends on pressure and flow conditions. The auto-ignition temperature is a critical parameter in determining the engine knock tendency of a fuel since knocking is caused by the auto-ignition of the unburned fuel-air mixture before the point of ignition in the engine cylinder [35].

Auto-ignition characteristics of a fuel are characterized through the auto-ignition delay time. The auto-ignition delay time is a key parameter in chemical kinetics validation. The auto-ignition delay time (τ_{id}) is measured in rapid compression machines, shock tubes, and flow reactors. The commonly used approximation for τ_{id} is given in Equation 1.9 [59, 35, 48].

$$\tau_{id} = AP^{-n} exp(\frac{E_A}{RT}) \tag{1.9}$$

Here, A and n are fuel dependent constants. P and T are the reaction chamber pressure and temperature, respectively, at the starting of fuel injection. R is the universal gas constant, and $\mathrm{E_A}$is the activation energy of the fuel. However, pressure and temperature change frequently inside an SI engine, so above expression of τ_{id} is not good enough to characterize the auto-ignition delay time.

The Livengood-Wu integral approximation is used to account for the variation of pressure and temperature during the auto-ignition delay time calculation for a homogeneous mixture [59, 35, 48]. According to this approximation (Equation 1.10), auto-ignition occurs when the integral of the inverse reciprocal of τ_{i}(T, p) becomes the unity with respect to time.

$$\int_0^t \frac{dt}{\tau_i(T,p)} = 1 \tag{1.10}$$

Auto-ignition delay times (τ_i) are measured using shock tubes, rapid compression machines (RCMs), and flow reactors. Common operational regimes of a flow reactors, shock tubes, and RCMs are illustrated in Figure 1.8, where τ_{ign} is the auto-ignition delay time and T is the initial reactive temperature. Figure 1.8 shows shock tubes are used for fast kinetics, RCMs are used for intermediate range kinetics, and flow reactors are used for slow kinetics, and no single device is capable of probing all different reactions. Further, this section discusses shock tube, RCM, and flow reactors.

- **1.4.3.1 Shock Tubes**

Shock tubes are used to study chemical kinetics and auto-ignition properties of fuels. Shock tubes are most suitable for high pressures and temperatures ranges because the boundary layer affects chemical kinetics at low pressures and temperatures, hence shock tubes are used to study fast reactions with small auto-ignition delays [97, 66].

A shock tube consists of a long tube, which is divided into two sections as shown in Figure 1.9. One is the high-pressure driver section and the second is the low-pressure driven section. A thin diaphragm is used to separate the high-pressure and the low-pressure section. Driver section and driven section contain an inert gas and a fuel-oxidizer mixture of interest, respectively. A sharp object or electric current is used to break the diaphragm instantly. After the diaphragm breaks, a

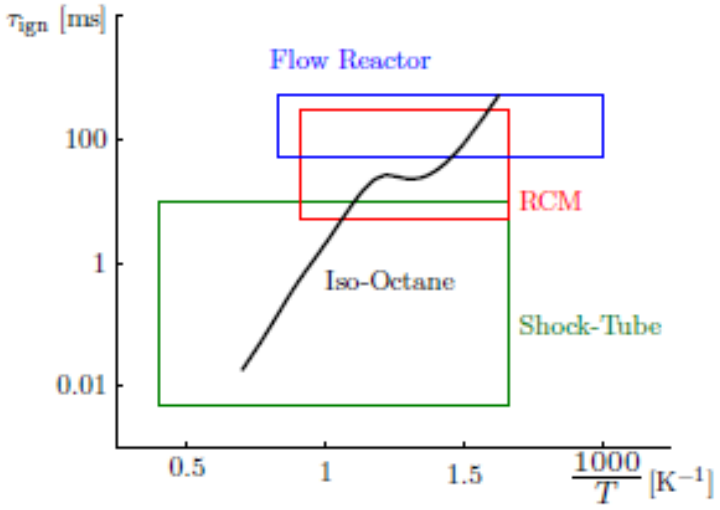

Figure 1.8: Typical operational boundaries of shock tube, rapid compression machine, and flow reactors.[31]

shock wave travels from the high-pressure section to the low-pressure section. This shock wave heats the gas in the driven section. Simultaneously an expansion wave travels in the driver section. The propagating shock reaches the end of the test section and reflects back after hitting the tube wall. This reflected shock wave collides with the incoming shock wave. The collision of shock waves causes a further increase in pressure and temperature of the test mixture. Combustion behavior of fuels are studied behind the reflected shock environment because it provides a perfect quiescent environment to study high-temperature reaction phenomena. The timing of interaction of the reflected shock and the incoming shock can be manipulated by varying the length of driver section and the driven section [34]. Pressure transducers and tunable diode laser absorption spectroscopy (TDLAS) are used for analyzing combustion gases behind the reflected shock wave [34].

- **1.4.3.2 Rapid Compression Machines**

Rapid compression machines (RCMs) are similar to a single stroke internal combustion engine. In RCM operation, a premixed fuel-oxidizer mixture is injected into the RCM reaction chamber and compressed by a piston. The piston in the chamber moves quickly, so heat losses through the reaction chamber wall are assumed to be negligible. The compression causes the unburned

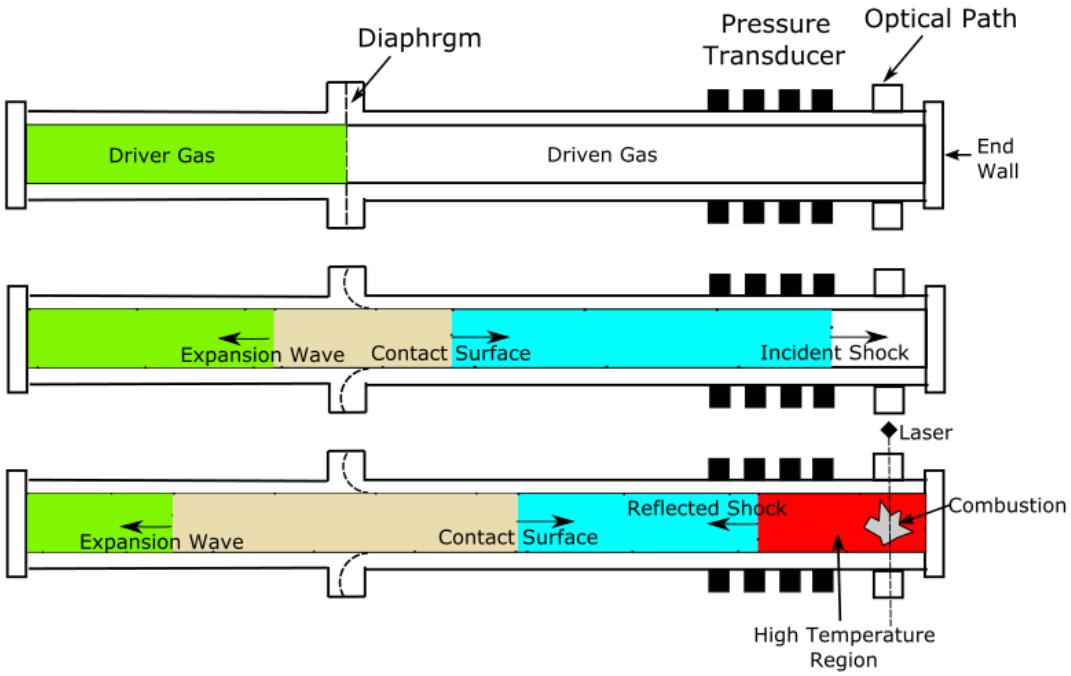

Figure 1.9: Schematic of shock tube operation.

fuel-oxidizer mixture to ignite by reaching high pressure and temperature. After reaching the top dead center, the piston is locked which creates a constant volume combustion chamber. Optical diagnostic is also used in conjunction with pressure evaluations in the reaction chamber to analyze combustion phenomena inside the reaction chamber [98, 31, 32]. Figure 1.10 displays an example for the pressure history of the RCM reaction chamber [31]. The first pressure increase is due to the initial piston compression stroke. After completion of the compression stroke, the piston reaches the top dead center, and the pressure remains almost constant. A slight decrease in the pressure after completion of the initial compression stroke is attributed to heat losses from the reaction chamber. After an ignition delay, the fuel-air mixture ignites. The difference in the time between the maximum pressure reached due to compression stroke and the sudden pressure rise due to the ignition of the fuel-oxidizer mixture is known as ignition delay. RCMs are capable of studying slow reactions with large ignition delay values. Ignition delay measurements in an RCM machine are prone to error due to a non-uniform temperature in the reaction chamber and heat loss through the wall of the reaction chamber [31, 32].

- **1.4.3.3 Plug Flow Reactors**

The plug-flow reactor (Figure 1.11) is a tubular reactor, where gases composition and temperature are uniform across a radial section, but vary along the axial direction [28]. Plug flow reactors can be modeled as flow passing through a series of infinitely thin well-stirred sections [28]. In plug flow reactors, fuel and air mixture moves in the tube and ignites after moving some distance along the

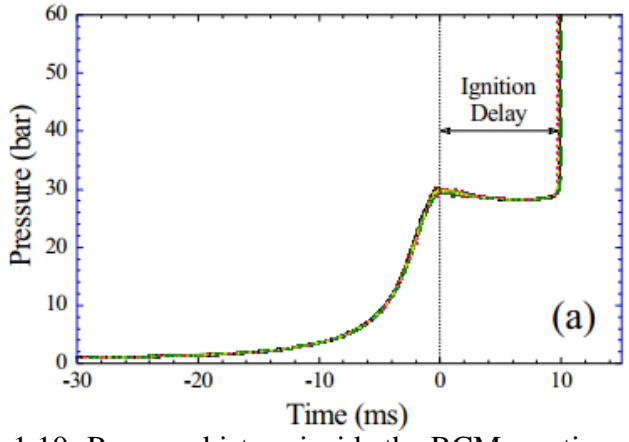

Figure 1.10: Pressure history inside the RCM reaction chamber. [31]

reactor. The time difference between perfect mixing and ignition point is defined as auto-ignition delay time.

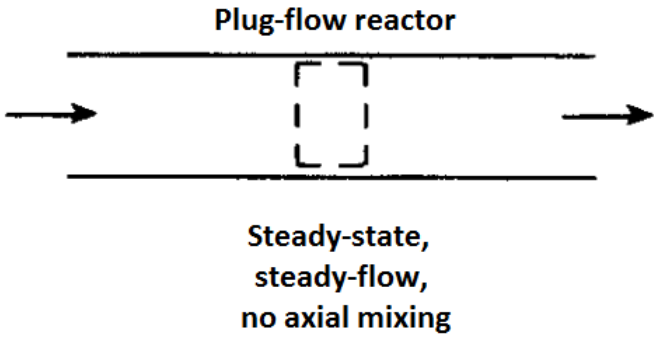

Figure 1.11: Plug-flow reactor. [102]

1.4.4 Laminar Flame Speed

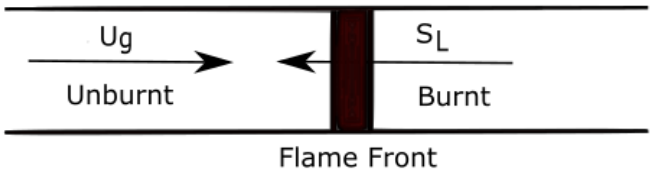

Figure 1.12: Laminar flame in 1D.

Flame propagation behavior is an important parameter to probe laminar-turbulent flame transition and turbulent flame propagation inside the engine cylinder. The laminar flame speed is used to characterize the flame propagation behavior inside the engine combustion chamber [83, 18, 44].

The laminar flame speed is a thermo-physical parameter of a combustible mixture and can be illustrated in a one-dimensional laminar region through an infinitely thin flame model as shown in Figure 1.12. An unburned fuel-air mixture enters through one end of the duct with a speed u_g, and a flame front consumes the unburned fuel-air mixture with a speed S_L. The flame is characterized as the thin interface between unburned and burned mixture [55, 28]. The propagation speed of this thin surface is known as laminar flame speed, or laminar flame speed is a speed at which unburned gases pass through the reaction wave in the normal direction of the reaction wave [55, 28]. This can also be called as the adiabatic laminar flame speed if the heat generated by chemical reactions only transfer to the the unburned mixture, not to walls. Since the flame front moves at a subsonic

speed, it is also known as deflagration speed. The laminar flame speed is a strong function of pressure, temperature, and unburned mixture equivalence ratio.

Several theories have been given to define the laminar flame speed. Mallard and Le Chatelier used a simple physical approach where the heat transfer from the unburned mixture to the burned mixture governs the flame propagation behavior [60, 58, 55, 28]. The unburned mixture is separated from the burned mixture by a thin boundary known as the thermal flame thickness. The thermal flame thickness is further divided into a preheat region (towards unburned region) and a reaction zone (towards the burned region). The thermal theory states that the flame propagates by conducting heat from the reaction zone to the preheat zone. This heat should be sufficient to increase the temperature of the unburned mixture to its auto-ignition temperature. By applying the energy conservation equation across the flame thickness, Mallard and Le Chatelier gave an expression of the flame speed (Equation 1.11) in terms of the thermal diffusivity and the chemical reaction rate.

$$S_L = k(\alpha\omega)^{\frac{1}{2}} \tag{1.11}$$

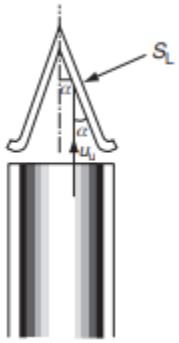

Figure 1.13: Bunsen core flame in the conical stationary flames method. [28]

Zeldovich, Frank-Kamenetskii, and Semenov have developed the second theory, which includes heat and diffusion of molecules [90, 55, 28]. This theory has not included radical diffusion from the reaction zone to the preheating zone. The third theory is the comprehensive theory, which has included radicals diffusion. According to the third theory, momentum, heat and mass transfer are conserved across the flame thickness.

Conical stationary flames, flames in cylindrical tubes, soap bubble method, closed spherical bomb

method, and flat flame burner are well known experimental configurations used for laminar flame speed measurements [58, 9, 8, 28, 39, 44].

In the conical stationary flames method, a premixed fuel/air mixture flow up a cylindrical tube. The premixed fuel/air mixture burns in a Bunsen cone flame shape at the opening of the tube as shown in Figure 1.13. The cone slant angle (α) is used to determine the laminar flame speed (S_L), which gives $S_L = u_u \sin\alpha$. In the cylindrical tubes method, a premixed fuel/air mixture is put in a horizontal tube open at one end. The premixed fuel/air mixture is ignited at the open end of the horizontal tube. The laminar flame speed is determined by calculating rate of progress into the unburned fuel/air mixture. In the soap bubble method, a premixed fuel/air mixture is put in a constant pressure soap bubble. The premixed fuel/air mixture at the center of the soap bubble is ignited by a spark. The laminar flame speed of the fuel/air mixture is determined by imaging the outward growth of the radially propagating flame.

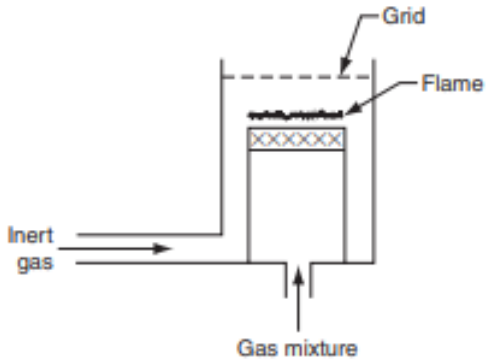

Figure 1.14: Flat flame burner apparatus. [28]

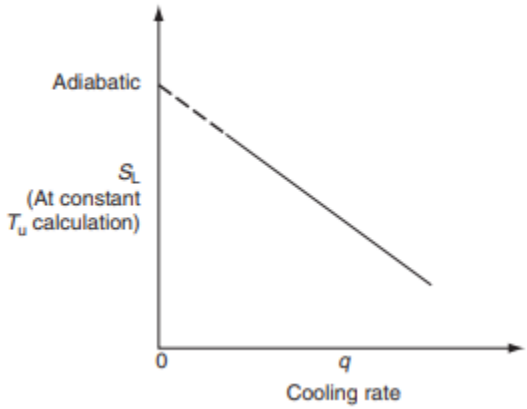

Figure 1.15: Flame speed vs cooling rate. [28]

In the closed spherical bomb method, a premixed fuel mixture is put in a constant volume spherical bomb. Similar to the soap bubble method, the mixture is ignited at the center of the bomb, and a flame front travels radially outwards. The pressure varies with the flame front because of a constant volume condition inside the closed spherical bomb. Pressure transducers are installed in the spherical bomb, and pressure data with optical diagnostic is used to determine the laminar flame speed [28].

In the flat flame burner method (Figure 1.14), a flat flame is stabilized on a porous disk. Plug cooling is used to stabilize the flame front closer to plug. Firstly, the flame is ignited with a high flow velocity than the flame speed, and cooling is managed to obtain a flat flame. Multiple cooling rates are used for a given gas mixture. Figure 1.15 shows that the adiabatic laminar speed is obtained by plotting flame speed as a function of cooling rate and extrapolating it to zero-cooling rate.

1.4.5 Surrogate Fuels

Combustion behavior of practical fuels depends on their composition. Gasoline, diesel, and bio-fuels are composed of various types of hydrocarbons. Compositions of these practical fuels also change depending on crude oil sources and refining processes. The highly complex nature of practical fuels poses challenges in relating their combustion behavior because of variation in their composition. Chemical kinetic modeling of practical fuels is also difficult since kinetic mechanisms are not available for each fuel molecule. To overcome this problem, surrogate fuels are developed. Surrogate fuels are composed of limited numbers of pure compounds of real fuels for research and kinetic modeling purpose. Surrogate fuels provide the luxury of conducting experiments with a well-understood fuel.

1.5 Co-Optimization of Fuels Engines (Co-Optima) Initiative

According to the Energy Independence and Security Act of 2007, 36 billion barrels of renewable fuels should be used by 2025 [74]. Bio-fuels are produced by breaking biomass molecules using chemical reactions and fermentation. To make new bio-fuels practical for future transport, chemical kinetics, fuel chemistry, and GHG emissions of bio-derived fuels are essential to be studied at

the whole vehicle level. Critical steps in a transition towards sustainable bio-fuel sources involve identification of promising bio-fuels, critical fuel properties and finding engine efficiency gains by engine-fuel co-optimization efforts.

The Co-Optimization of Fuels & Engines (Co-Optima) is an initiative of the United States Department of Energy (DOE) for high-performance fuel and engine research and development. The underlying concept of Co-Optima fuel research is the "central fuel hypothesis," which links engine performance to critical fuel properties [72, 22, 26, 64]. The hypothesis can be summarized as follows: "If target values for critical fuel properties that maximize efficiency and reduce harmful emissions for a given engine architecture are identified, then fuels that have properties with those values (regardless of chemical composition) will provide comparable performance [72, 22, 26, 64]." This hypothesis forms the basis of a fuel-tiered screening approach (shown in Figure 1.16), which has been used to identify promising bio-fuel candidate that are comparable or better than petroleum-derived fuel in engine performance.. The fuel tiered screening approach is sub-divided into three tiers. The first tier corresponds to the high-level screening where basic chemical and physical properties (RON, MON, Flame Speed, etc.) of fuel feed-stock candidate will be evaluated. In the second tier, critical fuel properties of high potential bio-fuel feed-stock candidate are related to the engine efficiency. Potential of feed-stock candidates are finalized by analyzing economics and commercial aspects in the third tier.

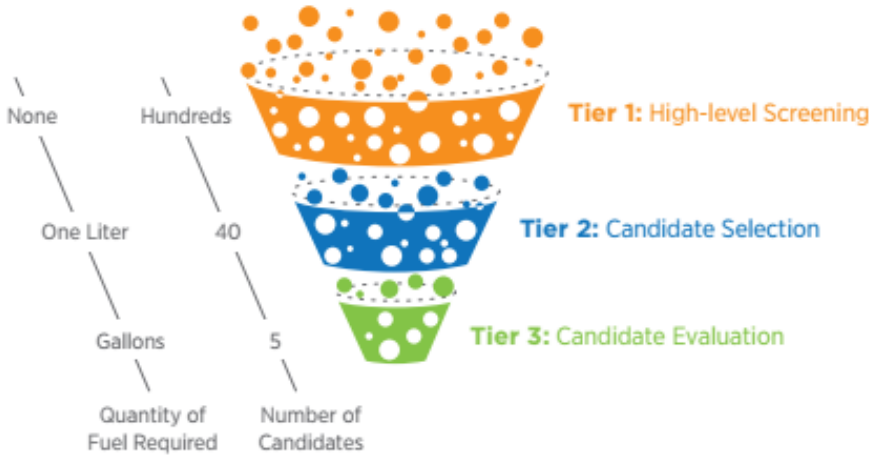

Figure 1.16: Tiered screening approach. [72]

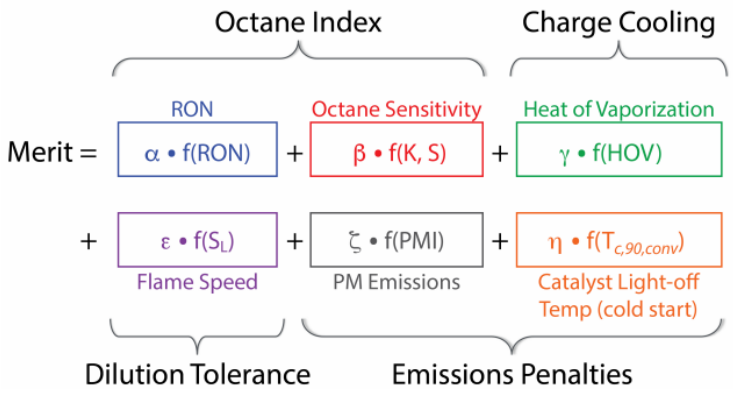

Figure 1.17: Engine merit function. [72]

1.5.1 Fuel Merit Function

The fuel merit function is a metric developed by DOE research teams in 2016 to characterize the potential fuel thermal efficiency gain when multiple interacting fuel properties are changing together [72, 22, 26, 64, 73]. An expression of fuel merit function is shown in Figure 1.17. The fuel merit function magnitude indicates the relative gain in the engine thermal efficiency when a new fuel blended into a gasoline reference fuel. The fuel merit function takes consideration of RON, MON, flame speed, heat of vaporization, exhaust emission, and various other fuel properties as shown in Figure 1.17. The gasoline reference fuel has a RON of 91 and a MON of 83. It is assumed that the gasoline reference fuel has an ethanol mole fraction of 0.21 corresponding to a Heat of Vaporization of 415KJ/Kg, a laminar flame speed of 46cm/s, a particulate emission of 0.2, and a stoichiometric air-fuel ratio of 14.

The step by step DOE co-optima roadmap can be summarized as follows:

* Find high potential biofuel feedstocks with desirable fuel properties and narrow down potential biofuel candidates further.

* Evaluate the combustion properties of high potential bio-derived fuels.

* Establish the relationship between the chemical structure of new fuels to their engine performance.

* Study the effect of blending of biofuels with gasoline on its combustion behavior.

* Develop a fuel properties database for new bio-derived fuels and their gasoline blends.

* Maximize the engine merit function by co-optimizing both fuel and engine architecture together.

Within the project a large number of bio-fuels are being proposed, but the applicability of these fuels to current engine architectures are still actively researched because of a limited availability of fuel property data. DOE and other research organization are using the fuel tiered screening approach to find the applicabilities of new bio-fuels to current engine architectures. The production costs and rates of bio-fuels under research phase scale poorly with CFR engine. The production rates of these fuels ($\sim$ml/hour) are small, and production cost are very high ($\sim$100 ml for 10K \$). CFR engines require a large amount of fuel ($\sim$2-4 liter) to characterize fuel properties, which makes them unsuitable for research of new bio-fuel candidates. A major obstacle in generating an extensive fuel property database and accelerating bio-fuel research is the limitation in the ability to rapidly test a large number of bio-derived blend-stocks. The challenge is to find an alternative fuel testing device, which can provide rapid testing ability and can characterize fuel properties of a new bio-fuel candidate at a stage when only a small quantity of fuel is available.

1.6 Method

Through this work, propose an externally heated millimeter scale microcombustor as an alternative fuel testing device for research and testing of small samples of fuels. The purpose of this work is to make a small sample fuel tester device to accelerate fuel research and getting big fuel data at low cost. The primary objective of this thesis is to determine whether FREI and strong flames inside an externally heated microcombustor can be used for fuel research and characterization. The research work presented here is based on experiments performed in an externally heated microcombustor. A machine vision camera and a thermocouple translational stage setup are used for experimental analysis of combustion phenomena inside the microcombustor. Gaseous fuels with different molecular structures are tested and compared to understand the impact of fuel molecular

structure and fuel properties on combustion properties. The experimental setup can give the estimation of some important fuel properties like ignition, extinction, and flame propagation behavior. Another significant aspect is to understand the applicability of microcombustor results to combustion phenomena at engine relevant pressure. 2-dimensional transient simulations in OpenFOAM are performed to study the combustion behavior inside the microcombustor for engine relevant pressure. Overall, this setup has potential applications to test bio-based renewable fuels and other alternative fuels. Small sample testing can differentiate desirable fuel properties for advanced engine performance and accelerate fuel research.

1.7 Structure of the Thesis

This thesis contains five chapters. Chapter 2 discusses the theory of microcombustion and its application for fuel studies. Chapter 3 focuses on the experimental analysis of gaseous fuels in an externally heated microcombustor. A detailed explanation of the experimental setup is given and experimental results are discussed. 2D transient numerical simulations of microcombustor at engine relevant pressures are discussed in Chapter 4. Governing equations, numerical methods with the geometry of domain, numerical cases, and results are described in detail. Conclusions and recommendations are stated in Chapter 5.

Chapter 2
Microcombustion

2.1 Introduction

A combustor is called a microcombustor if its length scale is comparable to the flame thickness. In microcombustion, combustion parameters such as the flame thickness, the flame speed, and the adiabatic flame temperature remain similar to large-scale combustion [24]. A microcombustor is heavily affected by surface heat losses because as the combustor size decreases, surface heat losses from the flame front increase due to a higher surface-area-to-volume ratio [24, 61, 45]. Premixed flames extinguish in small diameter tubes due to heat losses to walls and radical quenching at the wall. For a flame to propagate through a small diameter tube, the rate of heat release by chemical reactions inside the flame must be greater than or equal to the rate of the heat loss from the flame. The minimum diameter of a circular tube in which a flame extinguishes, rather than propagates, is denoted as the quenching distance or quenching diameter [28]. The quenching diameter is inversely proportional to the square root of the temperature, i.e. it decreases with increasing temperature, hence the flame can pass through much small diameter tube at high temperatures [28, 24].

Heat recirculation and external heating were successfully used to overcome wall quenching issues in Swiss-Roll microcombustors and externally heated microcombustors, respectively [92, 104, 91, 51, 62, 63, 54, 101, 88]. This work proposes an externally heated microcombustor for fuel research and testing.

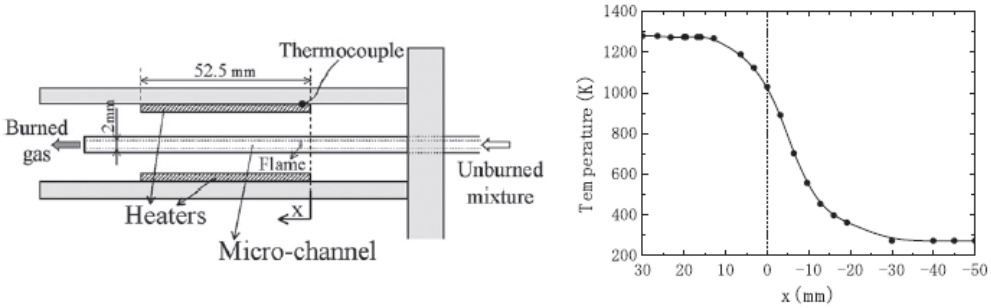

Figure 2.1: Externally heated microcombustor experimental set-up with a parallel plate heater. [62]

In externally heated microcombustors, external heating enables a premixed flame to stabilize in a microcombustor by compensating for wall heat losses [24]. The hot wall increases the tube

inner gas phase temperature and reduce quenching diameter. Several different externally heated microcombustor experimental setups have been reported in the literature [36, 37, 63, 62, 101, 94, 95]. A typical externally heated microcombustor setup has a quartz tube of a diameter smaller than the standard quenching diameter [36, 37, 63, 62, 101, 94, 95]. In initial studies electric parallel-plat heaters are used to externally heat the quartz tube by Maruta and co-workers as shown in Figure

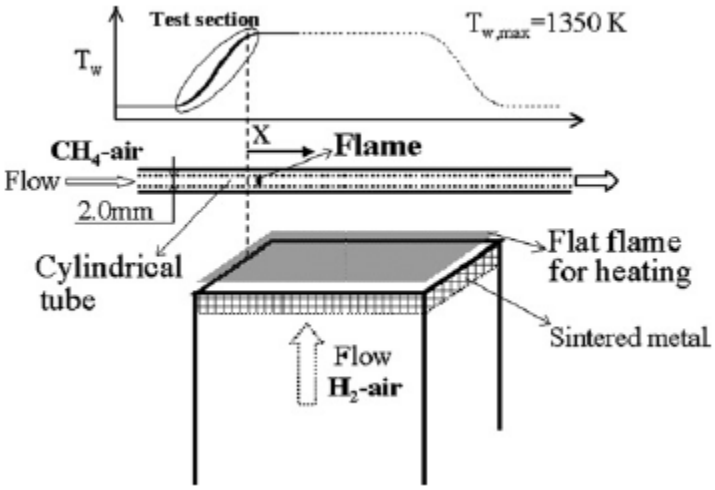

Figure 2.2: Externally heated microcombustor experimental set-up with a flat flame burner. [101]

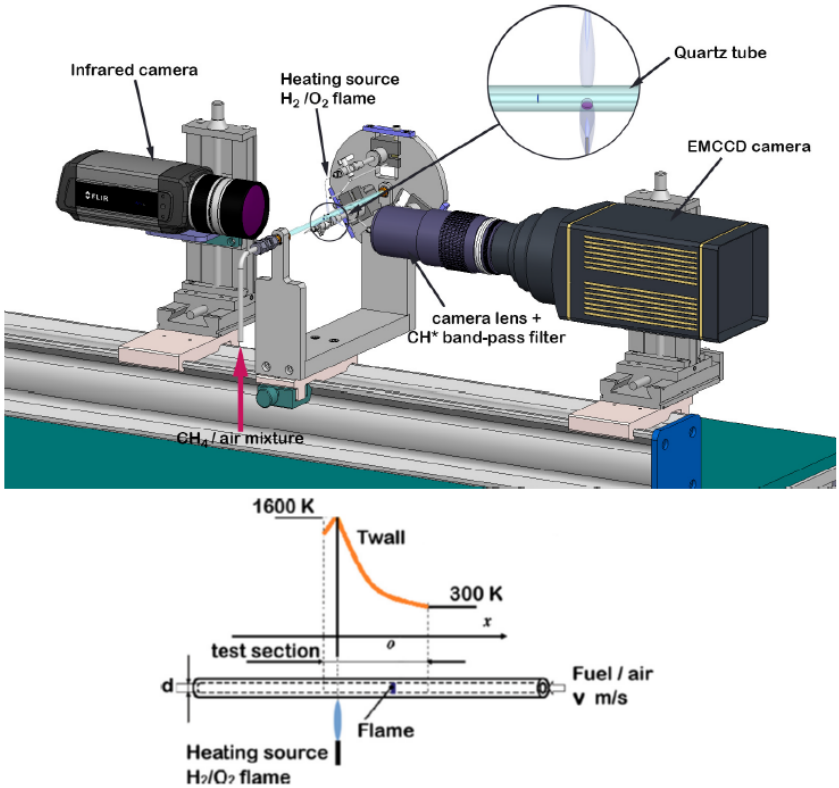

Figure 2.3: Externally heated microcombustor experimental set-up used by Stazio et al. [94]

2.1 [63, 62]. A stationary temperature profile with a positive gradient along the surface of the inner wall of microcombustor is achieved through heating by the parallel plate heater is shown in Figure 2.1. This stationary temperature profile forms across the test section of the tube because half of the test section is unheated and half is heated externally. In following studies, a flat flame burner is used to externally heat the quartz tube instead of parallel plate heaters as illustrated in Figure 2.2 [36, 37, 101]. Both parallel plate heater and flat flame heater ensure a controlled and continuous temperature profile along the inner wall of the quartz tube. In an alternate configuration introduced by Di Stazio et al. [94, 95], three blowtorches fueled by a H_2/O_2 mixture are used to heat the tube externally as shown in Figure 2.3. All three torches are placed at an equal distance at a 120^{o} angle. Heating by blowtorches provides a continuous and controlled temperature profile with a Gaussian temperature distribution along the tube. Each external heating method provides sufficiently high temperatures to self-ignite the unburned fuel-air mixture overcoming quenching issues. Most studies use H_2/O_2 mixtures for the external flame so that the external flame is free of CH* chemiluminescence, and microcombustor flame CH* chemiluminescence is easy visible. High-speed cameras and intensified (ICCD) cameras are used in the literature to capture flame movement inside the microcombustor. Thermocouples have been reported in the literature for externally heated microcombustors temperature measurements [63, 62, 54]. Di Stazio et al. [94, 95] used a thermal infrared camera as a non-intrusive device to measure microcombustor outer wall temperatures.

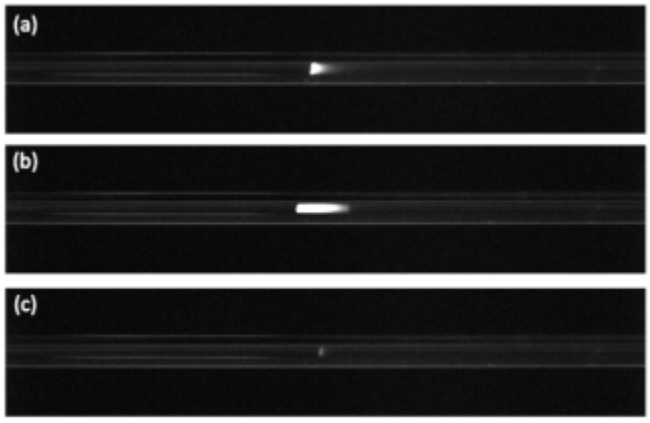

Figure 2.4: Flame images inside an externally heated microcombustor : (ϕ= 1.0); (a) normal flame (V_t = 80 cm/s), (b) FREI (V_t = 50 cm/s), and (c) weak flame (V_t = 7.5 cm/s). [70]

2.2 Flame Dynamics Inside Externally Heated Microcombustors

Various combustion regimes are observed inside an externally heated microcombustor: strong and stable flames at high flow rates, self-excited oscillatory Flames with Repetitive Extinction and Ignition (FREI) at intermediate flow rates, and weak stable flames at marginal flow rates (Figure 2.4) [63, 62, 101, 80, 108]. Time histories of luminous zones of strong flames and FREI inside the microcombustor with respect to unburned mixture velocities are shown in Figure 2.5. A strong flame exhibits a constant luminosity because it stabilizes at a fixed point in the microcombustor. In FREI, flames ignite and extinguish periodically. Because of periodic motion inside the microcombustor, FREI show a changing luminosity with respect to both time and positions. Extremities of FREI traces represent FREI Ignition and extinction points in Figure 2.5.

2.2.1 Strong Flames

Strong flames are observed at high flow rates [63, 62, 101]. A strong flame is a flat, stationary, and non-adiabatic flame, which stabilizes at a location where the unburned mixture flow velocity balances out the local flame speed [108]. The unburned mixture flow velocity is typically higher than the adiabatic laminar flame speed at the strong flame stabilization point. Strong flames stabilize in the temperature gradient region of the tube wall by preheating of the unburned mixture and can exist at low temperatures.

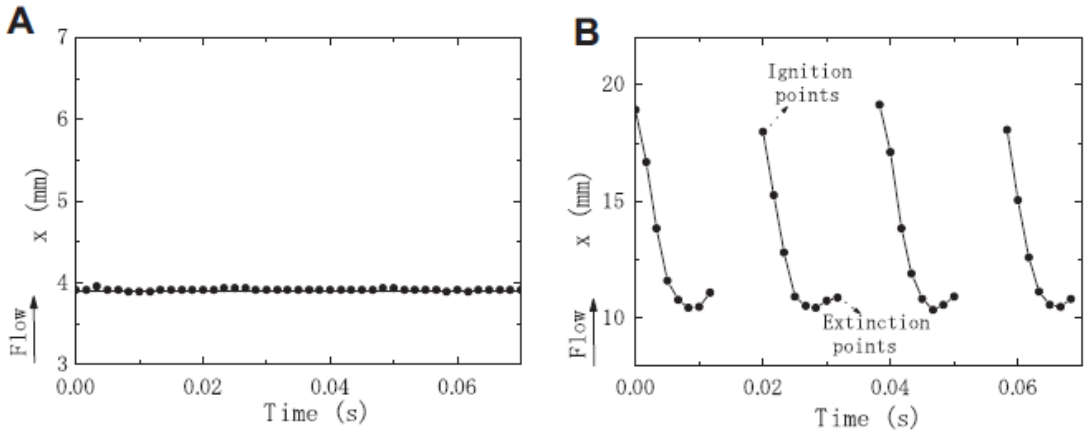

Figure 2.5: Time histories of (A) strong flame and (B) FREI inside an externally heated microcombustor. [62]

2.2.2 Flames with Repetitive Extinction and Ignition (FREI)

Flames with Repetitive Extinction and Ignition (FREI) form well defined, self-excited instabilities that occur in premixed combustion in an externally heated microcombustor at moderate flow rates. FREI are attributed to a Hopf-bifurcation phenomenon where a stable flame switch to an oscillatory flame behavior [68, 65, 85]. Several numerical studies have been reported in the literature to understand the FREI dynamics [65, 71, 85, 86]. At intermediate flow rates, the unburned premixed fuel-air mixture enters from the inlet and ignite downstream after gaining sufficient heat from the tube wall. The flame front travels to upstream continuously losing heat where it quenches due to large heat losses to comparable cold tube walls. After a time period, the tube fills with a fresh unburned mixture, and re-ignition occurs at the same ignition point followed by extinction towards the upstream side. This periodic phenomenon repeats itself at frequencies ranging from tens to hundreds of Hertz [63, 62, 85, 94]. At slow shutter speeds, FREI appears as a thickened combustion zone because the flame front oscillates with a very high frequency, but high-speed imaging and acoustic measurements reveal the underlying flame instability with repetitive extinction and ignition. Extinction and re-ignition terms used here are according to the definition suggested by Miyata et al. [67].

2.2.3 Weak Flames

This is a "weak" combustion phenomenon, which occurs at marginal flow rates [62, 101]. Since the diffusion heat transfer from the upstream is negligible at marginal flow rates, the weak flame stabilizes downstream (hot side) by heat transfer from the tube walls only. The weak flame does not propagate after the ignition and stabilizes close to the ignition point [108]. Since weak flames have very low luminosity, a long exposure time is required to capture their image. Due to a dominating impact of mass diffusion in the low flow velocity region, the weak flame has a widened reaction zone in comparison to a stable flame [101].

2.3 Microcombustion for Fuel Research

In previous studies, externally heated microcombustors are used for fundamental combustion studies and chemical kinetics validation [80, 108, 37, 36, 99, 69, 49, 50]. Maruta and co-workers have

used weak flame behavior inside the micro-reactor with a controlled temperature profile to investigate fuels ignition properties [80, 108, 37, 36, 99, 69, 49, 50, 101]. Figure 2.6 presents an overview of results by Maruta and co-workers on fuel dependence of weak flames [108, 37, 36, 49]. Figure 2.6 clearly reveals that the position of weak flame luminosity is a function of fuel RON. As fuel RON decreases, the weak flame shifts towards the low-temperature region, which is equivalent to the weak flame ignition temperature decrease as RON decreases.

Several other fuel studies have been conducted using the micro-reactor with controlled temperature

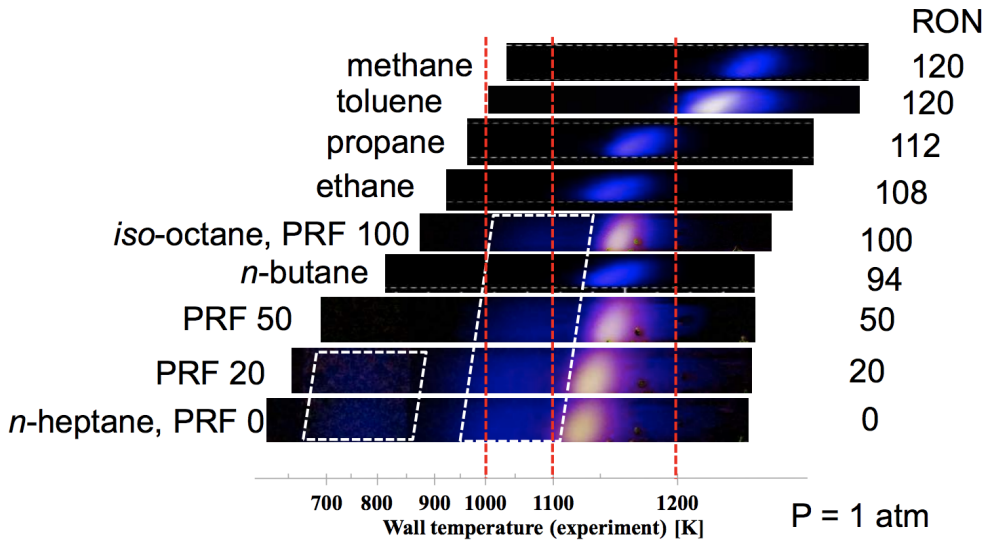

Figure 2.6: Weak flame dependence on Research Octane Number. [108, 37, 36, 49]

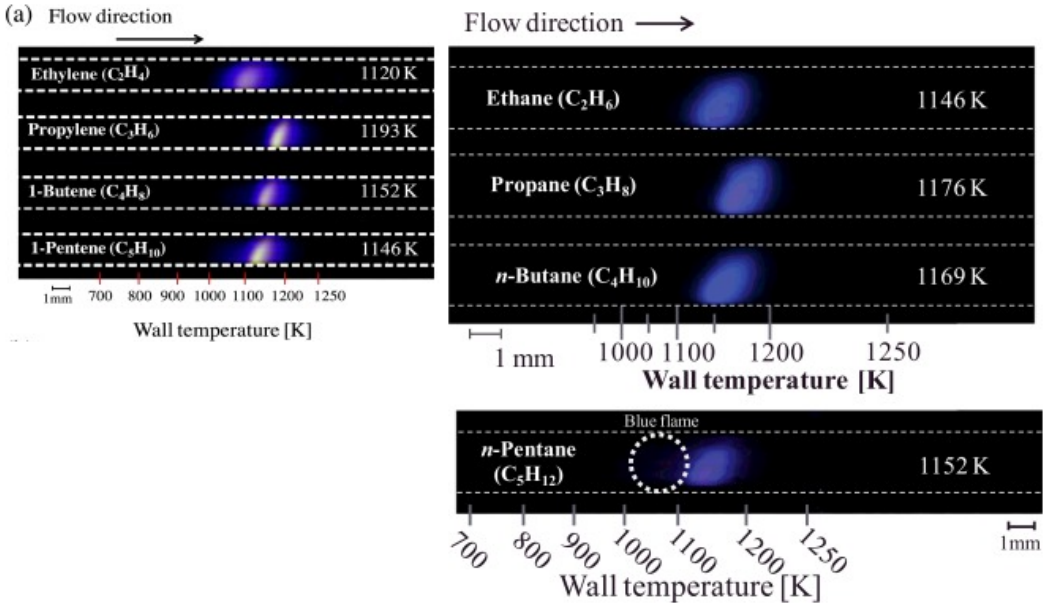

Figure 2.7: Weak flame dependence on fuel molecular structure. [49, 50]

profile. Suzuki et al. [99] have studied the Cetane Number dependence of diesel surrogate/air. Nakamura et al. [69] have used a micro-reactor for kinetic validation of ethanol mechanism. Kikui et al. and Kamada et al. [49, 50] have used a micro-reactor with a controlled temperature profile to study the impact of molecular structure on the ignition behavior of alkanes and alkenes and chemical kinetics validation. Figure 2.7 shows the difference in weak flame position/temperatures for different alkanes and alkenes. From Figure 2.7 it is apparent that the weak flame position is affected by its carbon chain length and presence of a double bond. In a recent study, Tezuka et al. [30] has introduced a vertical type micro-reactor to study PRF mixtures reactivity. This study shows that as equivalence ratio is decreased from 1 to 0.5, weak flames stabilize at lower temperatures, which indicates higher reactivate in low temperature region. All these previous studies with weak flames have confirmed that externally heated microcombustor with a controlled temperature profile could be used for fundamental combustion studies.

2.4 Previous Numerical Work on Microcombustion

Norton et al. [71] and Kurdyumov et al. [56] have used a single-step kinetic mechanism to understand the flame stability inside a microcombustor with a temperature profile. Kurdyumov et al. [56] have used a two-dimensional thermal-diffusive model (constant-density model) to prove that the flame-wall interactions are the reason behind self-excited instabilities like FREI. Despite the ability to identify flame instability region, single-step kinetic models are incapable of reproducing ignition and extinction phenomena, which have significant relevance in understanding the impact of pressure on ignition and extinction behavior of fuels inside the microcombustor.

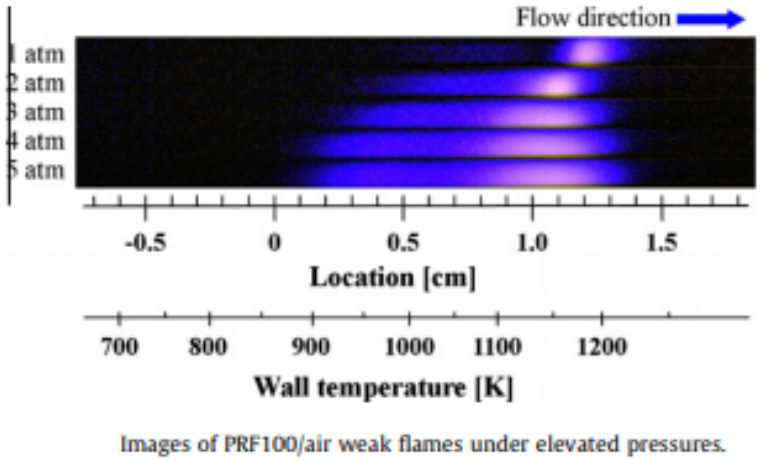

Figure 2.8: Pressure dependence of PRF100/air weak flame. [37]

FREI origin through a Hopf bifurcation phenomenon have reported in the literature [85, 86, 68]. In the mathematical theory of bifurcations, a Hopf bifurcation is a phenomenon where a stable solution switches to an unstable solution [11]. Minaev et al. have used a nonlinear analytical model to explain the bifurcation phenomena at the onset of the FREI oscillation. Pizza et al. [85, 86] have studied the ignition and extinction phenomena of FREI through direct numerical simulation with detailed chemistry and stated that ignition and extinction behavior caused by a loss of stability from a Hopf bifurcation. Fan et al. [19] have used a thermal-diffusive model to report the splitting flame dynamics of FREI. Nakamura et al. [68] have used the unsteady one-dimensional model to study the bifurcation behavior of FREI into two peaks and quasi-steady nature of FREI. Miyata et al. [67] have performed 2D FREI direct numerical simulations of methane-air mixture with GRI-MECH 3.0 for a 0.5 mm radius microcombustor. They have stated that a particular negative phase in total heat transfer through the wall causes FREI. This negative phase in heat transfer causes a heat re-circulation for preheating the incoming unburned mixture. Kishore et al. [52] have studied the impact of the the external temperature profile gradient on FREI behavior and reported that FREI ignition temperature decreases as the external temperature profile gradient decreases and FREI ignition occur closer to auto-ignition temperature of the fuel/air mixture for marginal temperature gradient values.

The impact of pressure on weak flame ignition behaviour inside a micro-reactor with a controlled

temperature profile has been studied both experimentally and numerically by Maruta and co-workers [37, 69]. Figure 2.8 shows weak flame ignition temperature decreases with increasing pressure, which is in direct correlation with fuel ignition behaviour inside engines [28]. Although elevated pressure weak flame studies have shown encouraging signs [37], none of studies have reported the impact of pressure on FREI.

Chapter 3
Experimental Analysis of Gaseous Fuels

The previous two chapters have discussed the motivation for this thesis work, some fundamental concepts of combustion, and earlier studies on externally heated microcombustors, where weak flames are used for fundamental combustion studies. Weak flames imaging needs high camera exposure because of their low chemiluminescence. This makes data acquisition time-consuming during weak flames experiments. Instead of weak flames, the current study seeks to investigate potential of FREI and strong flames for fuel characterization. FREI and strong flames provide high chemiluminescence, which will make fuel testing experiments high throughput. FREI also have in-built ignition, extinction, and flame propagation behavior, which could be helpful in characterizing bio-fuels combustion behavior. To gain insight into FREI and strong flame, an experimental setup of externally heated microcombustor is implemented. Low-speed imaging of CH^* chemiluminescence and wall temperature quantification via thermocouple measurements are used to quantify FREI ignition and extinction temperatures. The introduction of a low-cost microphone for pressure measurements is new and opens additional avenues for the characterization of FREI dynamics. Five gaseous fuels - methane, ethane, ethylene, propane, and dimethylether (DME) are experimentally investigated using the microcombustor experimental setup to study the impact of fuel chemistry. The respective impacts of the external temperature profile, microcombustor diameter, and mixture equivalence ratio are also investigated. Firstly, this chapter discusses the details of the experimental setup followed by data processing. Finally, the chapter concludes by discussing experimental results.

3.1 Experimental Setup and Methods

A detailed schematic diagram of the experimental setup is shown in Figure 3.1. The experimental apparatus consists of two flow delivery systems, a McKenna flat flame burner, a quartz tube microcombustor, a thermocouple-translational stage system, an imaging setup, and a microphone device. A closer view of the experimental setup is shown in Figure 3.2.

Two flow delivery systems are used to supply premixed fuel/air mixtures to the McKenna burner

and the microcombustor. Premixed fuel/air delivery is dedicated for each system, i.e. one line supplies premixed test fuel/air mixture to the microcombustor and the second line delivers the premixed H_2/air to the McKenna burner. H_2 and air for the McKenna burner are supplied by using a pressurized H_2 cylinder and an external air compressor, respectively. Gaseous fuel and

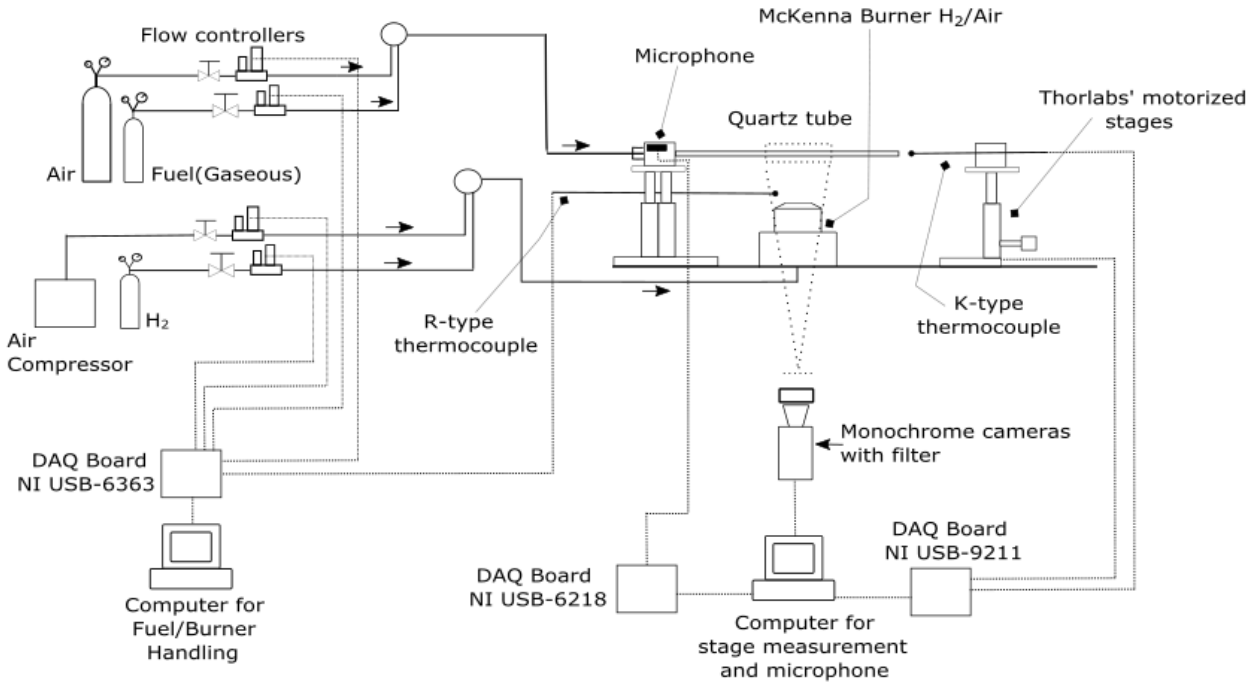

Figure 3.1: Schematic of the experimental setup.

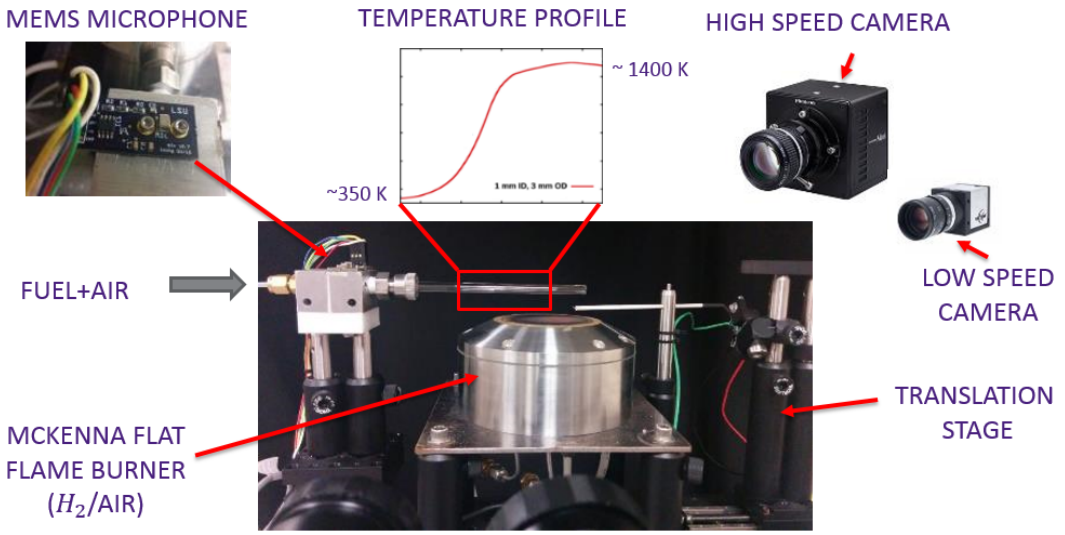

Figure 3.2: Experimental apparatus, including McKenna Burner, quartz tube microcombustor, microphone, translation stage, high-speed and low-speed cameras. A temperature profile is shown across the 50 mm quartz tube section.

air are supplied to the microcombustor from pressurized cylinders. Experimental conditions are specified by velocities and equivalence ratios for quartz tube (v_{tube}/ϕ_{tube}) and McKenna burner (v_{burner}/ϕ_{burner}), respectively. Fuel and air flow rates are controlled by using Cole-Parmer Mass Flow Controllers (MFCs). Detailed information about all Cole-Parmer MFCs of the experimental setup is given in Table 3.1. A Cole-Parmer MFC measures the volumetric flow rate by creating a pressure drop across a laminar flow element and has a fast response time in comparison of thermal mass technologies due to no warm-up time. Gas mass flow rates in a Cole-Parmer MFC are corrected for different gas densities via ideal gas and compressibility properties.

The microcombustor chosen for the work is a one-millimeter diameter fused quartz tube. The diameter of the quartz tube is chosen to be less than the conventional quenching diameter of gaseous alkane (C_1-C_8) fuels, as FREI behavior is exclusive to tubes having a smaller inner diameter than the quenching diameter. Fused quartz is chosen as the microcombustor material because of its high melting point ($\sim$2000K). Fused quartz also has a very low thermal expansion ($5.5\,e{-}7\frac{cm}{cm^oC}$) and excellent thermal shock resistance.

External heating to the quartz tube microcombustor is provided by a McKenna burner (Holthuis & Associates, steel plug, shown in Figure 3.3), which is operated with H_2/air mixture to eliminate external CH^* signals. McKenna laboratory burners are flat flame burners, which have been used to provide a well-characterized flat flame in combustion experiments.

Temperature measurements are dedicated per system, i.e. McKenna burner and microcombustor are separate systems. The McKenna burner flame temperature is measured by placing R-type

Table 3.1: Cole-Parmer Mass Flow Controllers model number, operating range, and accuracy.

Gas	MFC Model	Operating Range	Accuracy
C_3H_8 (Tube Fuel)	EW-32907-55	0.1–10 sccm	±0.8% of reading ±0.2% full-scale
Air (Tube Air)	EW-32907-59	1–100 sccm	±0.8% of reading ±0.2% full-scale
H_2 (McKenna Fuel)	EW-32907-75	1–100 slpm	±0.8% of reading ±0.2% full-scale
Air (McKenna Fuel)	EW-32907-77	2.5–250 slpm	±0.8% of reading ±0.2% full-scale

thermocouple above the burner surface. The Omega K-type thermocouple (KMTXL-010E-12, 0.25 mm bead) is used with a precision translation stage (Thorlabs MTS50- Z8, 50 mm travel) to measure the microcombustor inner wall temperature profile. The Omega K-type thermocouple is a fine gauge thermocouple with an exposed tip. A microphone device is used to capture FREI pressure fluctuations.

A monochrome machine vision camera with a prime lens and an optical bandpass filter is used to capture flame CH^* chemiluminescence. The camera is an IDS (Imaging Development Systems) monochrome machine vision CMOS camera (UI-3240CP-M/C) with a sensor resolution of 1280×1024 pixels. The camera has a USB 3.0 interface. A Tamron prime lens with a 25mm focal

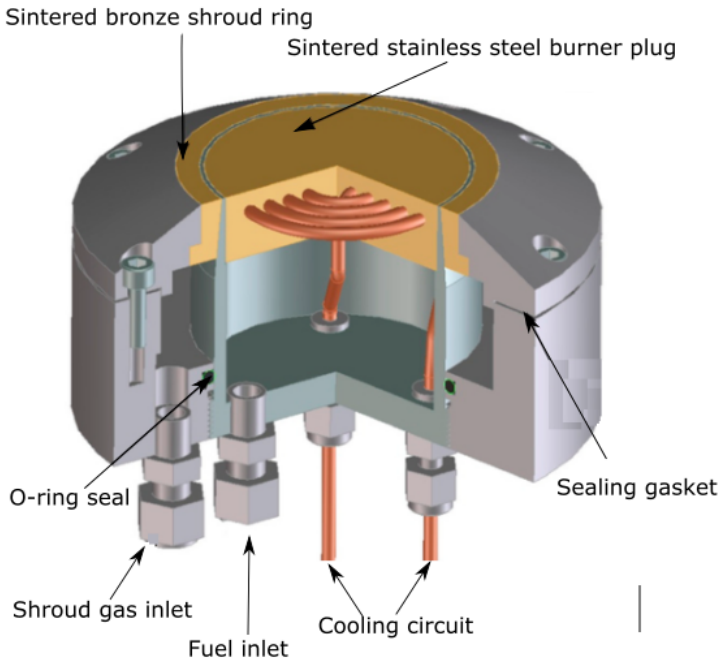

Figure 3.3: The Holthuis and Associates McKenna Flat Flame Burner Description. [13]

Figure 3.4: (A) IDS monochrome machine vision CMOS camera [29] (B) A Tamron prime lens [103].

length and $\frac{F}{1.4}$ aperture is used with the camera. The Edmund hard coated optical bandpass filter has a Center Wavelength (CWL) of 430nm and Full Width-Half Max (FWHM) of 10nm. Both monochrome machine vision camera and Tamron lens are shown in Figure 3.4.

Experiments are controlled through laptop PC/Desktop PC via LabVIEW programs and National Instruments Data Acquisition (DAQ) boards. Different LabVIEW Virtual Instruments (VI) are used to monitor the flow control system, microcombustor inner wall temperature measurements, and the microphone device. Flow controllers and the R-type thermocouple are controlled by one LabView VI and the K-type thermocouple with the translation stage is controlled by another LabView VI. The microphone device is controlled by a separate LabView VI. This work has used three NI DAQ boards for data acquisition and interfacing different measurement devices to the computer. The NI USB-6363 is used for managing flow controllers and the R-type thermocouple, the NI USB-9211 is used for thermocouple temperature measurements inside the microcombustor, and the NI USB-6218 is used for microphone data acquisition. A Lenovo Think-pad computer is used to manage flow controllers and the R-Type thermocouple. A separate Desktop computer is used to manage the K-type thermocouple translational stage system with and the microphone.

3.1.1 Microphone and FREI Frequencies

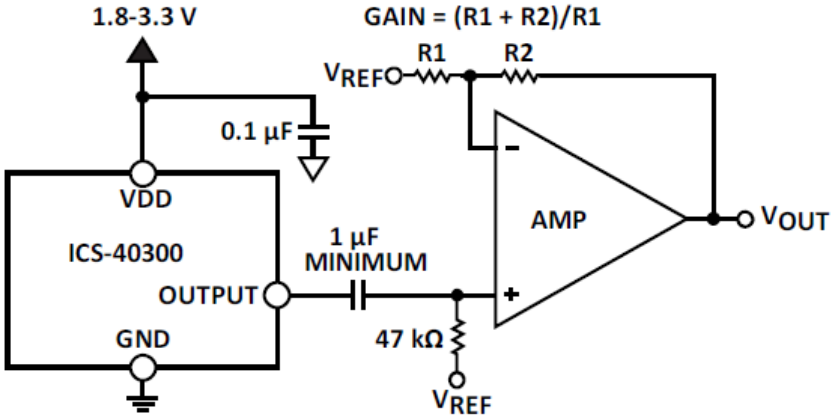

Figure 3.5: Microphone circuit diagram [42]

FREI frequencies are acquired through a MEMS microphone (InvenSense ICS-40300). The MEMS microphone has a frequency range 6 Hz-20 kHz. The circuit diagram of the microphone assembly

is illustrated in Figure 3.5. The microphone sensor is installed on a custom PCB. The custom PCB has a passive high-pass filter (f_c=3Hz) and signal amplification. Fundamental FREI frequencies are obtained using Fast Fourier Transform (FFT) on ten consecutive pressure measurements. Typical FREI frequencies are shown in Figure 3.6. A Photron SA3 monochrome high-speed camera is used with Nikon 50 mm $\frac{f}{1.2}$ lens and an Edmund 435±40 nm OD6 filter to capture the FREI CH^* emission. FREI reaction zone traces are constructed from videos acquired using high-speed

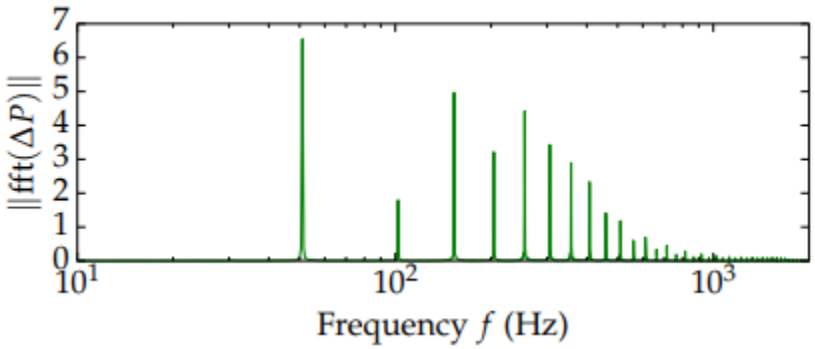

Figure 3.6: FFT magnitude for pressure signal shown in Fig. 3.7 reveals a base frequency of 51.25 Hz. (Credit: I. Schoegl)

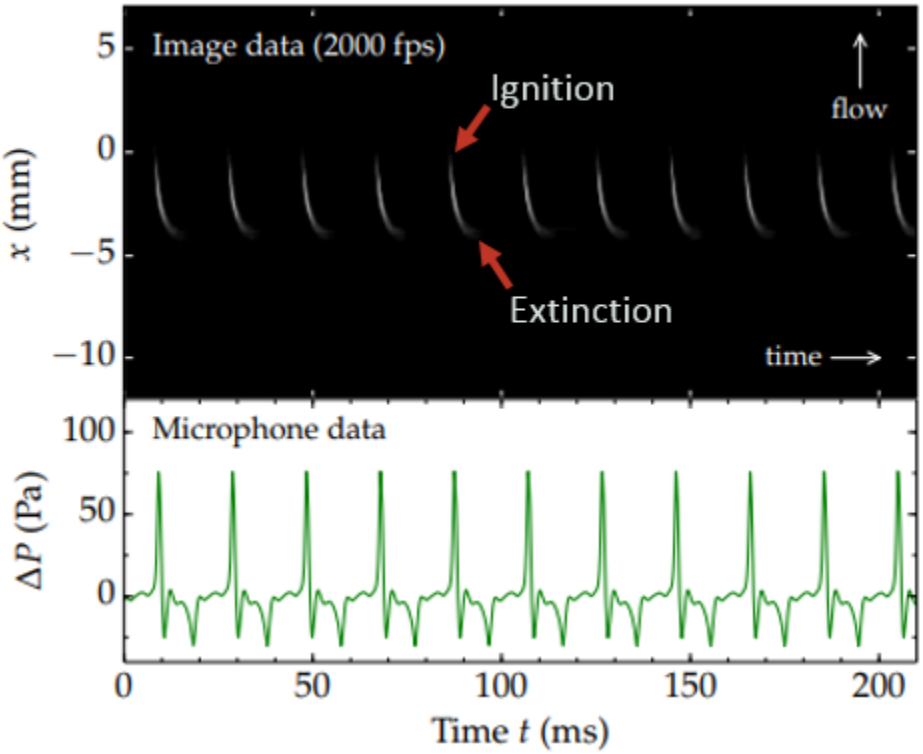

Figure 3.7: High-speed imaging data (flame traces) and pressure signal for FREI. (Credit: I. Schoegl)

camera. Figure 3.7 shows the correlation between pressure signals and FREI reaction zone traces. Figure 3.7 shows that sharp pressure peaks are found to coincide with ignition events in FREI cycle. Two negative pressure spikes are observed in each cycle, where the first is attributed to an acoustic pressure oscillation after ignition, and the second marks extinction. Figure 3.7 also shows the time histories of FREI locations. FREI locations show periodic behavior. In FREI, flames move inside the microcombustor and do not remain luminous at each time step, hence CH^* chemiluminescence traces are found to vary with both position and time. Flames start emitting CH^* chemiluminescence at the ignition point and keep emitting during their movement inside the microcombustor. At the end of the FREI cycle, flames extinguish. After a delay, reignition occurs in the upstream region, and FREI cycle repeats itself.

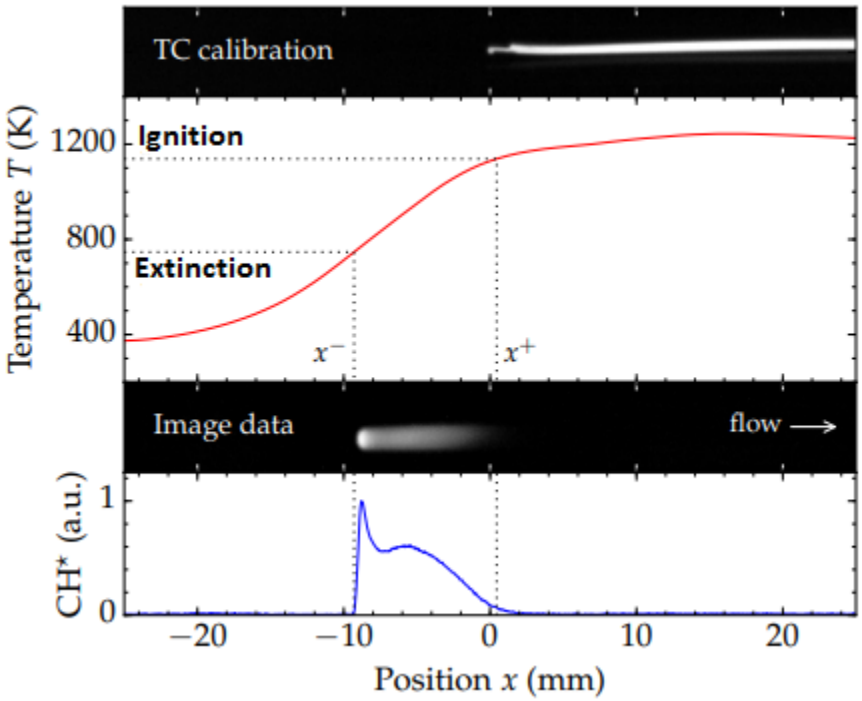

Figure 3.8: Data processing based on thermocouple data and low-speed imaging of CH^* chemiluminescence to capture upstream/downstream positions and temperatures (illustration for 2mm ID / 4mm OD quartz tube). (Credit: I. Schoegl)

3.1.2 Flames Locations and Temperatures

Flame positions inside the microcombustor are determined by using calibrated images. Calibration of the camera is achieved with respect to thermocouple bead locations as shown in Figure 3.8.

Images are processed using the Python Imaging Library (PIL) and the Python Scikit Library. This section discusses the procedure of flames locations and temperatures determination.

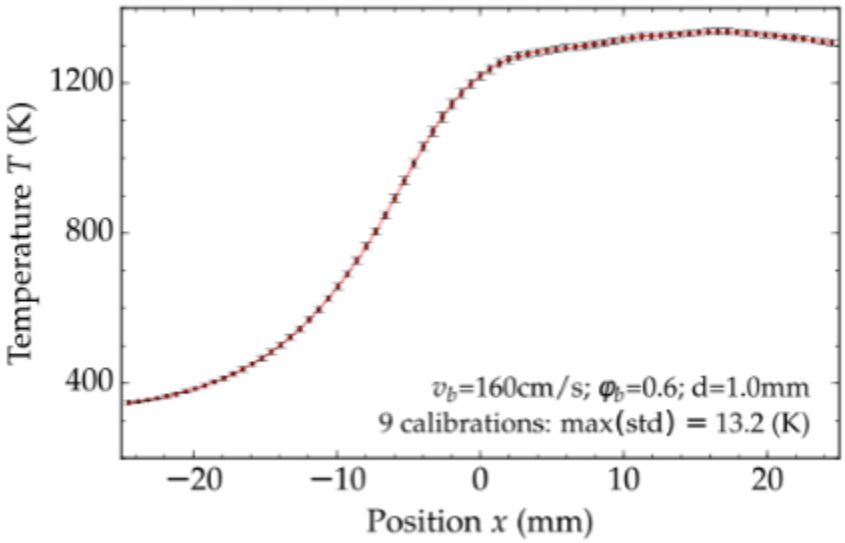

Figure 3.9: A typical microcombustor inner wall temperature profile. (Credit: I. Schoegl)

First, the camera is installed on the optical table. The camera lens is aligned parallel to the microcombustor surface. The K-type thermocouple is placed inside the microcombustor such that the K-type thermocouple bead is at the edge (x=0) and an image is taken. Another image is taken after moving the thermocouple bead 25 mm towards the burner center (x=25). Now, the K-type thermocouple is moved across the 50 mm section of the microcombustor from the cold side to the hot side. During the thermocouple motion, a constant flow of air at 30 cm/s is passed through the microcombustor. Wall temperature calibration data ($\sim$1650 points) are acquired. A typical microcombustor inner wall temperature profile is shown in Figure 3.9, where x = 0 mm corresponds to the edge of the McKenna burner plug. A maximum standard deviation of 13.2 K between temperature calibrations indicates excellent repeatability. Now the K-type thermocouple is removed from the microcombustor and premixed fuel-air mixtures are supplied to the microcombustor. Further low shutter-speed images of flames are obtained using the machine vision camera. The shutter speed of the machine vision camera is kept significantly longer than the period of FREI to capture multiple FREI events in each image. Flame images are acquired as video sequences of $\sim$30 frames with a rate of 2 frames per second. Consecutive frames of videos are extracted and analyzed. The

elongated FREI CH^* emission in a frame indicates the FREI extent from ignition to extinction. Figure 3.8 illustrates the calibration of image positions based on photographs of the thermocouple bead at center (x=0 mm) and stop position (x=25 mm; not shown). Once the FREI region is known, the extent of visible CH^* emission is quantified by upstream and downstream locations x^- and x^+, where a threshold value of 5 % of peak values are used. FREI ignition and extinction temperatures are extracted by using FREI downstream and upstream positions with calibration data and the temperature profile.

3.2 Results and Discussion

3.2.1 Flames Observed inside Microcombustors

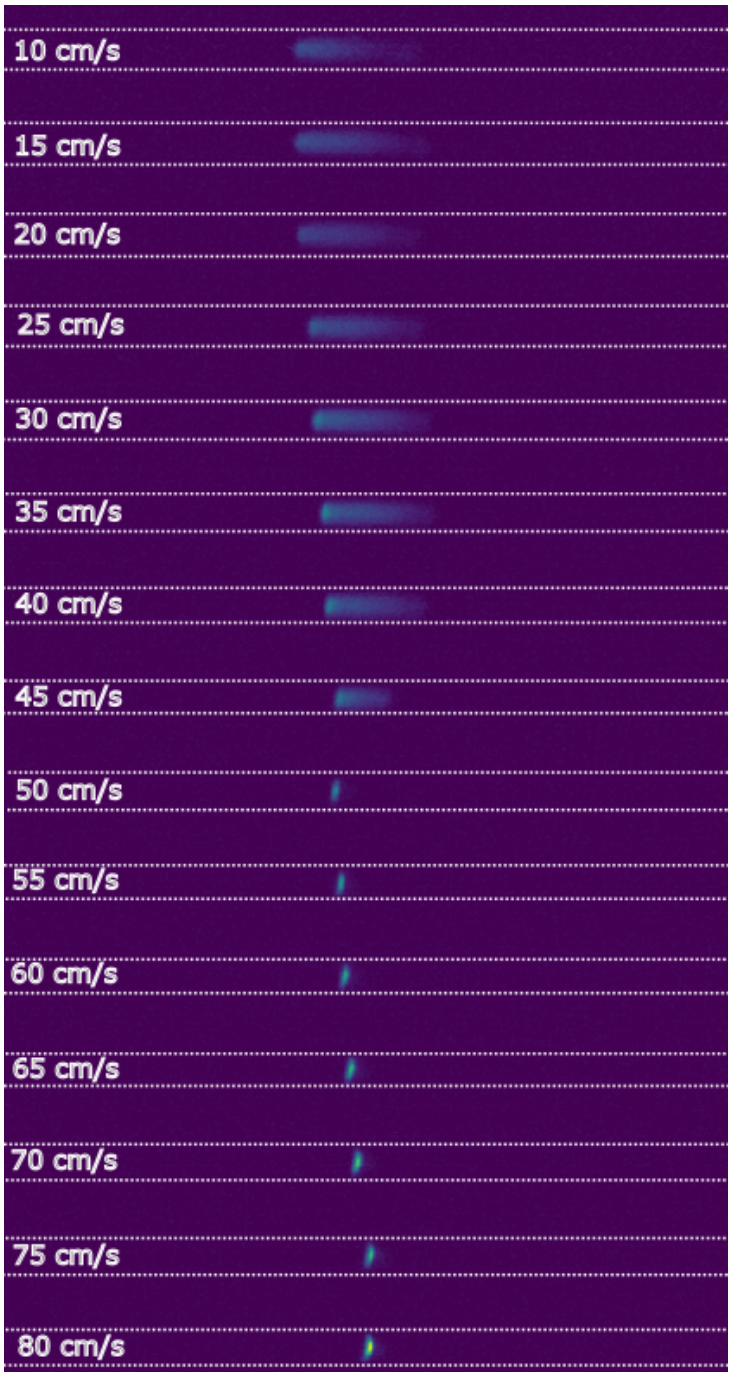

Figure 3.10: Flames images with the inlet velocity (C_3H_8/air, ϕ = 1, d = 1 mm).

Results for flame observation are reported in this section for a velocity sweep covering strong flames and FREI. Figure 3.10 displays flame images in high and moderate velocity regimes for a 1

mm inner diameter and 3 mm outer diameter microcombustor for $\phi_{\text{tube}}=1$. The unburned fuel/air mixture flows from the left side to the right side. All flame images are taken by the monochrome machine vision camera. Images shown in Figure 3.10 are preprocessed in python for noise removal and are represented in false color. The low-velocity regime (weak flame) is not shown here because

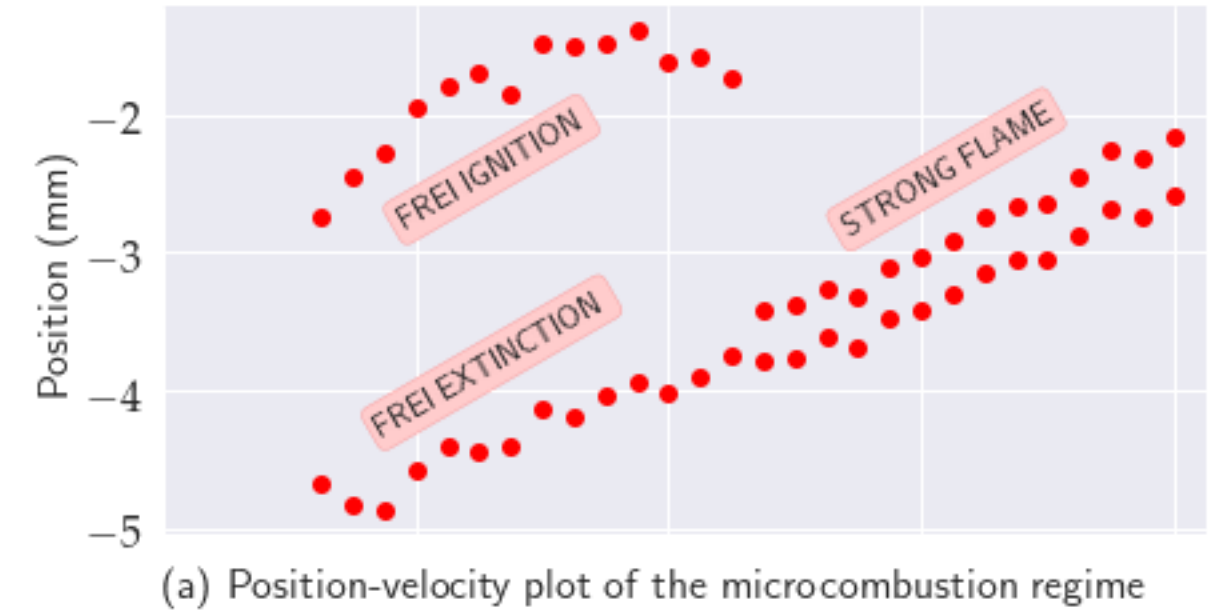

(a) Position-velocity plot of the microcombustion regime

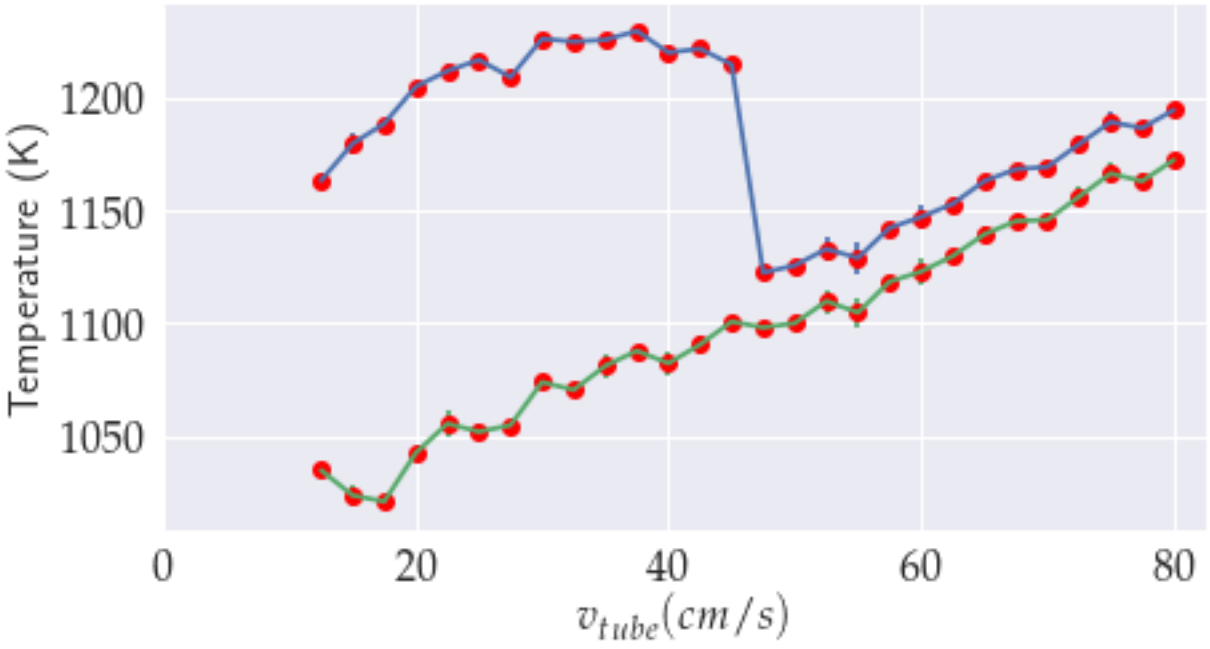

(b) Temperature-velocity plot of the microcombustion regime

Figure 3.11: Position of reaction zone and averaged mixture velocity (experimental results).

of the limitation of the machine vision camera to capture weak flame CH^* chemiluminescence appropriately. Figure 3.10 illustrates strong flames are observed for a high range of velocity. A transition occurs at an intermediate velocity and the strong flame switches to a periodic combustion instability, FREI. FREI are observed at intermediate fuel-air mixture velocity in previous studies [62, 101, 94]. FREI appear as a thick broad combustion zone with naked eyes. FREI broad regions result from oscillating combustion zones, which ignite and extinguish periodically. Both strong flame and FREI shift towards upstream as v_{tube} decreases.

3.2.2 Temperature-Velocity Plot of the Microcombustion Regime

Positions of reaction zones of strong flames and FREI with respect to v_{tube} are shown in Figure 3.11a for propane inside a 1 mm inner diameter microcombustor at ϕ_{tube}=1. The origin of the position axis in Figure 3.11a is at the center of the temperature profile as shown in Figure 3.8. Positive coordinates of the position axis indicate downstream (hot) region of the microcombustor, and negative coordinates indicate upstream (cool) region of the microcombustor. Flame positions are extracted from raw data using the methods illustrated by Figure 3.8. Strong flames are indicated by two points because of their finite length, the python algorithm is able to extract out extremities of strong flames. Downstream points indicate FREI ignition positions, and upstream points indicate FREI extinction points. It is evident from Figure 3.11a that a strong flame switches to FREI in the intermediate velocity region ($\sim$45 cm/s).

Figure 3.11b illustrates a temperature-velocity plot of FREI and strong flame regimes. The temperature-velocity plot is generated from flame positions shown in Figure 3.11a. Error bars are provided to show the standard deviations of repeated measurements. Figure 3.11b demonstrates the transition from a strong flame to FREI by a sudden change in temperature. At high v_{tube}, the strong flame stabilizes by preheating of the unburned mixture, hence it can exist at low temperatures. A strong flame shifts to a higher temperature for a high v_{tube} because increasing v_{tube} causes an ineffective heat transfer from the hot tube wall to the unburned mixture, which requires a longer distance to preheat the unburned mixture [71]. Strong flames have higher reaction rates in comparison to the adiabatic flames. Strong flames at higher v_{tube} have lower heat losses because they stabilize in

high wall temperature region. As v_{tube} decreases, the strong flame shifts towards the upstream side and heat losses from the strong flame increases. When heat losses to microcombustor wall reach a critical high point, FREI appear. In FREI, the unburned mixture ignites in a downstream (hot) region, moves to an upstream (cold) region, and eventually quench because of high heat losses to cold walls. Increase in FREI ignition and extinction temperatures with v_{tube} can be explained by an increase in mass burning flux and consequently increased reaction rates supported by higher temperatures.

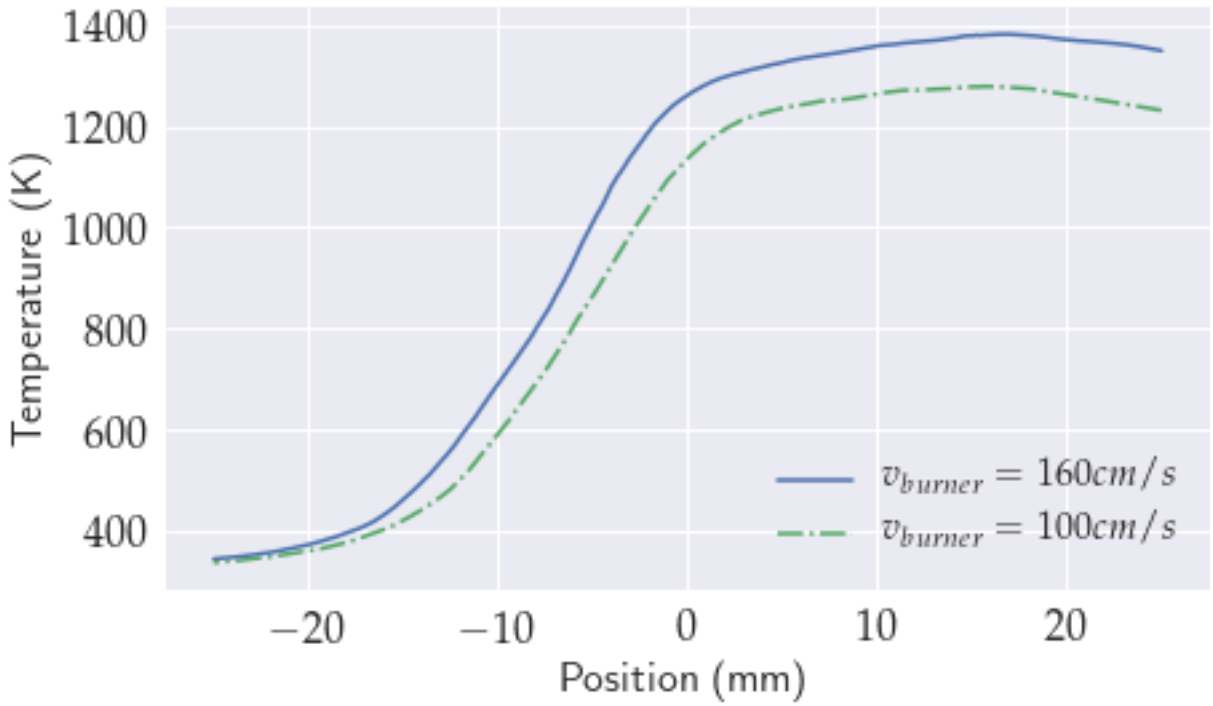

Figure 3.12: Impact of external heating: microcombustor inner wall temperature profile for v_{burner}=160 cm/s and 100 cm/s.

3.2.3 Impact of External Heating

This section discusses the impact of external temperature profile on FREI and strong flames. The external temperature profile is changed by changing the external heating rate. The external heating rate is changed by changing v_{burner}, while ϕ_{burner}=1 is kept constant. Two different external heating rates (v_{burner}=100 cm/s and 160 cm/s) are used to study the impact of external temperature profile. All other external conditions are kept the same. ϕ_{tube}=1 is kept constant in experiments and all experiments are started at the highest v_{tube}.

Figure 3.12 illustrates microcombustor inner wall temperature profiles measured for v_{burner}=100 cm/s and 160 cm/s. Reducing external heating makes the temperature profile less steep and causes reduction in its peak temperature. Peak temperature (T_{max}) of 1278.4 K and 1382.42 K are obtained for burner velocities v_{burner} of 100 cm/s and 160 cm/s, respectively. Bright, strong flames are

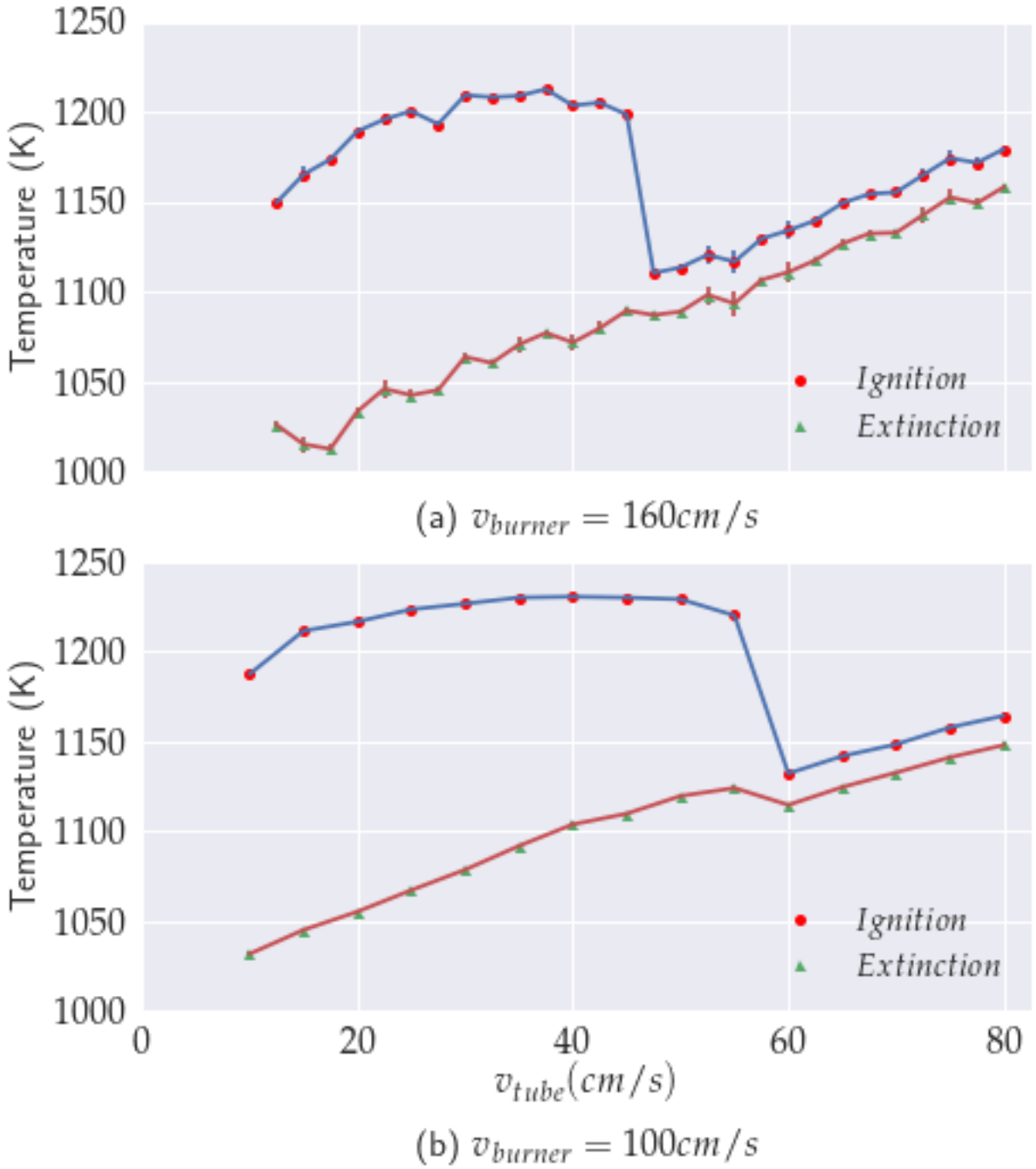

Figure 3.13: Impact of external heating on the micro-combustion regime.

observed at higher velocities. A transition to FREI occurs v_{tube}≈50-60 cm/s.

Figure 3.13 displays processed data from raw data of low-speed machine vision camera and the thermocouple. One important finding is that the transition from a strong flame to FREI happens earlier for v_{burner}=100cm/s, which is similar to Maruta et al. observations [62], who reported that a decrease of peak wall temperatures triggers a transition from strong combustion to FREI and other oscillatory behavior, which is caused by loss in stability by increase in heat losses to relatively cold walls. Figure 3.14 shows as the heating rate decreases, FREI ignition and extinction temperatures increase. As the heating rate decreases, the external temperature profile becomes less steep. A less steep temperature profile provides lesser preheating to the unburned mixture, which causes an increase in ignition temperatures. Increase in extinction temperatures are attributed to increase in flames heat losses to the relatively cold microcombustor wall for a less steep temperature profile.

Figure 3.15 indicates that higher FREI ignition and extinction temperatures match with a decrease in FREI frequencies because higher FREI ignition and extinction temperatures lie on the downstream part of the temperature profile, hence the distance between two temperatures is less, so

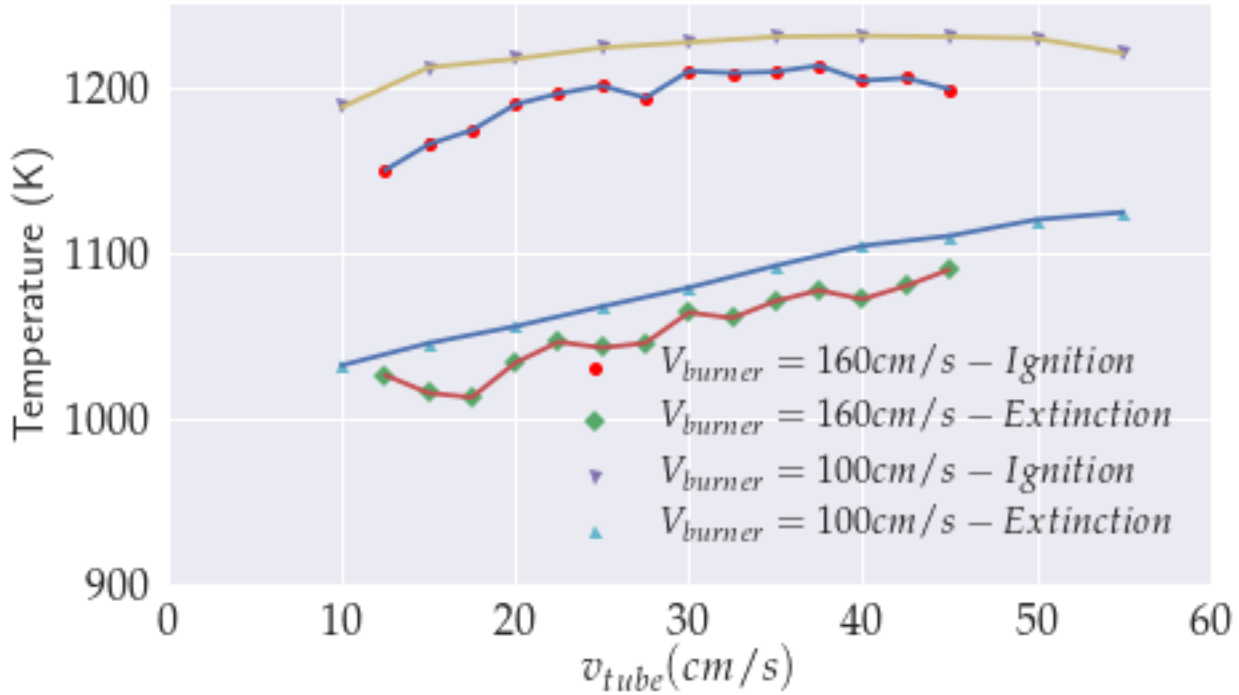

Figure 3.14: Impact of external heating on FREI ignition and extinction temperatures.

FREI have to travel a short distance for one repetition for higher FREI ignition and extinction temperatures.

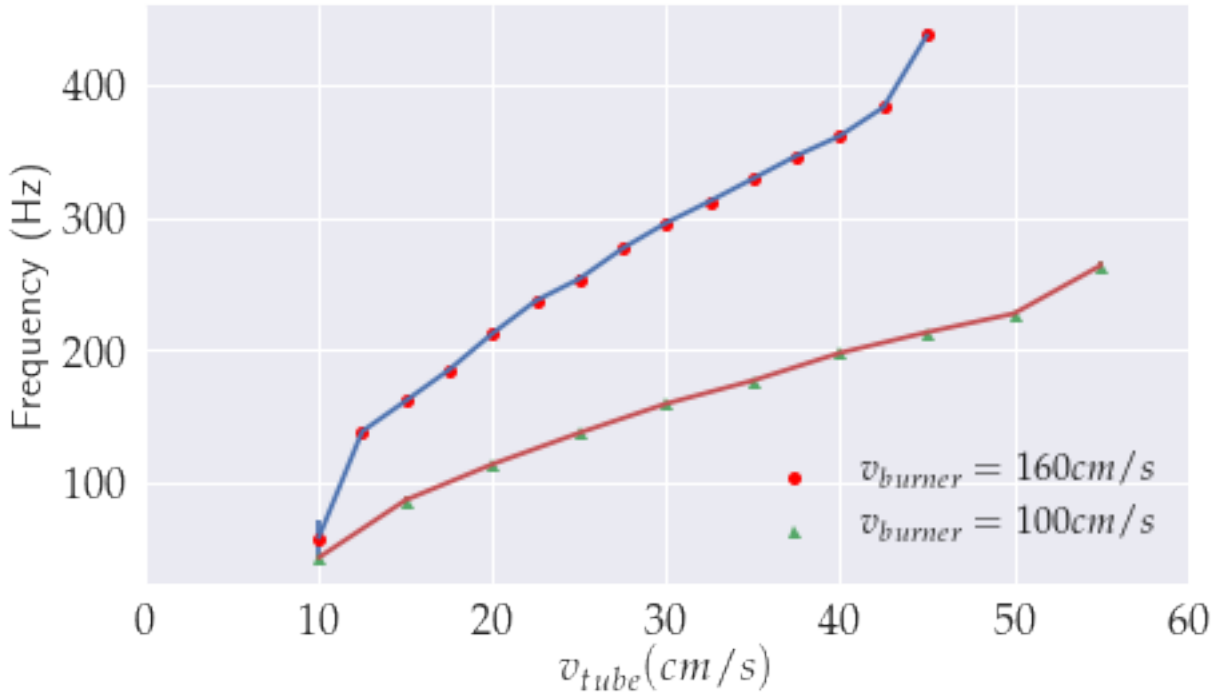

Figure 3.15: Impact of external heating on FREI frequencies.

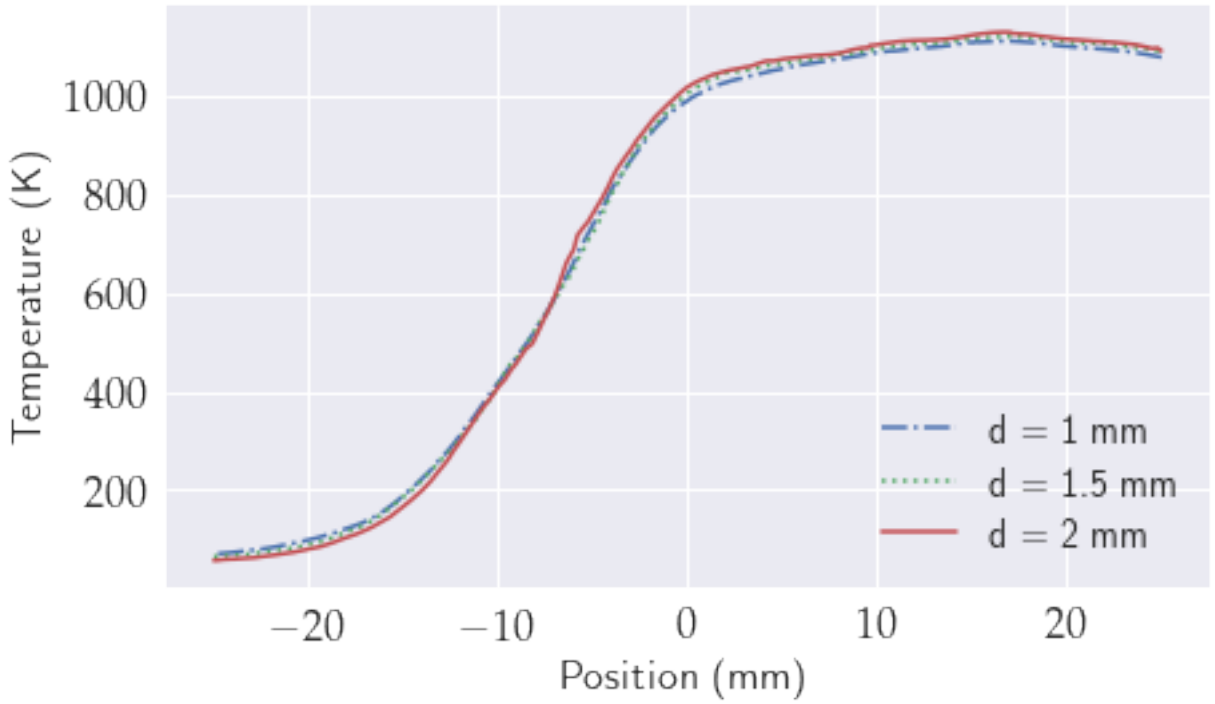

Figure 3.16: Microcombustor inner wall temperature profile for d=1mm, 1.5 mm, and 2 mm.

3.2.4 Impact of Microcombustor Diameter

Studies by Pizza et al. [85], Norton et al. [71], and Gauthier et al. [27] have shown that microcombustor inner diameter affects its microcombustion behavior, accordingly the influence of the microcombustor inner diameter on its combustion behavior has been studied in this section.

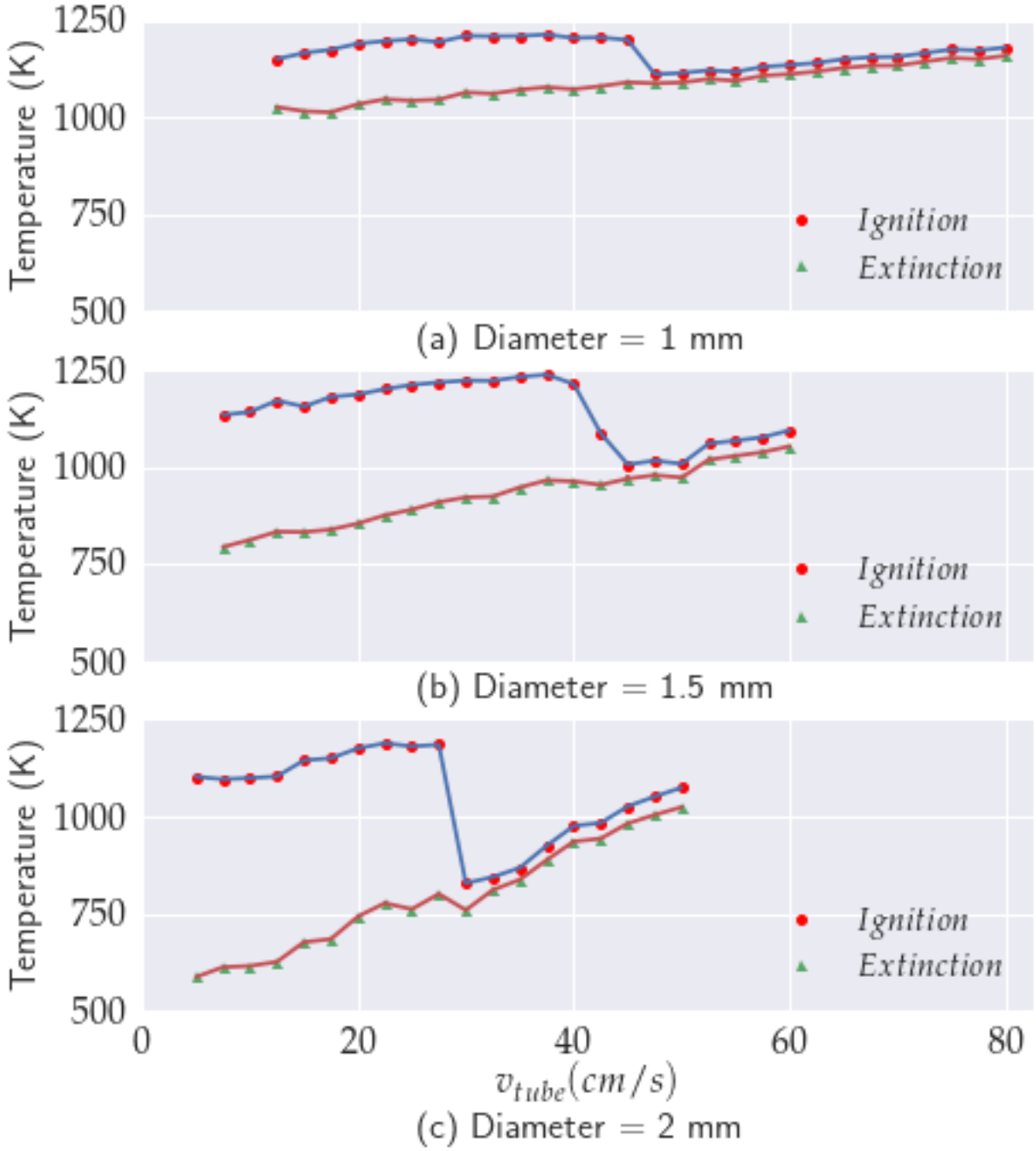

Figure 3.17: Impact of microcombustor inner diameter on the micro-combustion regime.

Three microcombustors with inner diameters of 1.0 mm, 1.5 mm, and 2.0 mm are used to understand impact of microcombustor inner diameter. All three microcombustors have a same outer diameter of 3.0 mm. All microcombustors inner diameters are smaller than the conventional quenching diameter. Figure 3.16 illustrates inner wall temperature profiles for three different microcombustors. The McKenna burner conditions are kept at v_{burner}=160 cm/s and ϕ_{burner}=1 for all experiments. Figure 3.16 illustrates that the microcombustor with an inner diameter of 1.0 mm shows the lowest peak temperature in the temperature profile, followed by 1.5 mm and 2 mm. This could be summarized as the microcombustor with thicker walls shows the lowest peak temperature in the temperature profile, which could be attributed to the axial conduction effect. For a same outer diameter, a tube with smaller inner diameter provides a larger cross-section for axial conduction in comparison of a tube with a larger inner diameter. This large available cross-section area reduces axial temperature gradient and the peak temperature in the temperature profile by increasing axial heat transfer across the tube cross-section.

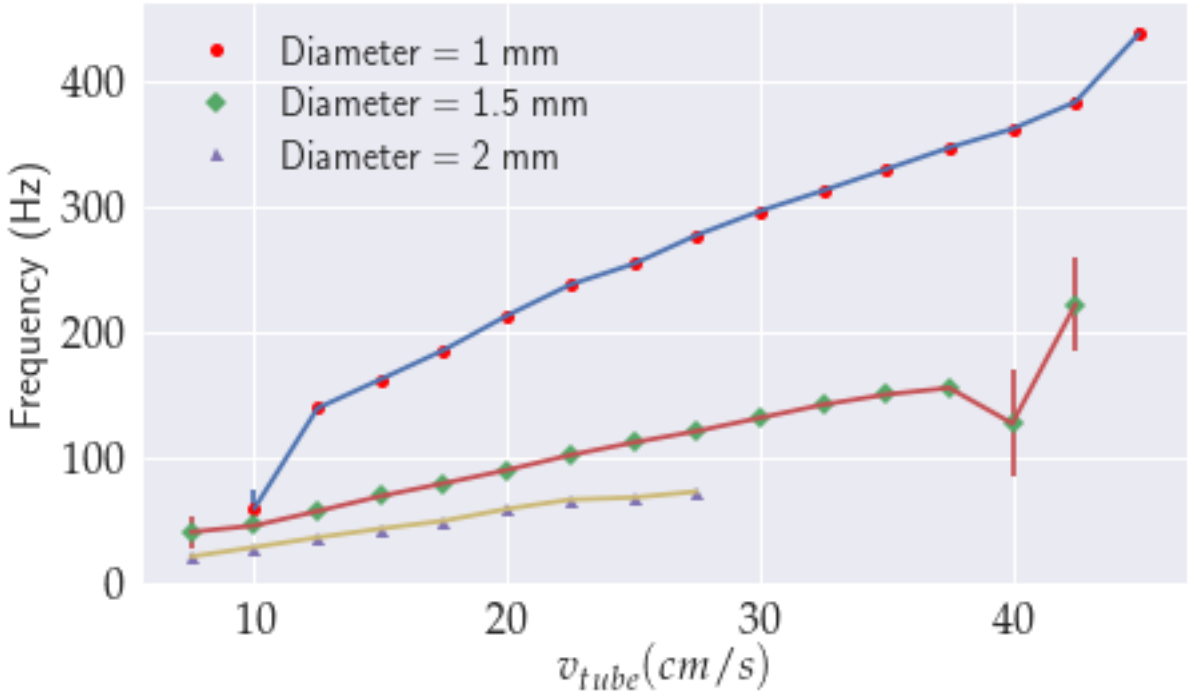

Figure 3.18: Impact of microcombustor inner diameter on FREI frequencies.

Propane fuel is used for microcombustor inner diameter experiments. ϕ_{tube}=1 is kept same for all experiments. Figure 3.17 shows stabilizing temperatures of strong flames and ignition and

extinction temperatures of FREI with respect to v_{tube}. One important finding is that reducing the microcombustor inner diameter results in change in strong flame-FREI regime transition. For 1mm, the transition happens at v_{tube} ∼47.5 cm/s, for 1.5 mm at v_{tube} ∼42.5 cm/s, and for 2 mm at v_{tube} ∼30 cm/s. A similar shift in strong flame-FREI regime transition is reported by Pizza et al. [85] and Bianco et al. [10]. The impact of an increase in inner diameter is more pronounced on FREI extinction temperatures and strong flame stabilization temperatures. Strong flames are found to be stabilized at higher wall temperature for smaller inner diameter tubes. As the microcombustor inner diameter decreases, the flame surface-to-volume ratio increases, and heat losses from the flame to microcombustor wall increases, so the strong flame stabilization point moves to a higher temperature to compensate for heat losses. As the microcombustor inner diameter increases, FREI extinguish at lower temperatures because heat losses from the flame kernel decrease as the surface-to-volume ratio decreases with an increase in the inner diameter.

FREI frequencies for different inner diameter microcombustors are illustrated in Figure 3.18. Large differences in FREI ignition and extinction temperatures show lower frequencies because flames have to move large distances for one repetition. Results for 2 mm inner diameter tube show lowest frequencies due to large temperature differences in FREI ignition and extinction temperatures.

3.2.5 Impact of Fuel

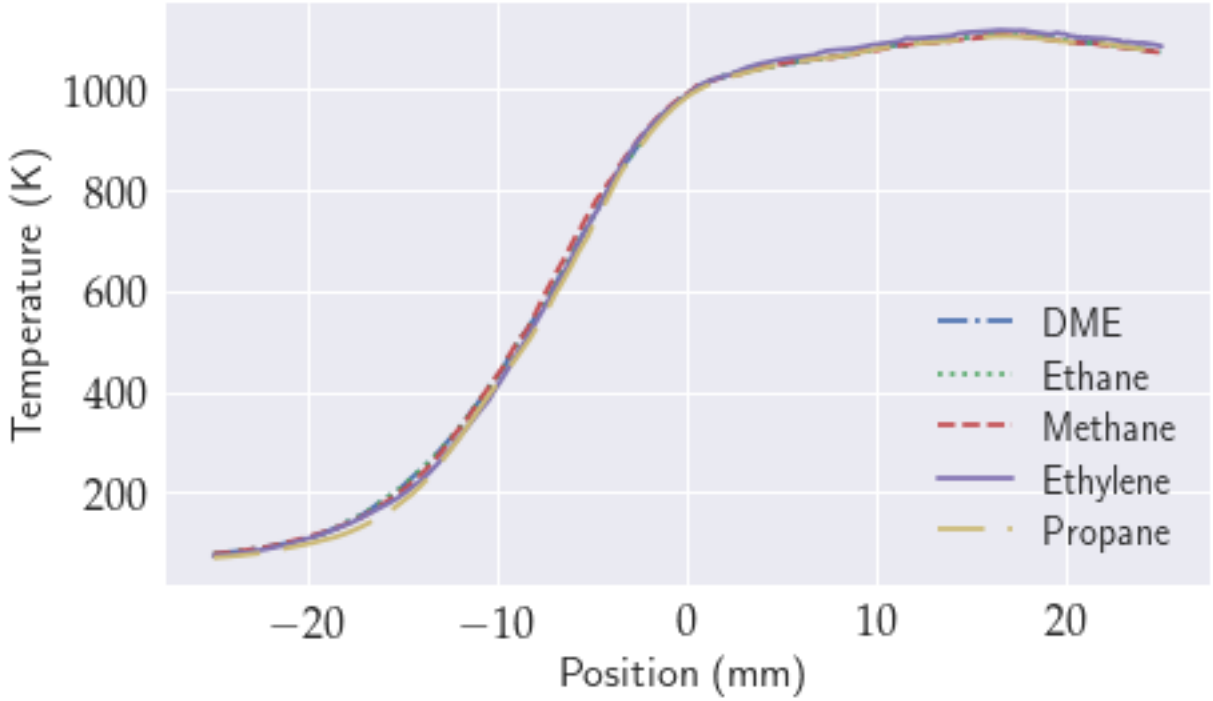

Figure 3.19: Impact of fuel: microcombustor inner wall temperature profile for DME, ethane, methane, ethylene, propane.

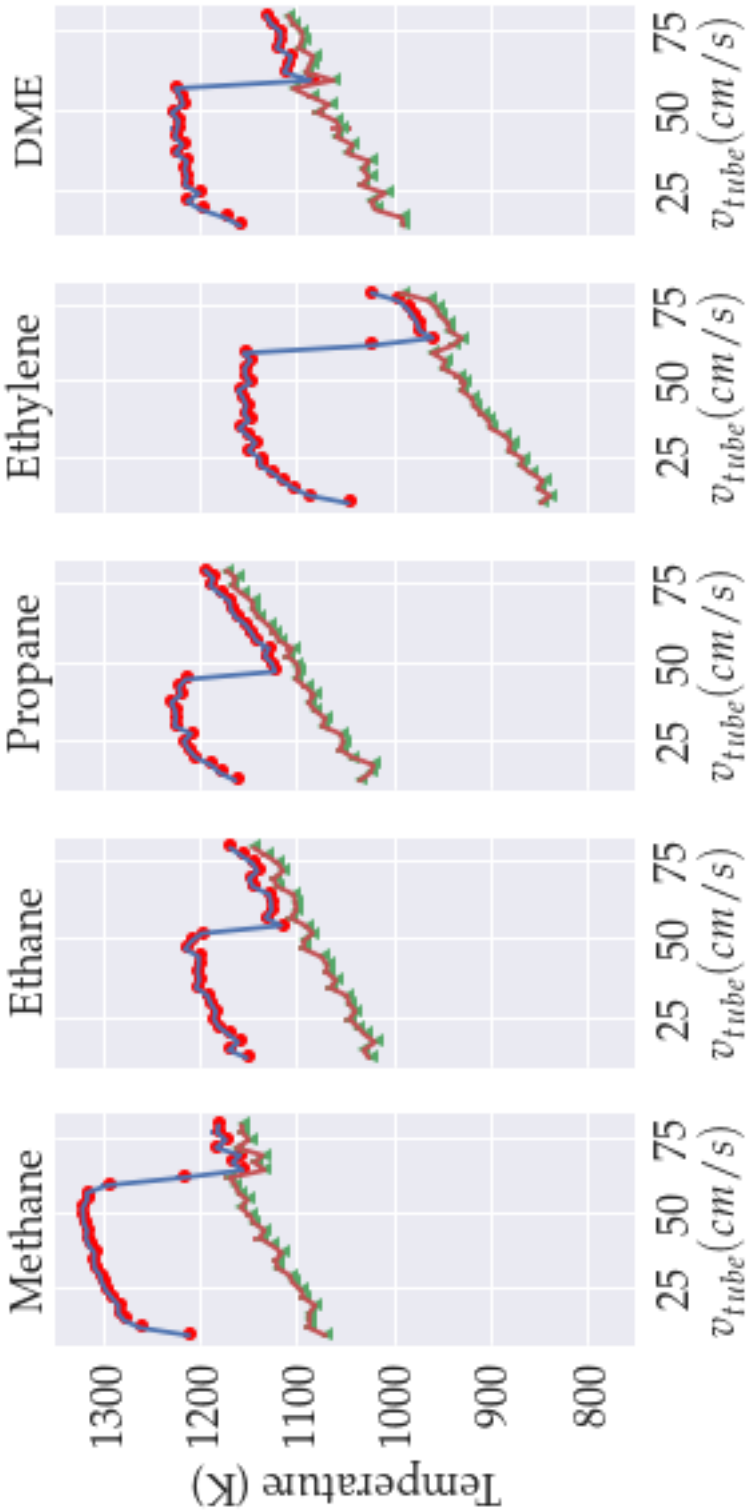

Figure 3.20: Impact of fuel on the micro-combustion regime.

This particular section aims to understand the impact of gaseous fuel on FREI and strong flames.

Figure 3.19 illustrates microcombustor inner wall temperature profiles for five different gaseous

fuels. McKenna burner conditions are kept at v_{burner}=160 cm/s and ϕ_{burner}=0.6 for all experiments. Five gaseous fuels- methane, ethane, propane, ethylene, and dimethylether (DME) are tested. Methane, ethane, and propane are high octane number fuels and give comparisons to transportation fuels. Ethylene is added to study the impact of the double bond in the carbon chain length. DME is considered to investigate the impact of the addition of oxygen atom to carbon chain length. DME is an alternative fuel for diesel engines with a high Cetane Number.

Figures 3.20 illustrates results for five gaseous fuels, which are tested under otherwise identical conditions. To compare alkanes - methane, ethane, and propane, carbon number of the hydrocarbon chain from C_1 to C_3 is taken as the criterion. Figure 3.20 reveals that as we add one C-C bond in the methane, the micro-combustion behavior changes, but adding a further C-C bond does not change the micro-combustion behavior significantly, which indicates a small impact of increasing the carbon chain length. By comparing results for ethane and ethylene, Figure 3.20 shows that the presence of a carbon-carbon double bond changes the micro-combustion behavior significantly.

A comparison of results for different fuels shows significant differences in both FREI Ignition and extinction temperatures, which indicate that FREI behavior is impacted by fuel chemistry. In FREI ignition temperatures, methane shows the highest levels (1320 K), followed by DME (1230 K), propane (1225 K), ethane (1210 K), and ethylene with the lowest level (1160 K); Kamada et al. [49] shows the same order of temperature for weak flames. Differences in extinction temperatures for different fuels are more pronounced, where decrease in extinction temperature indicates increase resistance to quenching. Again, methane exhibits the highest levels. Extinction characteristics of ethane and propane are comparable, whereas a drop is seen for DME. Ethylene exhibits the lowest extinction temperatures correspond to an increased resistance to quenching.

In addition to FREI results, microcombustor results also give insight in fuels non-adiabatic flame speeds at stationary conditions. To compare non-adiabatic flame speeds for fuels, preheating levels of laminar stable flames adjust to tube flow velocities v_{tube}. As an example, for a stable flame at v_{tube} = 80 cm/s, fuels fall in the order CH4 > C2H6 > C3H8 > DME > C2H4 in terms of preheating. Adiabatic flame speeds S_L increase as preheating increases, so the order of S_L will reverse of the

preheating order. The order of S_L will CH4 < C2H6 < C3H8 < DME < C2H4, which agrees with published data [28]. However, a conclusive link to S_L requires a computational framework that accounts for preheating and non-adiabatic conditions.

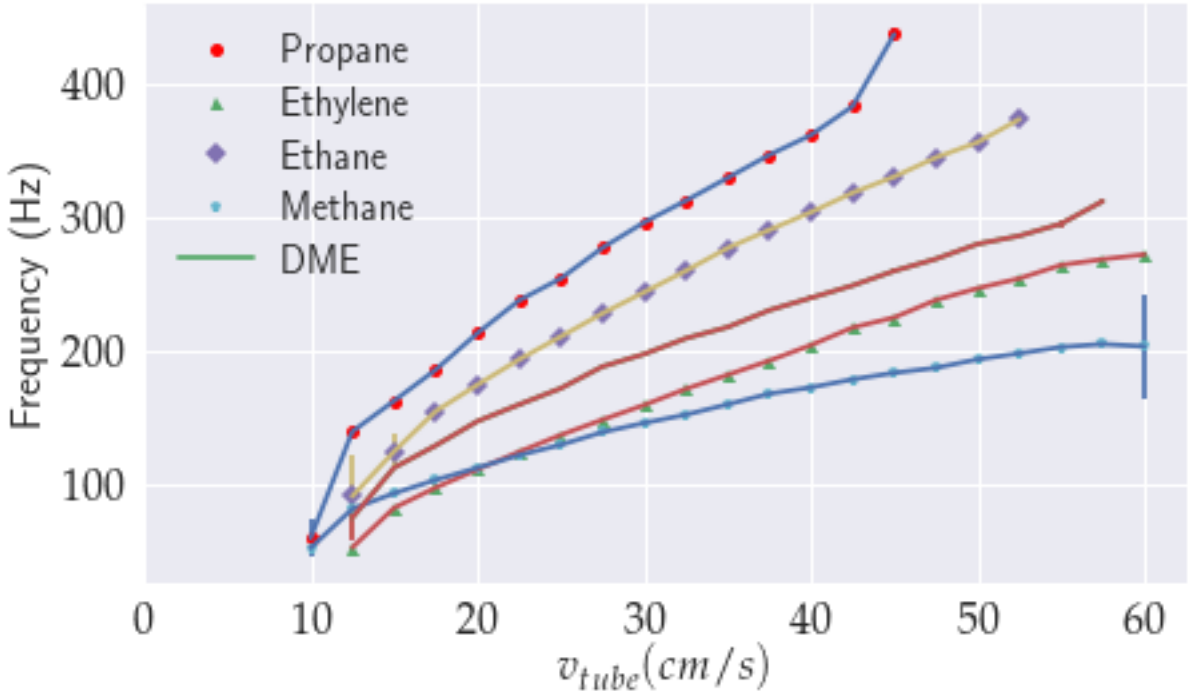

Figure 3.21: Impact of fuel on FREI frequencies.

Figure 3.21 illustrates FREI frequencies for DME, ethane, methane, propane, and ethylene. Here lowest FREI frequencies are observed for fuel with larger differences in ignition and extinction temperatures. Here, methane is an exception, as reduced frequencies are due to FREI form farther downstream, where temperature gradients are smaller.

3.2.6 Impact of Equivalence Ratio

Table 3.2: Equivalence ratios (ϕ) and corresponding normalized equivalence ratios (Φ).

ϕ	0.61	0.72	0.85	1.00	1.17	1.38	1.63
Φ	0.378881988	0.418604651	0.459459459	0.5	0.539170507	0.579831933	0.619771863

The objective of this section is to understand the influence of equivalence ratio (ϕ_{tube}) on FREI and strong flames inside the microcombustor. Seven equidistant normalized equivalence ratios ($\Phi=\phi/(\phi+1)$) are used to sample both lean and rich regimes. Table 3.2 displays equivalence ratios

(ϕ_{tube}) and corresponding normalized equivalence ratios (Φ_{tube}). A 1 mm inner diameter and 3 mm outer diameter quartz tube microcombustor is used with propane fuel. Figure 3.22 illustrates raw

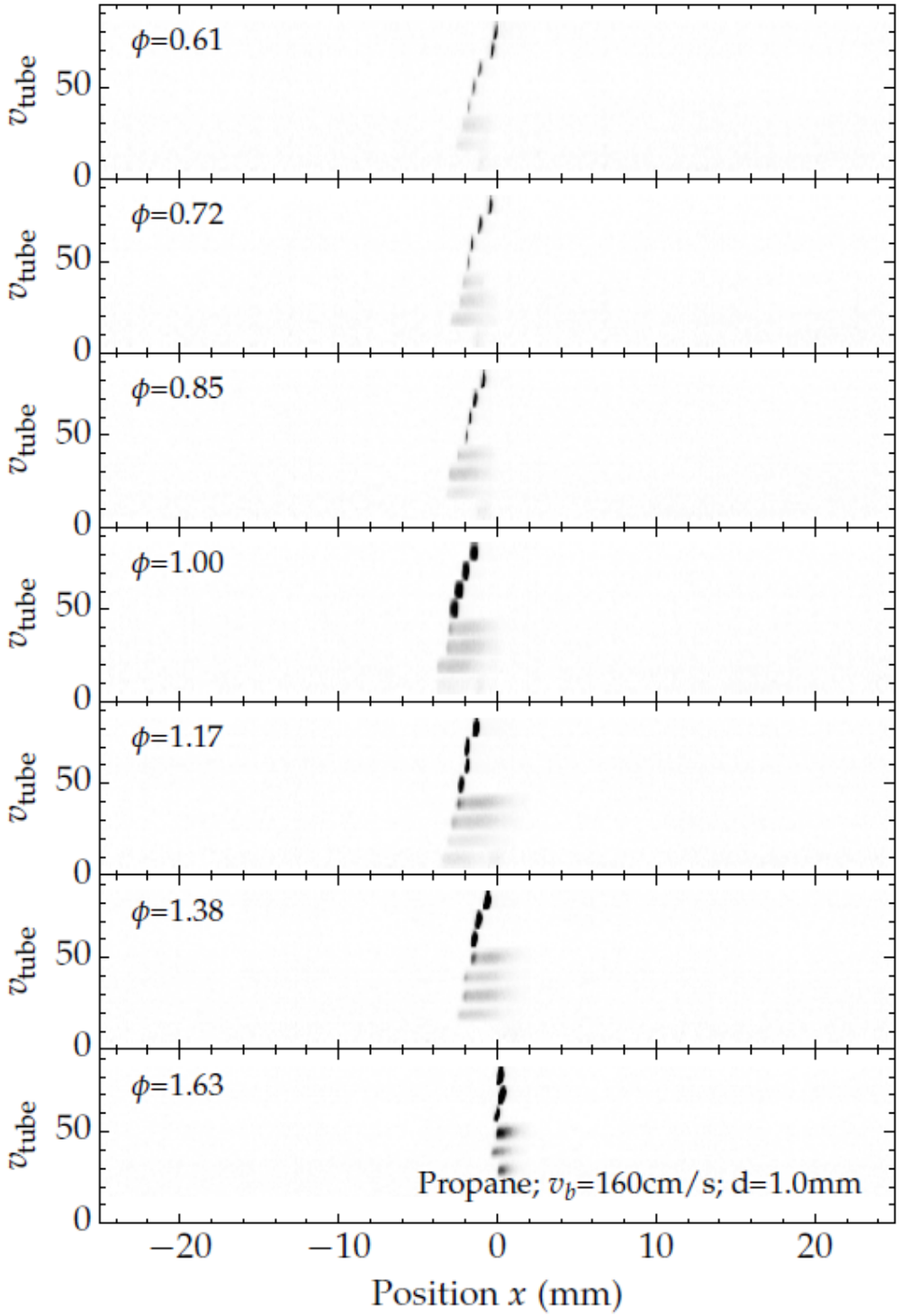

Figure 3.22: Impact of equivalence ratio on flame positions. (Credit: I. Schoegl)

data for propane for various equivalence ratios (ϕ_{tube}), where flame locations (greyscale composite images) are presented. Figure 3.22 depicts only FREI and strong flames. In all cases, experiments are started at the highest v_{tube}, where strong flames are observed. As v_{tube} decreases, a transition to FREI occurs at v_{tube} ~50 cm/s, which are easily recognized as elongated flames in low-speed imaging.

Increase in the strong flame brightness with increasing the ϕ_{tube} is attributed to an increase in fuel mass fraction with an increase in ϕ_{tube}. For all ϕ_{tube}, strong flames stabilize at lower wall temperatures by decreasing v_{tube}. Strong flames are observed to stabilize at the lowest wall temperatures for ϕ_{tube}=1, and strong flames stabilization temperatures are found to increase by both increasing and decreasing ϕ_{tube} either side of ϕ_{tube}=1. This observation is in agreement with Stazio et al. [94], who also observed the lowest stabilization temperatures for ϕ_{tube}=1, and highest for richest and leanest fuel-air mixtures. In the previous section, it has shown that a fuel with highest laminar flame speed needs lowest preheatings to stabilize strong flames inside the microcombustor. The same logic can also be used for ϕ_{tube} results to understand the impact of equivalence ratio on non-adiabatic laminar flame speed. The ϕ_{tube}=1 case needs lowest preheating and preheating increases either side of ϕ_{tube}=1, which indicates that ϕ_{tube}=1 mixture has the highest laminar flame speed, and the laminar flame speed decreases either side of ϕ_{tube}=1. These results are in a direct correlation with corresponding adiabatic results, where the highest laminar flame speed is found for a slightly fuel-air rich mixture. [28]. FREI positions shift downstream on either side of ϕ_{tube}=1, which is equivalent to FREI ignition and extinction temperatures increase on either side of ϕ_{tube}=1.

3.3 Summary

An experimental setup is designed to investigate FREI and strong flames in an externally heated microcombustor. The microcombustor consists of a cylindrical quartz tube. This quartz tube is heated externally by a flat flame McKenna burner. This heating system ensures a stationary temperature profile starting from ~350K on the upstream side (gas inlet) to a maximum of ~1400K downstream. H_2/air mixture is used for the the McKenna burner to keep the external McKenna flame

free of CH^* species, which allows a better visualization of CH^* chemiluminescence of flames inside the microcombustor. The temperature distribution along the inner side of the microcombustor wall is measured by a K-type thermocouple. A monochrome machine vision camera is used to image various flames inside the microcombustor. Raw experimental data are processed using Python.

All experiments are conducted at atmospheric pressure. The specific approach of this study converts locations of FREI ignition and extinction points to local wall temperatures, which are subsequently used to quantify FREI ignition and extinction temperatures, respectively. Three different flame behaviors are observed: strong flames at higher v_{tube}, FREI at intermediate v_{tube}, and weak flames at marginal v_{tube}. Weak flames are not shown and discussed further in the chapter. The respective impact of external heating, microcombustor inner diameter, ϕ_{tube}, and fuel are investigated.

FREI and strong flames investigated in this study are shown to depend on fuel behavior. Differences in microcombustion behavior are attributed to fuel chemistry. Results for FREI ignition temperatures of different gaseous fuels reveals similar trends as those has been reported in earlier weak flame studies [49]. Further, trends of non-adiabatic flames observed at high tube velocities correlate to adiabatic flame speed data. The small amount of fuel required for microcombustor experiments shows its potential for accelerated research on traditional and bio-derived fuels. As auto-ignition and flame speed metrics are relevant to IC engine operation, there is a strong indication that the experimental framework can be extended with an objective to quantify the impact of bio-fuels on IC engine performance.

Chapter 4
FREI Behavior at Engine Relevant Presssures

Microcombustor experiments in the previous chapter are conducted at atmospheric pressure. Understanding micro-scale combustion behavior at elevated pressure is necessary to make microcombustor results applicable to engine conditions. This chapter investigates the impact of pressure on FREI behavior using transient numerical simulations with detailed chemistry. This chapter firstly discusses OpenFOAM software/laminarSMOKE solver description. After that geometry of computational domain and computational cases are described. The chapter concludes with numerical cases results and final remarks.

4.1 OpenFOAM and LaminarSMOKE Solver

The Open Source Field Operation and Manipulation (OpenFOAM) is used in this work to perform numerical simulations [79]. The laminarSMOKE solver is used to resolve the detailed chemistry of laminar reacting flows [16, 17]. The CRECK group in Milan, Italy has developed the laminarSMOKE solver and validated for moderately large reaction mechanisms with up to $\sim$220 species and $\sim$6800 reactions [16, 17]. The laminarSMOKE solver is built on top of open-source CFD package OpenFOAM. The laminarSMOKE solver code is derived from the standard pisoFoam solver of OpenFOAM. The pisoFoam solver has a capability of solving unsteady, compressible, non-reacting flows. To include simulation of reacting flows with detailed chemistry, the pisoFoam solver is modified by adding the operator-splitting approach. A kinetic interpreter is used to preprocess kinetic mechanism for simulations. The kinetic interpreter takes kinetic mechanisms in CHEMKIN format and outputs mechanisms in Cantera format.

4.2 Governing Equations

The laminarSMOKE solver solves continuity, momentum, species, and energy equations (Equations 4.1, 4.2, 4.3, 4.4) for the reactive laminar regime and a Newtonian fluid. All equations are defined for a compressible, multi-component, and thermally-perfect gas mixture.

$$\frac{\partial \rho}{\partial t} + \nabla(\rho v) = 0 \tag{4.1}$$

$$\frac{\partial}{\partial t}(\rho v) + \nabla(\rho vv + pI) = \nabla(\tau) + \rho g \tag{4.2}$$

ρ is the mixture density, t is the time, v is the velocity vector of mixture, p is the pressure,τ is the fluid stress tensor, and g is the gravity acceleration vector.

$$\frac{\partial}{\partial t}(\rho \omega_k) + \nabla(\rho \omega_k v) = -\nabla(\rho \omega_k V_k) + \Omega_k \quad k = 1, ..., NC \tag{4.3}$$

ω_k is the species mass fraction, V_k is the k^{th} species diffusion velocity, and Ω_k is the species formation rate.

$$(\rho C_p)\frac{\partial T}{\partial t} + \rho C_p v \nabla T = -\nabla q + \rho \sum_{k=1}^{NC} C_{pk} \omega_k V_k - \sum_{k=1}^{NC} h_k \Omega_k \tag{4.4}$$

C_p is the mixture constant pressure specific heat, T is the temperature, C_{pk} is the constant pressure specific heat of individual species k, q is the heat flux vector, h_k is the enthalpy of individual species, and NC represents the total number of species in the gas mixture.

Heat transfer by conduction and radiation are considered in the heat flux vector (q) calculation through Equation 4.5.

$$q = \lambda \nabla T + q_{rad} \tag{4.5}$$

λ represents the gas mixture conductivity and q_{rad} is the radiative heat transfer contribution towards the heat flux vector. The density of the mixture is calculated by using the ideal gas equation.

The diffusion velocity of species k is calculated by considering both the Fick's law and thermal diffusion in Equation 4.6. Γ_k stands for the individual species mixture averaged diffusion coefficient, Θ_k is the thermal diffusion ratio of species k, and X_k is the mole fraction.

$$V_k = \frac{\Gamma_k}{\omega_k}\nabla \omega_k + \frac{\Gamma_k \Theta_k}{X_k}\frac{1}{T}\nabla T \tag{4.6}$$

The corrected diffusion velocity vector V_k^c is calculated by Equation 4.7, where V_c is a constant correction factor to satisfy mass conservation.

$$V_k^c = V_k + V_c \tag{4.7}$$

V_c is calculated by Equation 4.8.

$$V_c = -\sum_{k=1}^{NC} \omega_k V_k \tag{4.8}$$

The radiative heat transfer is evaluated by using an optically thin radiation model. The self-absorption of radiation is neglected in the optically thin radiation model. Only radiations from H_2O, CO, CO_2, and CH_4 are considered. The expression for the divergence of radiative flux is given by Equation 4.9.

$$\nabla q_{rad} = -4\sigma a_p (T^4 - T_{env}^4) \tag{4.9}$$

a_p is the Planck mean absorption coefficient, σ is the Stefan-Boltzmann constant, and T_{env} is the temperature of the environment.

The planck mean absorption coefficient a_p is calculated by Equation 4.10, where p_k is the partial pressure of species k and a_{pk} comes from the RADCAL software [33].

$$a_p = p_{H_2O} a_{p,H_2O} + p_{CO_2} a_{p,CO_2} + p_{CO} a_{p,CO} + p_{CH_4} a_{p,CH_4} \tag{4.10}$$

4.3 Geometry of Computational Domain

A cylindrical tube geometry of length L=50mm and diameter D=1mm as shown in Figure 4.1 has been used in numerical simulations. The cylindrical tube is simulated based on the 2D axisymmetric wedge geometry shown in Figure 4.2 and Figure 4.3. Hydrodynamic and chemical phenomena are approximated as axisymmetric because the diameter of the circular tube is narrow enough

in comparison of its length [86], which results in circumferential gradients being much smaller than axial gradients. The 2D axisymmetric domain has been drawn along the center line of the cylindrical microcombustor. A uniform grid has been used across the two-dimensional geometry. Figure 4.1 illustrates an experimental temperature profile that has been employed along the wall of the computational domain. The velocity profile is assumed to be fully developed at the inlet of the geometry and no-slip boundary conditions have been applied on the cylinder geometry walls. Velocity-derived and pressure-derived OpenFOAM boundary conditions for the 2D axisymmetric computational domain are summarized in Table 4.1.

4.4 Cases

A total of four 2D transient cases are investigated. Cases details are summarized in Table 4.2. All cases are investigated for otherwise identical conditions, i.e., burning mass flux, stoichiometric fuel/air ratio, and externally employed experimental temperature profile. At the inlet, the wall

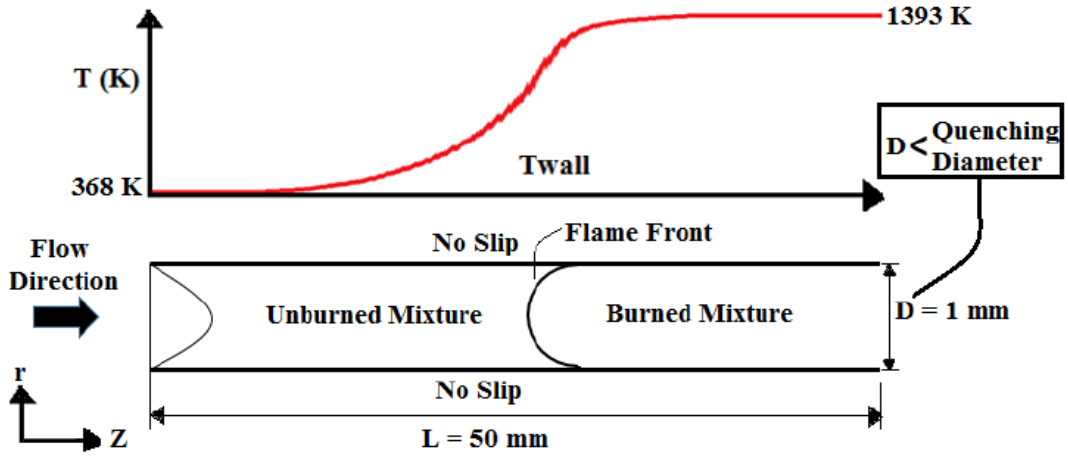

Figure 4.1: 1mm tubular microchannel with an externally imposed temperature profile.

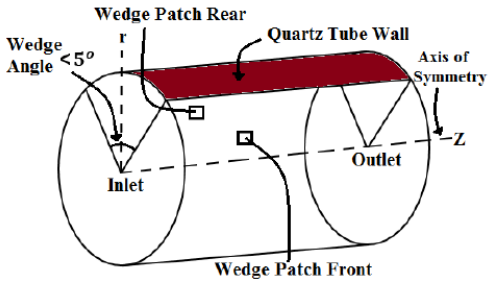

Figure 4.2: 2D axisymmetric geometry.

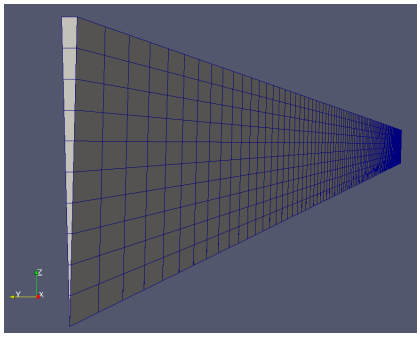

Figure 4.3: Computational mesh with wedge geometry.

temperature is 368K and at the outlet temperature is 1393K. The burning mass flux is kept constant by reducing the velocity to compensate for increased density at elevated pressures. All simulations are started with the whole computational domain is filled with air. The stoichiometric propane/air mixture enters the channel with a uniform inlet temperature ($T_{in} = 300K$) and a fully developed velocity profile with mean velocity u_{in}. A grid resolution of 10×525 is used for pressures of 1atm, 2atm, and 5atm, i.e. 10 grid points in the radial direction and 525 grid points in the axial direction. Since the flame thickness decreases with increasing pressure, the grid resolution is increased to 10×1025 for the 10atm case to better resolve the flame thickness. Data are saved every 500 μs, and simulations are continued until two ignition-extinction cycles are observed.

A standard Gaussian finite volume integration scheme is used with a second-order scheme for terms including gradients and Laplacians and first-order upwind for terms including divergence. A first-order implicit Euler scheme is used for the time integration. Parallel computing is utilized to solve the computational domain. The computational domain is divided into 64 equal size blocks and solved on 64 processors (4 nodes and 16 processors on each node). The San Diego mechanism with 53 species and 235 reactions is used to model the chemistry in this work [15].

Table 4.1: OpenFoam boundary conditions.

Boundary	Type	Velocity-Derived Type/Value	Pressure-Derived Type/Value
Inlet	Patch	Fixed Value(Fully Developed Flow)	Zero Gradient
Outlet	Patch	Zero Gradient	Fixed Value(Atmospheric Pressure)
Wall	Wall	Fixed Value/Uniform (No Slip)	Zero Gradient
Axi-Symmetric-Front	Wedge	Wedge	Wedge
Axi-Symmetric-Rear	Wedge	Wedge	Wedge

Table 4.2: Simulation parameters.

Pressure (atm)	u_{in} (cm/s)	T_{in}(K)	Diameter (mm)	ϕ	Grid
1	30	298	1	1	10×525
2	15	298	1	1	10×525
5	6	298	1	1	10×525
10	3	298	1	1	10×1025

4.5 Results

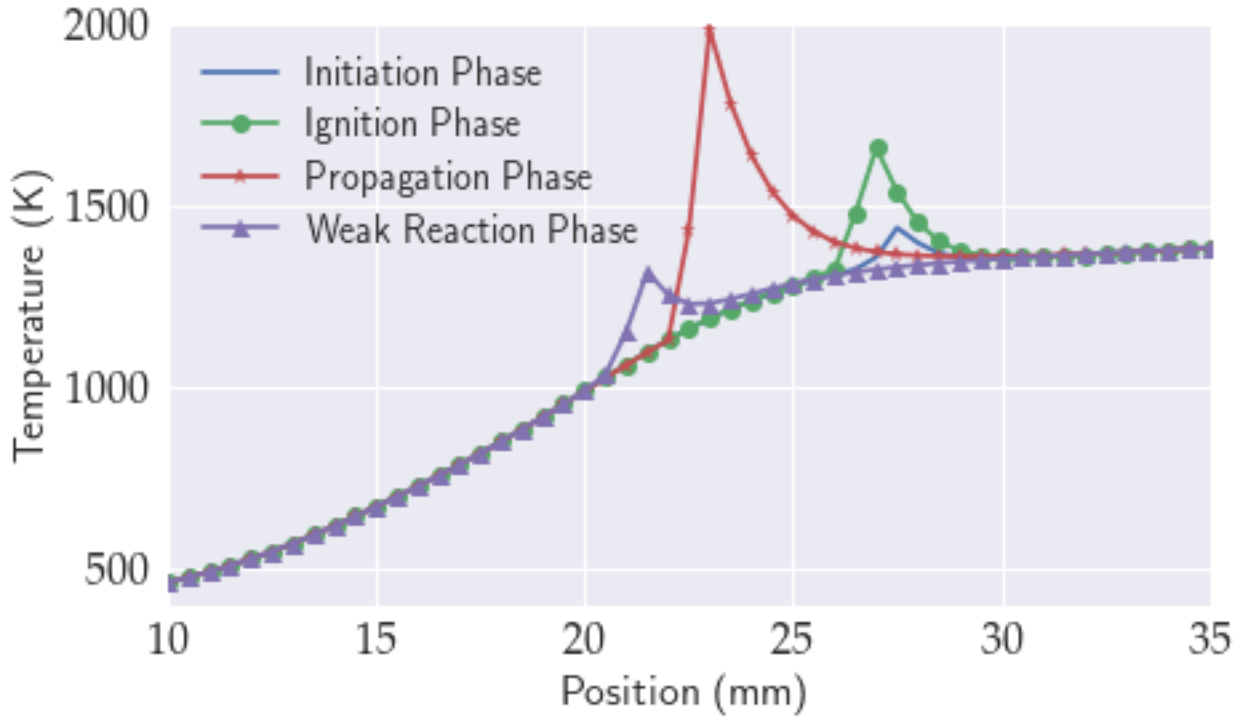

Figure 4.4: Temperature profile along the axis at various time instances during FREI cycle for 1 atmospheric case.

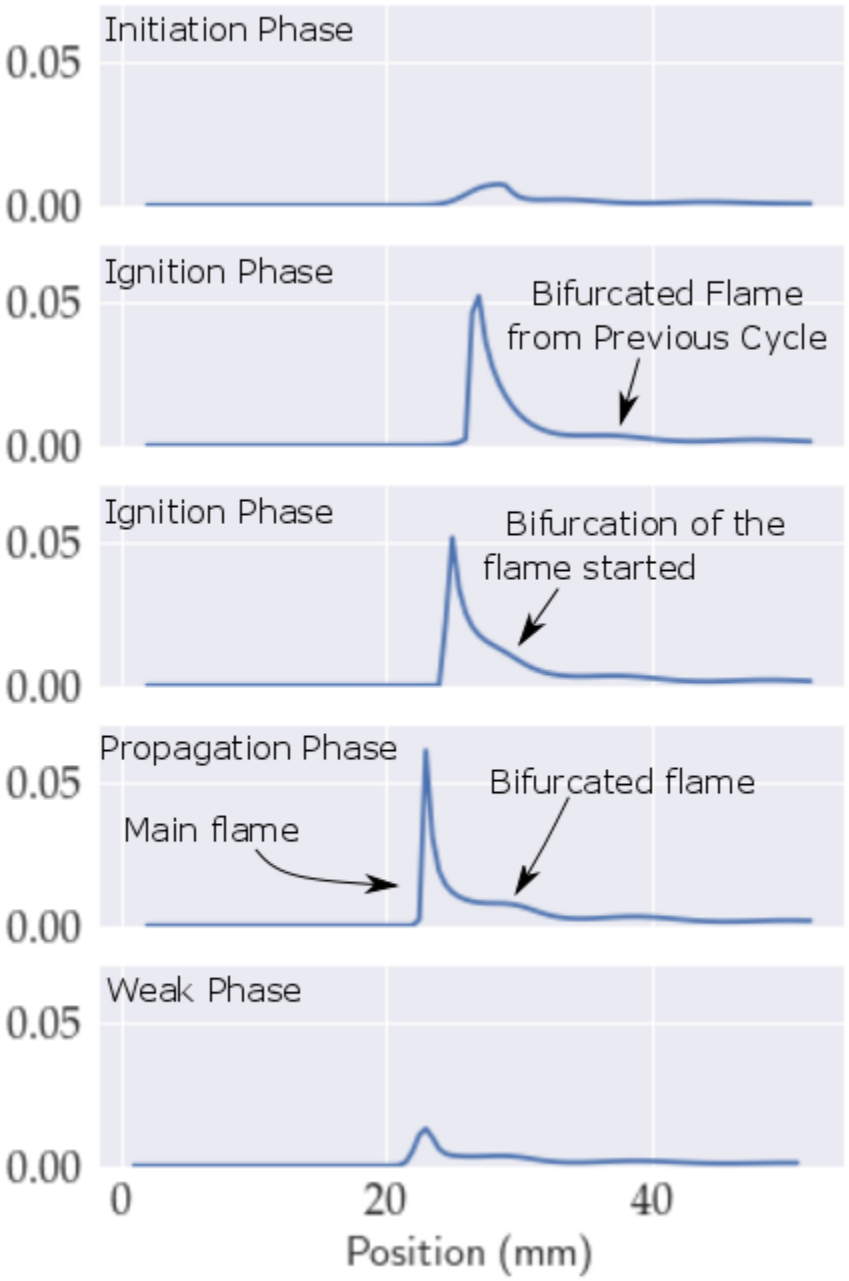

Figure 4.5: CO mole fraction along the tube axis at various time instances during a FREI cycle for 1 atmospheric case.

Figure 4.4 and 4.5 show temperature profiles and CO mole fraction profiles along the tube axis, respectively at different time instances during a FREI cycle for the 1 atmospheric pressure case. Similar to the Nakamura et al. [68] numerical study, the complete FREI propagation cycle is divided into 5 phases: (1) Initiation Phase (2) Ignition Phase (3) Propagation Phase (4) Weak Reaction Phase (5) Flowing Phase. Below all five different phases of FREI cycle are discussed.

1. Initiation Phase: During the initiation phase, a small peak in the temperature profile is observed as shown in Figure 4.4. The small peak in the temperature profile results from heat release from the reaction zone. Since there is no significant consumption of C_3H_8 in the initiation phase, the peak for CO mole fraction is very small as shown in Figure 4.5.

2. Ignition Phase: After the initiation phase, the fuel and air mixture reacts quickly in the ignition phase causing the ignition. This ignition causes large peaks in temperature and CO mole fraction profiles as shown in Figures 4.4 and 4.5. These peaks occur at a downstream location corresponding to the ignition point of FREI. Shortly after ignition, the flame bifurcation phenomenon begins, where the CO mole fraction peak breaks into two peaks, where the upstream peak is much more prominent than the downstream peak. These peaks confirm with the splitting flame dynamics observed in previous numerical and analytical studies [85, 19, 86, 68].

3. Propagation Phase: In the propagation phase, fuel and air mixture keeps reacting and the flame move towards downstream. In the propagation phase, consumption of fuel is higher in comparison to the ignition phase hence the CO mole fraction peak is bigger in the propagation phase in comparison to the ignition phase. The upstream bifurcated flame keeps moving towards the upstream consuming the unburned mixture, while the downstream bifurcated flame keeps moving towards the downstream.

4. Weak Reaction Phase: The upstream bifurcated flame continuously keeps losing heat as it moves to the upstream side. The peak flame temperature reduces as the upstream bifurcated flame reaches upstream, and the weak reaction phase starts. Due to a significant reduction in the flame temperature, CO mole fraction reduces drastically.

5. Flowing Phase: The flowing phase corresponds to flame extinction. Eventually, both bifurcated flames extinguish. The upstream bifurcated flame extinguishes due to heat losses to cold walls, and the downstream bifurcated flame extinguishes due to consumption of fuel in the hot part of the tube. Temperature and CO mole fraction profiles along the tube axis for the flowing phase are not shown since they are similar to profiles without any flame.

Figure 4.6 shows temporal histories of the maximum temperature and the maximum OH mole

fraction along the tube axis during multiple FREI cycles for the 1atm case. Maximas for all intermediate species and temperature occur at the mid-plane in the tube for a FREI cycle [85, 86]. As shown in Figure 4.6, after the ignition in a FREI cycle, the maximum temperature and the maximum OH mole fraction along the tube axis increase rapidly, and both change periodically in FREI with intermittent periods of relative inactivity. This relative inactivity is attributed to flow of fresh unburned mixture and build up of radical pools. After an inactive period, a sudden auto-ignition occurs and the FREI cycle repeats itself. The maximum temperature and the maximum OH mole fraction contours follow the similar pattern, hence the maximum OH mole fraction along the tube axis can be taken as a quantitative parameter for the flame location.

Figure 4.7 displays instantaneous FREI OH snapshots for the 1atm case for two FREI cycles. The position of the peak OH mole fraction is used to indicate the flame front location. An unburned premixed stoichiometric propane/air mixture enters from the left end of the tube and moves towards the right slowly gaining heat from the wall. Eventually, auto-ignition occurs far downstream

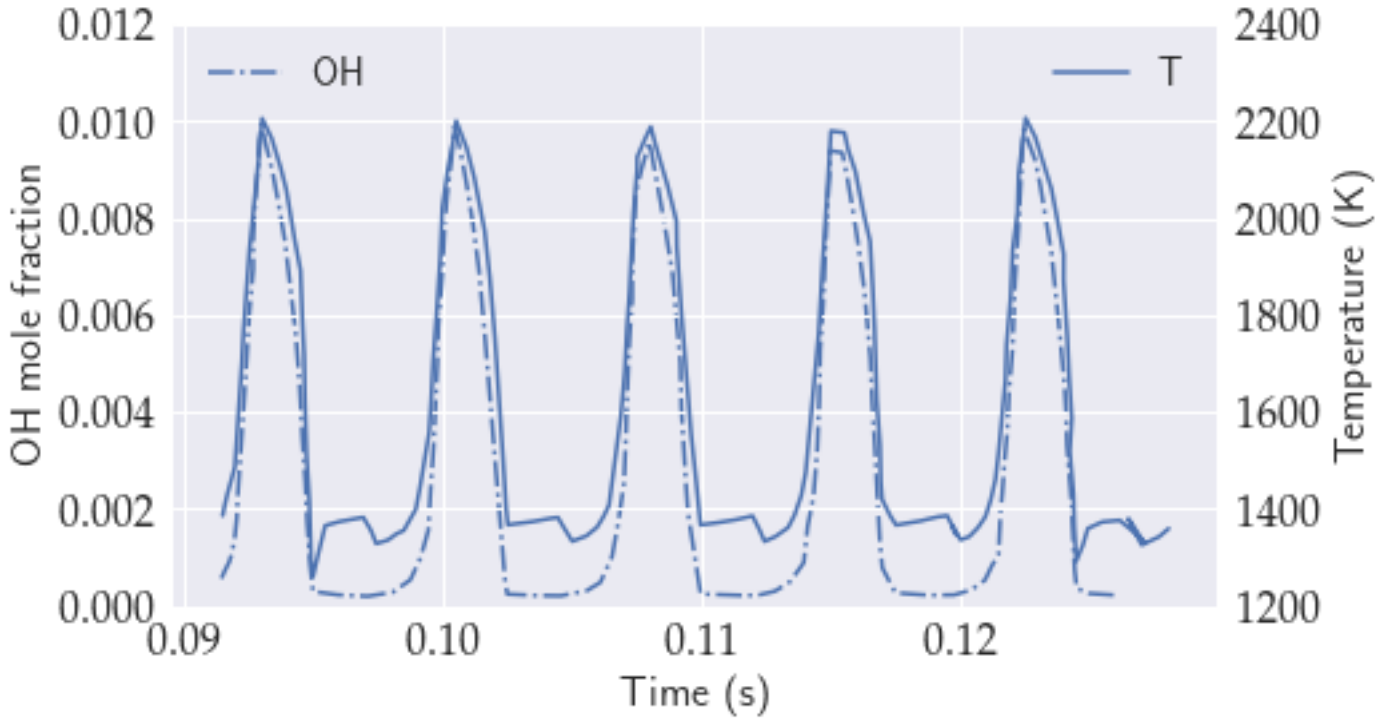

Figure 4.6: Temporal histories of maximum temperature and maximum OH mole fraction along the tube axis for multiple FREI cycles.

when a sufficiently high gas temperature is reached due to heat transfer from the hot tube walls. The flame front forms and propagates upstream after ignition, where it eventually extinguishes due to an excessive heat losses to relatively tube cold walls. After a significant delay, a new unburned premixed mixture fills up the hot section of the tube, and re-ignition occurs towards the downstream side. Soon after re-ignition a flame front forms, which quickly moves upstream, where it extinguishes again. The time difference between the extinction of FREI and re-ignition of the unburned mixture is known as recharge process, which is shown in Figure 4.7 [20]. Bifurcated flames can be not be seen in Figure 4.7 because of their low-luminosity.

Figure 4.8 shows instantaneous FREI snapshots for 1atm, 2atm, 5atm and 10atm pressure cases. One FREI cycle is shown for each pressure case. Figure 4.8 illustrates that increase in pressure affects the FREI behavior drastically, as both FREI ignition and extinction positions shift far up-

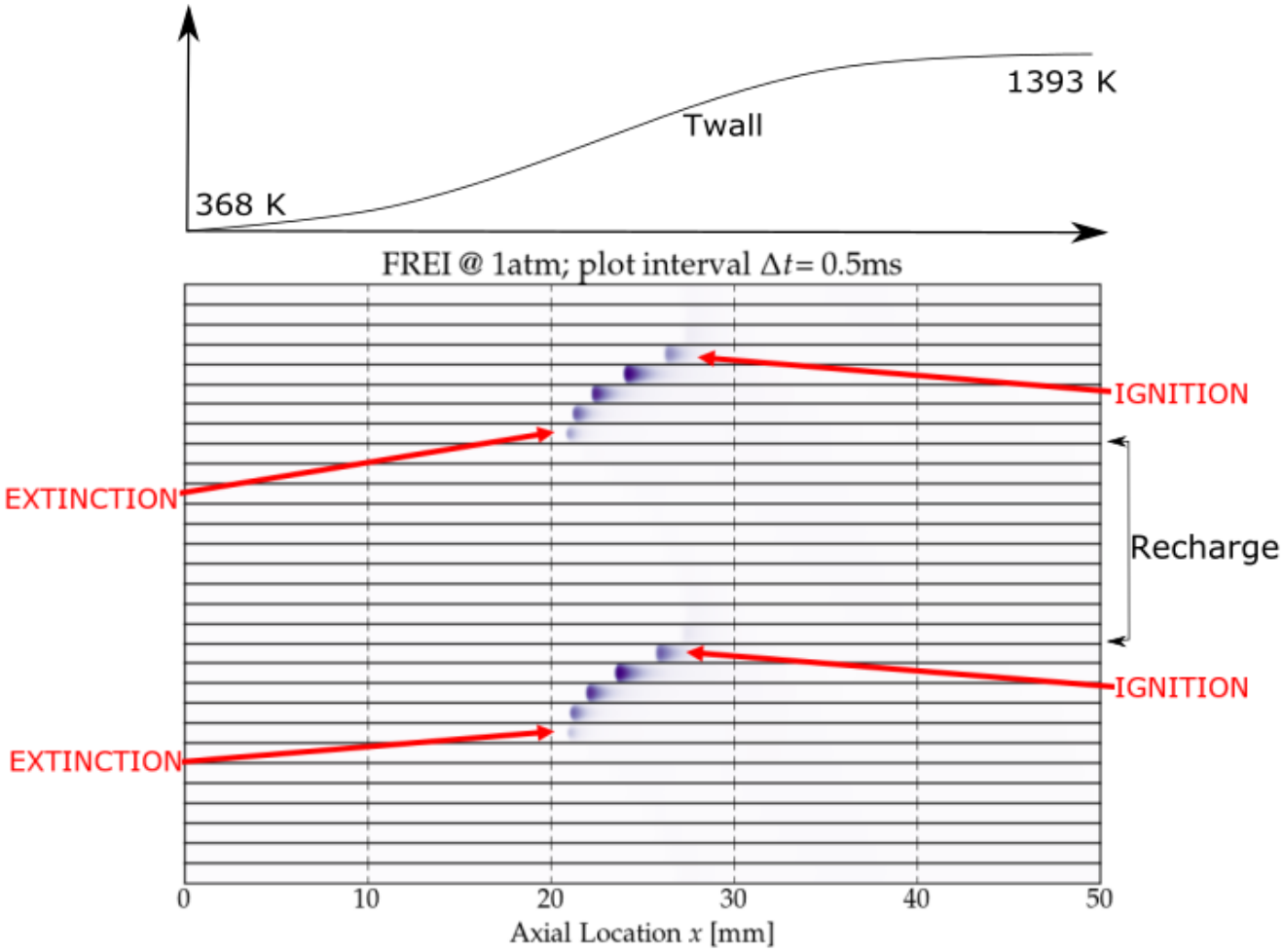

Figure 4.7: Instantaneous FREI OH snapshots for 1 atmospheric case.

stream, where wall temperatures are lower. For the 10atm case, the flame does not quench and moves to the tube inlet. Further it is observed that a shift in the extinction point is more pro-

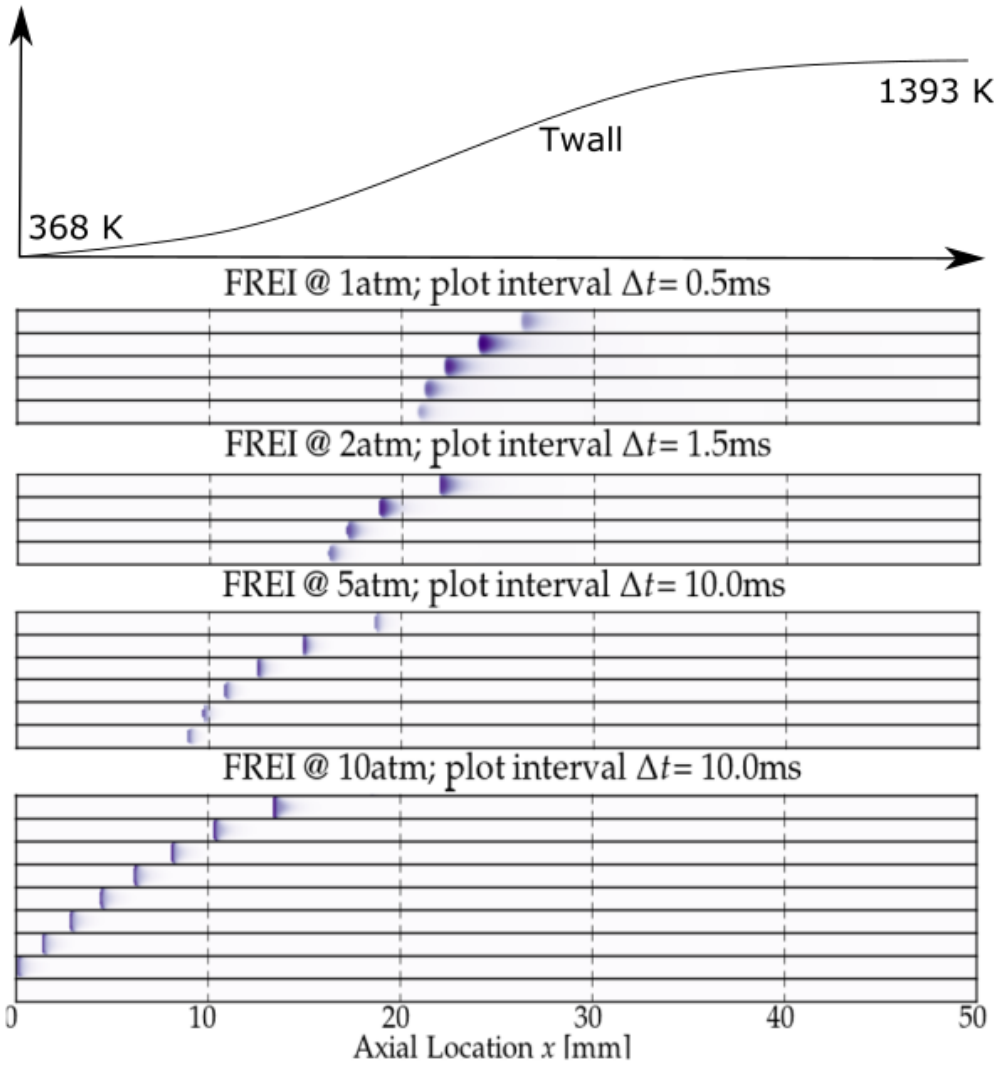

Figure 4.8: Instantaneous FREI OH snapshots for different pressures.

nounced in comparison of the ignition point for elevated pressures.

Table 4.3: Ignition temperature, Extinction temperature, FREI frequency, and FWHM reaction zone thickness for different pressures.

Pressure (atm)	Ignition Temperature (K)	Extinction Temperature (K)	Frequency (Hertz)	FWHM Reaction Zone Thickness (mm) (plot)
1	1333	1087	142	1.11
2	1309	744	41	0.63
5	1235	433	7	0.55
10	999	N/A	N/A	0.33

Figure 4.9 shows the temporal OH mole fraction as a function of the wall temperature for different pressures, where the periodic variation of the OH mole fraction is plotted with respect to the wall temperature during the FREI cycle. Figure 4.9 illustrates that during ignition, the OH mole fraction increases sharply, and remains at an elevated level while the flame propagates upstream. At the

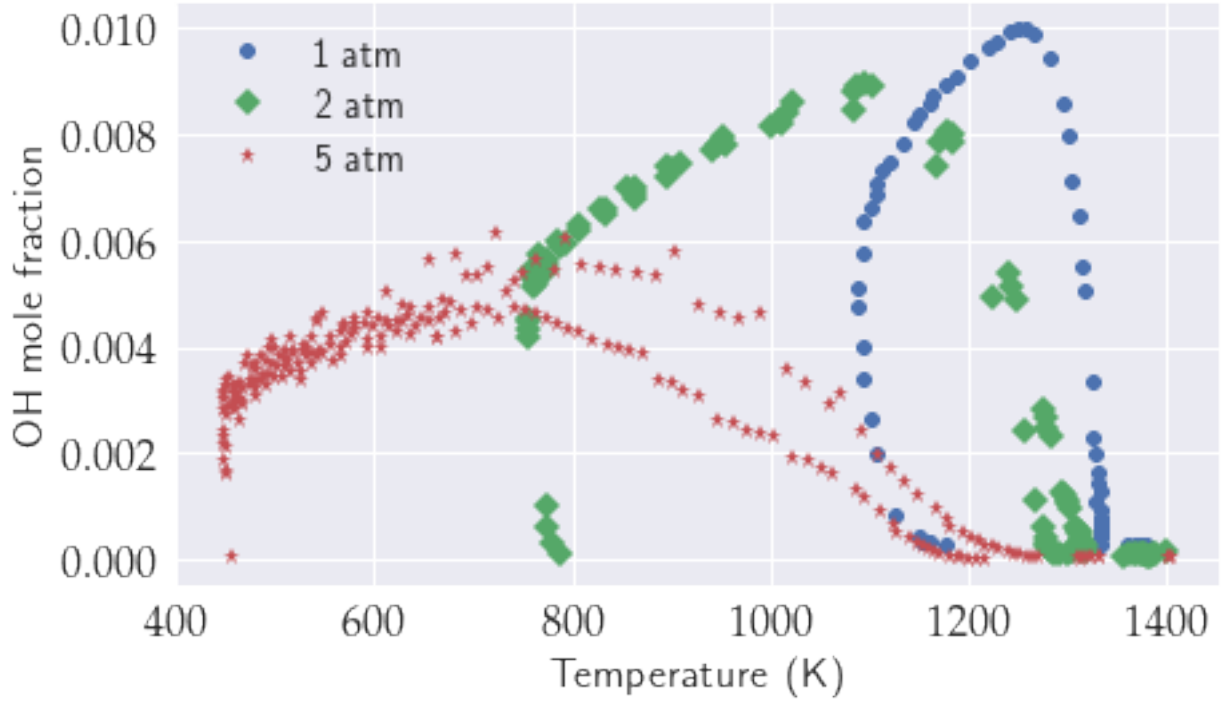

Figure 4.9: Temporal OH mole fraction as a function of the wall temperature for different pressures.

upstream extinction location, the OH mole fraction decreases and eventually extinguishes. Figure 4.9 can be used to obtain ignition and extinction temperatures by finding wall temperatures at which the OH mole fraction sharply increases and decreases, respectively. It is observed that the first and subsequent ignition-extinction cycles show slightly different temporal OH mole fraction contours. In the case of 5atm, data show some oscillations, which are attributed to imperfect grid spacing, which no longer sufficiently resolves the flame thickness at the given pressure. Table 4.3 demonstrates results for ignition and extinction temperatures of FREI for all four cases. Both ignition and extinction temperatures are calculated by finding x-intercept of OH mole fraction contours. Both ignition and extinction temperatures decrease with increasing pressure, although the decrease is more pronounced for the extinction temperature, which is consistent with a known reduction in the quenching diameter for increasing pressure ($d_T \propto \frac{1}{P}$) [28]. For 10 atm , the flame ignites and propagates to the inlet where it stabilizes, i.e., no extinction is observed. Overall, results clearly show that FREI relies on flame quenching, where a decrease in FREI extinction temperatures at high pressures will require microcombustors with reduce diameters.

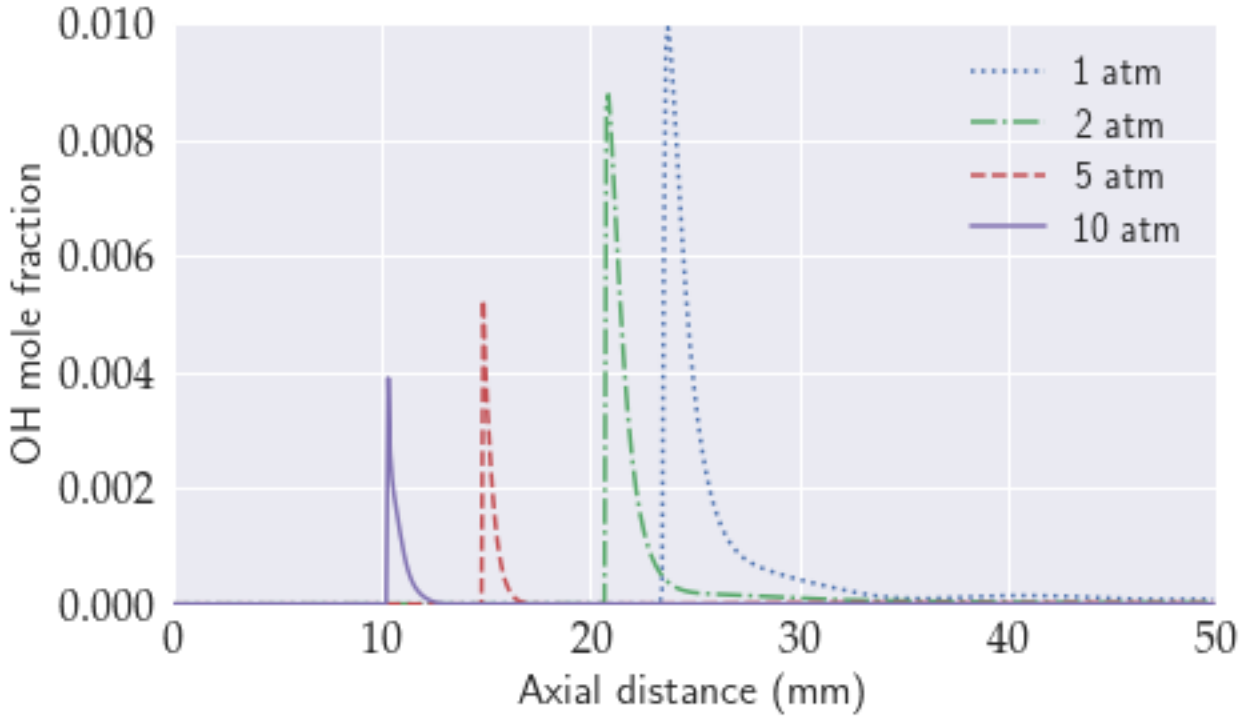

Figure 4.10: Impact of pressure on the peak OH mole fraction on the FREI cycle.

Figure 4.10 shows the impact of pressure on peak OH mole fraction during the FREI cycle. Figure 4.10 illustrates that with increasing pressure there is a significant upstream shift of the location for peak OH mole fraction. The decrease in the peak OH mole concentration with a decrease in pressure is attributed to a reduction in the OH creation rate due to lower temperatures. Table 4.3 further illustrates the Full-Width Half Maximum (FWHM) calculated for FREI reaction zone thickness at different pressures. Here, the reaction zone thickness is calculated by taking the difference between two axial positions at which the the OH mole fraction is equal to half of its maximum value. From Table 4.3 it is evident that the reaction zone thickness decreases with an increase in pressure, which is in direct correlation with the literature that laminar flame thickness (δ) decreases with increasing pressure ($d \propto \frac{1}{P}$) [28]. While results are consistent with observations from adiabatic flames, it is noted that FREI are strongly non-adiabatic due to flame-wall thermal interactions, where further details need to be investigated using analytical studies.

Table 4.3 illustrates the frequency of FREI for different pressures. The FREI frequencies are calculated by taking the inverse of the time difference in two ignition periods. Simulations of FREI result in frequencies of 142Hz for 1atm, 41Hz for 2atm, and 7Hz for 5atm. The decrease in FREI frequency as pressure increase is attributed to the larger drop of extinction temperatures in comparison to ignition temperatures as well as a reduction of flame propagation velocities, i.e., flames will travel a larger distance before quenching due to reduction in flame propagation velocities.

4.6 Summary

The numerical study in this section has investigated the impact of pressure on FREI behavior in a 1mm diameter tube at four pressures (1atm, 2atm, 5atm, and 10atm) while holding the mass flux and other external conditions constant. FREI phenomena are observed for 1atm, 2atm, and 5atm pressure cases, but flame do not quench for the 10atm case and sit at the inlet of the tube, which indicates that high pressure FREI will need reduced microcombustor (d<1mm). Flame bifurcations in FREI are observed. Temporal evaluations of OH mole fraction and temperature during FREI cycle are plotted to show the periodic nature of FREI behavior. It is found that both

ignition and extinction temperatures decrease with increasing pressure, and the pressure effect is more pronounced for the extinction temperature, which is consistent with a known reduction of quenching diameters at elevated pressures. The FREI reaction zone thickness is found to decrease with pressure, which corresponds to the behavior of laminar flames. Peak OH mole fractions decrease with increasing pressure due to reduction in OH production rates at lower temperatures. Further, frequencies of FREI decrease with increase of pressure due to an increase of the traveled distance as well as a reduction of flame speeds.

Overall, this study finds that trends for auto-ignition, extinction, and reaction zone thickness observed in FREI closely resemble known trends for corresponding adiabatic phenomena for engine relevant pressures, i.e., FREI constitute a promising approach to understand impact of new fuels on IC engine behavior.

Chapter 5
Conclusions and Recommendations

Fuel behavior impacts the IC engine significantly. The current thesis has used an externally heated microcombustor as an alternative testing device to study gaseous fuel behaviors at the atmospheric pressure. The purpose of this thesis is to develop a small sample fuel tester and investigate the applicability of FREI and strong flames behavior for fuel characterization. FREI and strong flame behavior are investigated in detail. Dynamic response of flames with repetitive extinction and ignition (FREI) is shown to depend on fuel properties, which shows FREI potential for fuel characterization. The relatively small test sample suggests the potential of the approach be used to accelerate traditional and bio-derived fuel research. As auto-ignition and extinction are directly quantified, there are indications that the measurements presented here could be extended to quantify the impact of fuel on engine performance. Results for different gaseous fuels reveal similar trends as those reported in earlier weak flame studies. The strong flame behavior has given an insight into laminar flame speeds of fuels. A significant contribution of this work is the introduction of pressure measurements for the quantification of dynamic FREI behavior, which together with low-speed imaging of CH^* emission, holds promise as a convenient approach for fuel testing and characterization.

2D axisymmetric numerical simulations are performed to investigate FREI behavior for engine relevant pressures. In numerical simulations, FREI ignition and extinction temperatures and reaction zone thickness are found similar to corresponding adiabatic phenomena at elevated pressure.

The author would like to suggest the following recommendations for future works:

1. In the present work, gaseous fuels are investigated inside the microcombustor. To understand the behavior of practical fuels inside the microcombustor, PRFs, TSFs (Toluene standard Fuel), and bio-fuels are to be tested inside the microcombustor.

2. A microcombustor experimental setup for high pressure experiments (up to 20 bar) is need to be developed to understand practical fuels behavior for engine relevant pressures..

3. Temperature measurements by translating a thermocouple within a microcombustor have a

good repeatability, but they are affected by transient, insertion, and radiative losses effects [89]. Moreover, the thermocouple measurement is an intrusive technique and not suitable for high pressure experiments. Hence a non-intrusive temperature measurements technique is required for future experimental work .

Experiments and numerical simulations have shown the potential of microcombustion to understand impact of fuel on IC engine behavior. Considering encouraging signs, microcombustor experiments should be continued for gasoline representative fuels.

Bibliography

[1] *ASTM International, Standard test method for motor octane number of sparkignition engine fuel, ASTM D2700-11*, 2011.

[2] *ASTM International, Standard test method for research octane number of sparkignition engine fuel, ASTM D2699-11*, 2011.

[3] 2017, Later Model Year Light-Duty Vehicle GHG Emission Standards, and CAFE Standards, 2012.

[4] International Energy Outlook 2017. Technical report, U.S. Energy Information Administration U.S. Energy Information Admin, 2017.

[5] Global Transport Scenarios 2050. Technical report, World Energy Council, 2011.

[6] Corporate Average Fuel Economy: National Highway Traffic Safety Administration, 2018.

[7] F. An, D. Gordon, H. He, D. Kodjak, and D. Rutherford. Passenger vehicle greenhouse gas and fuel economy standards: A global update, 2007.

[8] G. E. Andrews and D. Bradley. The burning velocity of methane-air mixtures. *Combust. Flame*, 19:275–288, 1972.

[9] G. E. Andrews and D. Bradley. Determination of burning velocities: A critical review. *Combust. Flame*, 18:133–153, 1972.

[10] F. Bianco, S. Chibbaro, and G. Legros. Low-dimensional modeling of flame dynamics in heated microchannels. *Chemical Engineering Science*, 2015.

[11] Hopf Bifurcations.

[12] C. Brock and D. Stanley. The cooperative fuels research engine: Applications for education and research. *Journal of Aviation Technology and Engineering*, 2012.

[13] Holthuis & Associates Flat Flame Burners. http://www.flatflame.com/.

[14] J. Caton. A comparison of lean operation and exhaust gas recirculation: Thermodynamic reasons for the increases of efficiency. *SAE Technical Paper 2013-01-0266*, 2013.

[15] Chemical-Kinetic Mechanisms for Combustion Applications. Mechanical and Aerospace Engineering (Combustion Research), University of California at San Diego, 2009.

[16] A. Cuoci, A. Frassoldati, T. Faravelli, and E. Ranzi. A computational tool for the detailed kinetic modeling of laminar flames: application to C_2H_4/CH_4 coflow flames. *Combust. Flame*, 160:870–886, 2013.

[17] A. Cuoci, A. Frassoldati, T. Faravelli, and E. Ranzi. Numerical modeling of laminar flames with detailed kinetics based on the operator-splitting method. *Energy & Fuels*, 27(12):7730–7753, 2013.

[18] J. Ewald and N. Peters. On unsteady premixed turbulent burning velocity prediction in internal combustion engines. *Proceedings of the Combustion Institute*, 2007.

[19] A. Fan, S. S. Minaev, E. V. Sereshchenko, Y. Tsuboi, H. Oshibe, H. Nakamura, and K. Maruta. Dynamic behavior of splitting flames in a heated channel. *Combust. Explos. Shock Waves*, 45:245–250, 2009.

[20] Y. Fan, Y. Suzuki, and N. Kasagi. Experimental study of micro-scale premixed flame in quartz channels. *Proc. Combust. Inst.*, 32:3083–3090, 2009.

[21] J. Farrell. Co-optimization of fuels and engines. Technical report, SAE High Efficiency Internal Combustion Engine Symposium, 2016.

[22] J. Farrell and J. Holladay. Co-optimization of fuels & engines-2017 beto peer review. Technical report, U.S. Department of Energy, 2017.

[23] J. Farrell, W. Weissman, R. Johnston, and J Nishimura. Fuel effects on sidi efficiency and emissions. *SAE Technical Paper 2003-01-3186*, 2003.

[24] A. C. Fernandez-Pello. Micro-power generation using combustion: Issues and approaches. *Proc. Combust. Inst.*, 29:883–899, 2002.

[25] Climate Change 2014 Synthesis Report Summary for Policymakers, 2014.

[26] D. Gaspar. Co-optimization of fuels & engines-2017 beto peer review. Technical report, U.S. Department of Energy, 2017.

[27] G. P. Gauthier, G. M. G. Watson, and J. M. Bergthorson. Burning rates and temperatures of flames in excess-enthalpy burners: A numerical study of flame propagation in small heat-recirculating tubes. *Combustion and Flame*, 161(9):2348 – 2360, 2014.

[28] I. Glassman. *Combustion*. Academic Press, San Diego, 1996.

[29] IDS Imaging Development Systems GmbH. https://en.ids-imaging.com/home.html.

[30] P. Grajetzki, H. Nakamura, T. Tezuka, S. Hasegawa, and K. Maruta. Evaluation of the reactivity of ultra-lean prf/air mixtures by weak flames in a micro flow reactor with a controlled temperature profile. *Combustion Science and Technology*, page pages 1â21, 2018.

[31] K.P. Grogan, S.S. Goldsborough, and M. Ihme. Ignition regimes in rapid compression machines. *Combustion and Flame*.

[32] K.P. Grogan, S.S. Goldsborough, and M. Ihme. Mild ignition phenomena in rapid compression machines. 25th International Colloquium on the Dynamics of Explosions and Reactive Systems (ICDERS), 2015.

[33] R. J. Hall. The radiative source term for plane-parallel layers of reacting combustion gases. *Journal of Quantitative Spectroscopy and Radiative Transfer*, 1993.

[34] R.K. Hanson and D.F. Davidson. Recent advances in laser absorption and shock tube methods for studies of combustion chemistry. *Progress in Energy and Combustion Science*.

[35] J. B. Heywood. *Internal Combustion Engine Fundamentals*. McGraw Hill, 1988.

[36] M. Hori, H. Nakamura, T. Tezuka, S. Hasegawa, and K. Maruta. Characteristics of *n*-heptane and toluene weak flames in a micro flow reactor with a controlled temperature profile. *Proc. Combust. Inst.*, 34:3419–3426, 2013.

[37] M. Hori, A. Yamamoto, H. Nakamura, T. Tezuka, S. Hasegawa, and K. Maruta. Study on octane number dependence of PRF/air weak flames at 1–5 atm in a micro flow reactor with a controlled temperature profile. *Combust. Flame*, 159:959–967, 2012.

[38] W. Hsieh, R. Chen, T. Wu, and T. Lin. Engine performance and pollutant emission of an si engine using ethanolâgasoline blended fuels. 2002.

[39] Y. Huang, C. J. Sung, and J. A. Eng. Laminar flame speeds of primary reference fuels and reformer gas mixtures. *Combust. Flame*, 139:239–251, 2004.

[40] Trends in Global CO2 and Total Greenhouse Gas Emissions, 2017.

[41] Waukesha Engine. An international historic mechanical engineering landmark the Waukesha CFR fuel research engine. 1980.

[42] InvenSense. *InvenSense ICS-40300 : High SPL Analog Microphone with Extended Low Frequency Response*.

[43] How is Today Warming Different from the Past?, 2018.

[44] S. Jerzembeck, N. Peters, P. Pepiot-Desjardins, and H. Pitsch. Laminar burning velocities at high pressure for primary reference fuels and gasoline: Experimental and numerical investigation. *Combustion and Flame*, 2009.

[45] Y. Ju and K. Maruta. Microscale combustion: Technology development and fundamental research. *Progress in Energy and Combustion Science*, 37:669–715, 2011.

[46] G. Kalghatgi. Auto-ignition quality of practical fuels and implications for fuel requirements of future si and hcci engines. *SAE Technical Paper 2005-01-0239*, 2005.

[47] G. Kalghatgi. *Fuel/Engine Interactions*. SAE International, 2013.

[48] G.T. Kalghatgi. Developments in internal combustion engines and implications for combustion science and future transport fuels. *Proceedings of the Combustion Institute*, 2015.

[49] T. Kamada, H. Nakamura, T. Tezuka, S. Hasegawa, and K. Maruta. Study on combustion and ignition characteristics of natural gas components in a micro flow reactor with a controlled temperature profile. *Combust. Flame*, 161:37–48, 2015.

[50] S. Kikui, H. Nakamura, T. Tezuka, S. Hasegawa, and K. Maruta. Study on combustion and ignition characteristics of ethylene, propylene, 1-butene and 1-pentene in a micro flow reactor with a controlled temperature profile. *Combustion and Flame*, 2016.

[51] N. I. Kim, S. Kato, T. Kataoka, T. Yokomori, S. Maruyama, T. Fujimori, and K. Maruta. Flame stabilization and emission of small swiss-roll combustors as heaters. *Combust. Flame*, 141:229–240, 2005.

[52] V. R. Kishore, S. Minaev, M. Akram, and S. Kumar. Dynamics of premixed methane/air mixtures in a heated microchannel with different wall temperature gradients. *The Royal Society of Chemistry*, 2017.

[53] C. Kolodziej, M. Pamminger, J. Sevik, and T. Wallner. Effects of fuel laminar flame speed compared to engine tumble ratio, ignition energy, and injection strategy on lean and egr dilute spark ignition combustion. *SAE Int. J. Fuels Lubr. 10(1):2017*, 2017.

[54] S. Kumar, K. Maruta, and S. Minaev. Experimental investigations on the combustion behavior of methaneâair mixtures in a micro-scale radial combustor configuration. *Journal of Micromechanics and Microengineering*, 2007.

[55] K. K. Kuo. *Principles of Combustion*. Wiley, 2nd edition, 2005.

[56] V. N. Kurdyumov, G. Pizza, C. E. Frouzakis, and J. Mantzaras. Dynamics of premixed flames in a narrow channel with a step-wise wall temperature. *Combust. Flame*, 156(11):2190–2200, 2009.

[57] T. G. Leone, J. E. Anderson, R. S. Davis, A. Iqbal, R. A. Reese, M. H. Shelby, and V. M. Studzinsk. The effect of compression ratio, fuel octane rating, and ethanol content on spark-ignition engine efficiency. 2015.

[58] B. Lewis and G. von Elbe. On the theory of flame propagation. *Journal of chemical physics*, 2:537–546, 1934.

[59] J.C. Livengood and P.C. Wu. Correlation of autoignition phenomena in internal combustion engines and rapid compression machines. In *5th Symp. (Int.) on Combustion*, 1955.

[60] E. Mallard and H. L. le Chatelier. Recherches experimentales et theoriques sur la combustion des melanges gaseux explosifs. *Annales des Mines*, 4:274–618, 1883.

[61] K. Maruta. Micro and mesoscale combustion. *Proc. Combust. Inst.*, 33:125–150, 2011.

[62] K. Maruta, T. Kataoka, N. I. Kim, S. Minaev, and R. Fursenko. Characteristics of combustion in a narrow channel with a temperature gradient. *Proc. Combust. Inst.*, 30:2429–2436, 2005.

[63] K. Maruta, J. K. Parc, K. C. Oh, T. Fujimori, S. S. Minaev, and R. V. Fursenko. Characteristics of microscale combustion in a narrow heated channel. *Combust. Explos. Shock Waves*, 40(5):516–523, 2004.

[64] R. McCormick. Fuel property characterization and prediction. fy17 vehicle technologies office annual merit review. Technical report, U.S. Department of Energy, 2017.

[65] S. Minaev, K. Maruta, and R. Fursenko. Nonlinear dynamics of flame in a narrow channel with a temperature gradient. *Combust. Theory Model.*, 11:187–203, 2007.

[66] H. Mirels. Shock tube test time limitation due to turbulent wall boundary layer, 1963.

[67] E. Miyata, N. Fukushima, Y. Naka, M. Shimura, M. Tanahashi, and T. Miyauchi. Direct numerical simulation of micro combustion in a narrow circular channel with a detailed kinetic mechanism. *Proc. Combust. Inst.*, 35:3421–3427, 2015.

[68] H. Nakamura, A. Fan, S. Minaev, E. Sereshchenko, R. Fursenko, Y. Tsuboi, and K. Maruta. Bifurcations and negative propagation speeds of methane/air premixed flames with repetitive extinction and ignition in a heated microchannel. *Combust. Flame*, 159:1631–1643, 2012.

[69] H. Nakamura, A. Yamamoto, M. Hori, T. Tezuka, S. Hasegawa, and K. Maruta. Study on pressure dependences of ethanol oxidation by separated weak flames in a micro flow reactor with a controlled temperature profile. *Proc. Combust. Inst.*, 34:3435–3443, 2013.

[70] V. Naralasetti. Micro combustion of primary reference fuels in narrow heated channels. Master's thesis, LSU Master's Theses, 2018.

[71] D. G. Norton and D. G. Vlachos. Combustion characteristics and flame stability at the microscale: a CFD study of premixed methane/air mixtures. *Chem. Eng. Science*, 58:4871–4882, 2003.

[72] Co-Optimization of Fuels & Engines-2016 Year in Review. Technical report, U.S. Department of Energy, 2017.

[73] Co-Optimization of Fuels & Engines: Efficiency Merit Function for Spark-Ignition Engines, 2018.

[74] U. S. House of Representatives (2007) Resolution 6-310, 2007.

[75] GLOBAL CLIMATE CHANGE: Vital Signs of the Planet, 2018.

[76] US Department of Transportation. U.s. dot and epa propose fuel economy standards for my 2021-2026 vehicles, August 2 2018.

[77] Inventory of U.S. Greenhouse Gas and Emission Sinks (1990-2016), 2018.

[78] Inventory of U.S. Greenhouse Gas Emissions and Sinks. Technical report, United States Environmental Protection Agency, 2017.

[79] OpenFoam. OpenFoam - The Open CFD Toolbox. http://www.openfoam.com/, 2004-2016.

[80] H. Oshibe, H. Nakamura, T. Tezuka, S. Hasegawa, and K. Maruta. Stabilized three-stage oxidation of DME/air mixture in a micro flow reactor with a controlled temperature profile. *Combust. Flame*, 157:1572–1580, 2010.

[81] Fuels Performance. Technical report, National Renewable Energy Laboratory, 2014.

[82] U.S. DEPARTMENT OF TRANSPORTATION: SUMMARY OF FUEL ECONOMY PERFORMANCE, 2011.

[83] N. Peters. Fifteen lectures on laminar and turbulent combustion. Technical report, Ercoftac Summer School, RWTH Aachen.

[84] H. Pitsch. Laminar premixed flames: Kinematics and burning velocity, 2014.

[85] G. Pizza, C. E. Frouzakis, J. Mantzaras, A. G. Tomboulides, and K. Boulouchos. Dynamics of premixed hydrogen/air flames in microchannels. *Combust. Flame*, 152:433–450, 2008.

[86] G. Pizza, C. E. Frouzakis, J. Mantzaras, A. G. Tomboulides, and K. Boulouchos. Three-dimensional simulations of premixed hydrogen/air flames in microtubes. *J. Fluid Mech*, 658:463–491, 2010.

[87] H.R. Ricardo and J.G.G. Hempson. The high-speed internal combustion engine. *Blackie and Son*, 1953.

[88] I. Schoegl. *Superadiabatic Combustion in Counter-Flow Heat Exchangers*. PhD thesis, The University of Texas at Austin, 2009.

[89] I. Schoegl, P. Sharma, and M. J. McNenly. Ignition and extinction of gaseous fuels in the FREI regime. in revision, 2016.

[90] N.N. Semenov. Naca tech. memo. (1282), 1951.

[91] Z. Shao, S. M. Haile, J. Ahn, P. D. Ronney, Z. Zhan, and S. A. Barnett. A thermally self-sustained micro solid-oxide fuel-cell stack with high power density. *Nature*, 435:795–798, 2005.

[92] L. Sitzki, K. Borer, E. Schuster, P. D. Ronney, and S. Wussow. Combustion in microscale heat-recirculating burners. In *Third Asia-Pacific Conference on Combustion*, 2001.

[93] Light-Duty Vehicle GHG Emission Standards and 75:88. CAFE Standards; Final Rule. Federal Register, 2010.

[94] A.D. Stazio, C. Chauveau, G. Dayma, and P. Dagaut. Combustion in micro-channels with a controlled temperature gradient. *Experimental Thermal and Fluid Science*, 2016.

[95] A.D. Stazio, C. Chauveau, G. Dayma, and P. Dagaut. Oscillating flames in micro-combustion. *Combustion and Flame*, 2016.

[96] G. Strang. On the construction and comparison of difference schemes. *SIAM Journal on Numerical Analysis*, 1968.

[97] R.A. Strehlow and A. Cohen. Limitations of the reflected shock technique for studying fast chemical reactions and its application to the observation of relaxation in nitrogen and oxygen. *THE JOURNAL OF CHEMICAL PHYSICS*, 1959.

[98] C. Sung and H. Curran. Using rapid compression machines for chemical kinetics studies. *Progress in Energy and Combustion Science*, 2014.

[99] S. Suzuki, M. Hori, H. Nakamura, T. Tezuka, S. Hasegawa, and K. Maruta. Study on cetane number dependence of diesel surrogates/air weak flames in a micro flow reactor with a controlled temperature profile. *Proc. Combust. Inst.*, 34:3411–3417, 2013.

[100] J. Szybist and D. Splitter. Effects of fuel composition on egr dilution tolerance in spark ignited engines. *SAE Int. J. Engines 9(2):819-831*, 2016.

[101] Y. Tsuboi, T. Yokomori, and K. Maruta. Lower limit of weak flame in a heated channel. *Proc. Combust. Inst.*, 32:3075–3081, 2009.

[102] S. R. Turns. *An Introduction to Combustion: Concepts and Applications*. McGraw Hill, 2nd edition, 2000.

[103] Tamron USA. http://www.tamron-usa.com/.

[104] J. Vican, B. F. Gajdeczko, F. L. Dryer, D. L. Milius, I. A. Aksay, and R. A. Yetter. Development of a microreactor as a thermal source for MEMS power generation. *Proc. Combust. Inst.*, 29:909–916, 2002.

[105] C. Wang, J.M. Herreros, C. Jiang, A. Sahu, and H. Xu. Engine thermal efficiency gain and well-to-wheel greenhouse gas savings when using bioethanol as a gasoline-blending component in future spark-ignition engines: A china case study. 2018.

[106] C. Wang, S. Zeraati-Rezaei, L. Xiang, and H. Xu. Ethanol blends in spark ignition engines: Ron, octane-added value, cooling effect, compression ratio, and potential engine efficiency gain. 2017.

[107] GE Power & Water. Waukesha* cfr* combination research & motor method octane rating unit, 2013.

[108] A. Yamamoto, H. Oshibe, H. Nakamura, T. Tezuka, S. Hasegawa, and K. Maruta. Stabilized three-stage oxidation of gaseous *n*-heptane/air mixture in a micro flow reactor with a controlled temperature profile. *Proc. Combust. Inst.*, 33:3259–3266, 2011.

[109] Z. Yang and A. Bandivadekar. Global update: Light-duty vehicle greenhouse gas and fuel economy standards, 2017.

[110] F. Yuksel and B. Yuksel. The use of ethanol gasoline blend as a fuel in an si engine. 2004.

Appendix A
OpenFOAM Software Description

A.1 OpenFOAM Software Description

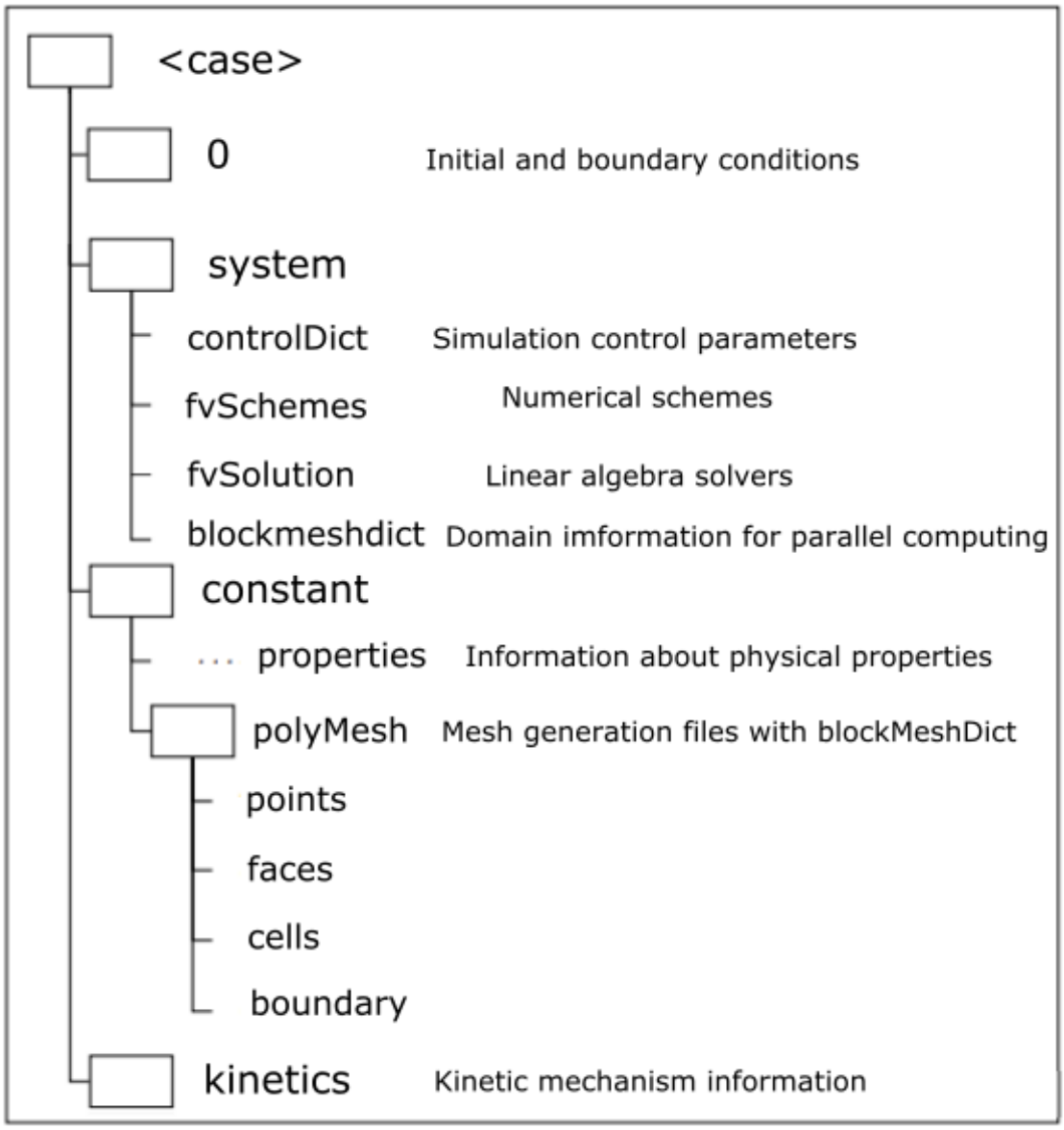

Figure A.1: OpenFOAM file structure

OpenFOAM is a free and open-source software, which is widely used for continuum mechanics problems analysis in both commercial and academic organizations. OpenFOAM uses finite volume method (FVM) for discretization and numerical calculations. OpenFOAM contains several physical models including turbulence models, chemical reactions, kinetics models, thermodynamic models, and radiative heat transfer models. OpenFOAM has several libraries written in C++ pro-

gramming languages, which are used to develop applications. OpenFOAM applications can be divided into two categories: utilities and solvers. While utilities are used to set up the simulations/mesh and operate on simulation results, solvers are used to perform numerical calculations. OpenFOAM also provides an ability to change existing solvers and utilities according to a specific problem.

OpenFOAM has an organized file structure, which is used to set up the simulation and mesh. Figure A.1 presents a hierarchical diagram of the file structure in OpenFOAM. The case is the main folder. 0, system, constant, and kinetics are subfolders. The 0 folder includes initial and boundary information. For this study, the 0 folder contains the the initial concentration of reactants, the velocity field, and the temperature field. The system folder has controldict, fvSchemes, fvSolution, and blockMeshDict files. The Controldict file includes information about mesh size, time step, and Courant number. The fvSchemes file includes information about numerical discretization schemes with interpolation schemes. The fvSolution file contains information about solvers to solve systems of the discretized linear system of equations. The BlockMeshDict file is used to divide the computational domain into small pieces for parallel computing. The constant folder includes a properties file, which has information about various physical constants and properties. The constant folder also contains a polyMesh folder, which has information about the case mesh.

A.1.1 Boundary Conditions In OpenFOAM

In OpenFOAM, a geometry boundary is broken into patches for applying boundary conditions properly. A keyword is assigned to each patch. A patch can contain two or more boundary. Keywords assigned to patches are used to setup initial and boundary conditions in the 0 folder. Boundary conditions used in this study are explained below.

* FixedValue: This boundary condition is used to provide a fixed value at a boundary for the whole simulation time. Both uniform and nonuniform boundary conditions can be provided through FixedValue. The no slip boundary condition at walls can also be imposed by specifying variable values zero. This boundary condition works as the Dirichlet boundary condition.

* ZeroGradient: This boundary condition sets the values of the variable gradient from the internal field to the patch as zero.

* Wedge: Wedge boundary condition has been used in our study for the 2D axisymmetric case. This has provided a cyclic boundary condition on the wedge patches.

Appendix B
Operator-splitting Method

B.1 Operator-splitting Method

CRECK group in Milan has developed the laminarSMOKE solver. The laminarSMOKE solver is built on the top of open-source CFD package OpenFOAM. The laminarSMOKE provides a capability to solve 2D and 3D problems. Both structured and unstructured meshes can be used with the laminarSMOKE solver. The laminarSMOKE solver utilizes operator-splitting algorithm to solve compressible, unsteady, and non-reacting flows. The operator-splitting method works by segregating transport and reaction terms. The one significant advantage of using the laminarSMOKE solver with OpenFOAM instead of ANSYS Fluent is that laminarSMOKE solver is capable of managing very large kinetic mechanisms consisting thousands of reactions and hundreds of species. The laminarSMOKE solver also provides an ability to run code in parallel mode with Message Passing Interface (MPI) library.The laminarSMOKE solver uses the operator-splitting approach for transport and energy equations and solves continuity and momentum equations using PISO algorithm of piso-FOAM solver in OpenFOAM.

The operator-splitting method is briefly summarized here. Transport equations of energy and species can be written as B.1 after the spatial discretization. To reduce stiffness in numerical schemes because of complex kinetic mechanisms, the stiff chemical term is separated from the transport terms (convection and diffusion). Where ψ is the vector of temperature in the energy equation or species mass fraction in the transport equation (dependent variables). $\mathrm{R}(\psi)$ vector stands for the rate of change in ψ due to chemical reactions, $\mathrm{C}(\psi_\mathrm{t})$vector represents the change in ψ due to convection, and $\mathrm{D}(\psi_\mathrm{t})$ vector represents the change in ψ due to diffusion.

$$\frac{\partial \psi}{\partial t} = C(\psi) + D(\psi, t) + R(\psi) \tag{B.1}$$

Equation is B.1 numerically solved by advancing the solution in the discretized time step Δt. The solution is found by adding contributions from convection, diffusion, and reaction term mentioned above. To ensure a good stability and accuracy for complex kinetic mechanisms, convection and

diffusion terms are clubbed together, and the stiff chemistry operator is kept in the last. In the laminarSMOKE solver, the strange splitting scheme is used to group convection and diffusion terms, and keep them separate from the stiff reaction term [96]. Then numerical integration is performed in three steps. The algorithm for numerical integration is explained in detail [16, 17] and briefly summarized here.

Substep 1: Firstly reaction terms are integrated over the time step $\frac{\Delta t}{2}$ by solving system of stiff ordinary differential equations (ODE). The initial condition for substep 1 $\psi^{a}(0)$ is taken as the previous time step final solution. $\psi^{a}(\frac{\Delta t}{2})$ is denoted as solution of equation.

Substep 2: Then Equation B.3 is solved to integrate transport terms (convection and diffusion) along the full time step Δt. Substep 1 final state is treated as the initial condition $\psi^{b}(0)$ for the substep 2. Solution of the substep 2 is designated as $\psi^{b}(\Delta t)$.

Substep 3: This step is same as the substep 1 with the initial condition $\psi^{b}(\Delta t)$ comes from the substep 2. The substep 3 solution is used as an initial condition for the next time step.

$$\frac{\partial \psi^{a}}{\partial t} = R(\psi^{a}) \tag{B.2}$$

$$\frac{\partial \psi^{b}}{\partial t} = C(\psi^{b},t) + D(\psi^{b},t) \tag{B.3}$$

Substeps 1 and 3 do not require boundary conditions since they have no spatial dependence, but $C(\psi_{t})$ and $D(\psi_{t})$ have spatial dependence and require appropriate boundary conditions. For the spatial discretization of convection and diffusion terms, OpenFOAM utilities are used. The backward implicit Euler method is used to solve non-stiff ODE systems of equations. The linear system of the ODE is solved by using the iterative technique. The pressure implicit with splitting of operators (PISO) algorithm is used to make sure that mass is conserved at each time step during the solution of continuity and momentum equations. The preconditioned conjugate gradient (PCG) is used to solve pressure and density, whereas the preconditioned biconjugate gradient (PBiCG) is used to solve velocity, species, and temperature. Cholesky (DIC) and diagonal incomplete lower-

upper (DILU) techniques are used to preconditioned PCG and PBiCG, respectively.

VITA

Pawan Sharma was born and raised in Bharatpur, Rajasthan, India. He started his bachelor degree in the mechanical engineering department at Indian Institute of Technology-Banaras Hindu University, Varanasi, India in Fall 2008. He graduated in Spring 2013 with Bachelors and Masters in mechanical engineering. He worked for one year in TATA Consulting Engineers Limited, Noida, India from August 2013 to July 2014. In Fall 2014, he started his PhD study in the mechanical engineering department at Louisiana State University. After four years, he defended his PhD dissertation in Fall 2018.